PERMEABILITY EVOLUTION IN SANDSTONE: DIGITAL ROCK APPROACH

A DISSERTATION

SUBMITTED TO THE DEPARTMENT OF GEOPHYSICS

AND THE COMMITTEE ON GRADUATE STUDIES

OF STANFORD UNIVERSITY

IN PARTIAL FULFILLMENT OF THE REQUIREMENTS

FOR THE DEGREE OF

DOCTOR OF PHILOSOPHY

Ayako Kameda

October 2004

I certify that I have read this dissertation and that, in my opinion, it is fully adequate in scope and quality as a dissertation for the degree of Doctor of Philosophy.

_____
Amos Nur (Principal Adviser)

I certify that I have read this dissertation and that, in my opinion, it is fully adequate in scope and quality as a dissertation for the degree of Doctor of Philosophy.

_____
Gary Mavko

I certify that I have read this dissertation and that, in my opinion, it is fully adequate in scope and quality as a dissertation for the degree of Doctor of Philosophy.

_____
J.G. Liou

I certify that I have read this dissertation and that, in my opinion, it is fully adequate in scope and quality as a dissertation for the degree of Doctor of Philosophy.

_____
Jack Dvorkin

Approved for the University Committee on Graduate Studies.

_____

Abstract

Permeability is perhaps one of the most important yet elusive reservoir properties, since it poorly correlates with elastic properties, and as a result, cannot be mapped remotely. Physical permeability measurements may be augmented or even partially replaced by numerical experiments, provided that a numerical simulation accurately mimics the physical process. Numerical simulation of laboratory experiments on rocks, or digital rock physics, is an emerging field that may benefit the petroleum industry. For numerical experimentation to find its way into the mainstream, it has to be practical and easily repeatable, i.e., implemented on standard hardware and in real time. This condition reduces the feasible size of a digital sample to just a few grains across. Will the results be meaningful for a larger rock volume?

The answer is that small fragments of medium- to high-porosity sandstone, such as cuttings, which are not statistically representative of a larger sample, cannot be used to numerically calculate the exact porosity and permeability of the sample. However, by using a significant number of such small fragments, it may be possible to establish a site-specific permeability-porosity trend, which can be used to estimate the absolute permeability from independent porosity data, obtained in the well or inferred from seismic measurements.

This dissertation is based on a very simple philosophy: small is beautiful. Rather than finding a scientific solution to a problem by using bigger and more complicated technology, I focus on methods that employ smaller, faster, cheaper technologies, using digital rock physics.

Three fundamental results and techniques have emerged from this approach:

(1) Small and statistically sub-representative fragments of rock are still suitable to serve as input to digital permeability calculations. A large enough suite of such fragments can be used to obtain a meaningful permeability-porosity trend instead of the intuitively anticipated statistical noise. This trend is very close to a trend where porosity and permeability vary due to diagenetic changes in rock. This result implies that a spatial ensemble within a relatively small sample can represent a geologic-time ensemble.

(2) Rock can be digitally moved through geologic time and space by applying geometric alterations to a prototypical digital representation of a natural sample. This is one way to simulate the effect of burial on rocks, where rocks are transformed in time and in space. Such alteration can be conducted on a 2D digital prototype and then the corresponding 3D digital rock can be statistically reconstructed from the 2D prototype. The resulting permeability will be essentially the same as if the alterations were applied directly to the 3D prototype. This result means that the geologist can essentially draw diagenesis-related alterations on a thin section image and then realistically assess how these changes affect porosity and permeability. This makes geologic time and space travel a reality, which can be implemented in real time, using standard computational means.

(3) Finally, I show how to create a prototypical digital image to serve as a starting point for geologic time and space travel. Instead of mathematically packing idealized geometrical approximations of grains into a 3D volume (which is often mathematically intractable), I introduce the concept of the physical prototype, which is simply a collection of sand grains manually packed as desired or in accordance with specific depositional rules (as in eolian environment), epoxy-stabilized, and CT-scanned. A library of such prototypes can serve as a digital playground for practical permeability predictions.

Acknowledgements

I would like to express my special appreciation to Dr. Amos Nur and Dr. Jack Dvorkin for their guidance, encouragement, and their support. They made me want to work harder and become a better researcher. I would also like to thank Drs. Gary Mavko, Steve Graham, J.G. Liou, and Roland Horne for their valuable input and guidance.

Thanks are also due to Dr. Don Lowe and Dr. Peter Eichbul for their help in the interpretation of the Minnelusa thin-section. Thank you Dr. Richard Ketcham, for your great CT-scanning work.

My life at Stanford could not have been complete without great friends, too many to list here, but Margaret Muir deserves special mention for being a great friend through the darkest times. Thank you, Margaret.

Yuichi, thank you always for your support and your objective advise in both academics and in rock-climbing! You are truly a strong, hard-working person and a great role model. I wish I had your wisdom, stamina, and perseverance.

I want to thank my family-- my younger brother, for being himself and making me a proud big sister; my 80-year old grandmother, who came all the way to the U.S. to watch me graduate; and my mother, who is my best friend. Last but not least, I want to thank my father for providing me with great education all over the world, which prepared me for my studies here at Stanford. I dedicate this thesis to my father, because he never thanks *me* for anything, and I figured he might actually thank me for dedicating a thesis that took me years to complete!

The department of Geophysics, the Department of Energy, and the Stanford Rock Physics Project financially supported this work.

Table of Contents

List of Tables

List of Figures

Chapter 1
Introduction

Standing on our microscopic fragment of a grain of sand, we attempt to discover the nature and purpose of the universe which surrounds our home in space and time. -Sir James Jeans

1.1 General

Permeability is one of the most important petroleum reservoir properties, in addition to being an important parameter in many other applications, such as pollutant migration, hydrothermal systems, ground water storage, CO_2 storage, and nuclear repositories. Numerical simulations of fluid flow through 3D pore space can provide accurate estimates of permeability. Inputs for such simulations require detailed description of the 3D pore-structure of rocks. A digital volume required for these numerical experiments may be directly obtained by CT-scanning or statistically reconstructed from 2D thin sections.

In this dissertation, I use both natural sandstone samples and artificial sand-packs. I introduce the concept of *prototyping*, where I pack natural sand grains in the laboratory and CT-scan the pack to produce a 3D digital rock. Such prototypes may be used in lieu

of mathematically generated digital rocks to represent freshly deposited sand. Considering that most people may not have access to a 3D imaging device, I also explore statistical reconstruction of 3D digital rocks from 2D thin sections.

I investigate how digital rocks can be numerically altered to simulate diagenesis and produce porosity-permeability evolution paths. Specifically, quartz overgrowth and patchy pore-filling cementation are modeled and applied to a core from Wyoming. I show how a prototype rock can be numerically moved through geological time and also through space. Moving through time means imposing compaction and diagenesis upon prototype rock. Moving through space means altering rock to reflect diagenesis conditions away from its initial location. I show how an eolian prototype can be digitally altered to arrive at a target, which is a Permian eolian sandstone, and that the porosity and permeability of the altered prototype match these properties measured for the target.

1.2 Chapter Description

The following is a brief description of each chapter in this dissertation.

Chapter 2 introduces the concept of *prototyping*. State-of-the-art technology can simulate the deposition of spherical grains, but it is computationally expensive to deposit and pack irregularly sized and shaped grains, as seen in natural sandstone. To overcome this problem, a laboratory-packed sandstone, a prototype, consisting of actual sand grains of varying size, is used. The prototype images are then used to conduct numerical experiments, as described in the following chapters. In the following chapters, artificially packed prototypes as well as naturally consolidated sandstone are used as digital input to numerical simulations.

Chapter 3 is one application of prototypes. It addresses how permeability can be estimated from 2D images of small rock fragments, such as drill cuttings, which may be commonly available in practical situations. I select a number of natural and artificial medium- to high-porosity, well-sorted sandstone as well as prototype rocks. Relatively large 3D CT-scan volumes are obtained from each of these physical samples. Then, in a process analogous to making thin sections of drill cuttings, a large number of small, 2D slices are selected from a 3D scan. As a result, a single physical sample is used to produce hundreds of virtual-drill-cutting 2D images. Corresponding 3D pore-space

realizations are statistically generated from these 2D images, fluid flow is simulated in 3D, and a set of absolute permeability values is computed. The results show that a single and clear trend appears after cross-plotting the simulated permeability versus porosity, if the permeability is normalized by the grain size squared. This trend is common for all the physical samples under examination.

Another application for prototypes is to model evolution of porosity and permeability using numerical diagenesis on digital rocks. To illustrate this example, I introduce various types of diagenesis in Chapter 4, and show numerical implementation of diagenesis in Chapter 5. Chapters 4 and 5 focus on porosity-permeability evolution of sandstone due to diagenesis. Chapter 4 provides background information on sandstone diagenesis, especially focusing on processes to be used in the modeling of eolian sandstone diagenesis in Wyoming. Chapter 5 focuses on numerical implementation of several of the diagenetic processes introduced in Chapter 4. Specifically, quartz overgrowth and patchy cementation are modeled. All numerical diagenesis codes are applied on both 3D and 2D images.

Chapter 6 and 7 incorporate prototypes and diagenesis modeling to actual rocks from a core in Wyoming. Chapter 6 and 7 are a two-part case study into the geological evolution of eolian sandstone from the Minnelusa Formation in Wyoming. Chapter 6 provides geological background and thin-section analysis of the Minnelusa core, and suggests a diagenesis path to be modeled in Chapter 7. In Chapter 7, I incorporate the concept of prototyping and apply the numerical diagenesis model implemented in Chapter 5. I show how an eolian prototype rock, a pre-diagenesis state, can be numerically altered, thus simulating a diagenesis evolution in time. I also show how to alter rock to reflect diagenesis away from its initial location.

To solve a question of upscaling that became apparent in Chapter 7, Chapter 8 discusses how to upscale permeability computed on a small 1 mm^3 volume to a core-plug scale. Based on results in Chapter 7, the natural heterogeneity in rock, in this particular case a low-permeability zone, seems to control the effective permeability. I use several upscaling methods to see which one best describes this phenomenon.

Finally, in Chapter 9, I conclude with a summary of results and significance of the contributions made in this dissertation. I also suggest several future research directions and possible applications of the concepts and technologies introduced in this dissertation.

1.3 List of Published Papers

Contents of this thesis, especially focusing on Chapter 3 (Permeability from Thin Sections) and Chapter 5 (Numerical Diagenesis of Virtual Rocks), are published in two papers: Kameda and Dvorkin, 2004*a* and Mese et al., 2004. One paper is in review (Kameda et al., 2004). In addition, two expanded abstracts are published: Kameda and Dvorkin, 2004*b* and Kameda and Dvorkin, 2004*c*. This work has also been presented in numerous other professional conferences such as AAPG and AGU.

1.4 References

Kameda, A., and J. Dvorkin, To see a rock in a grain of sand, *The Leading Edge*, August, p.790-792, 2004*a*.

Kameda, A., and J. Dvorkin, Permeability in the thin section, *SEG Annual Meeting Abstracts*, 2004*b*.

Kameda, A., and J. Dvorkin, Permeability in the thin section, Expanded Abstract, *Australian SEG Conference*, Sydney, 2004*c*.

Kameda, A., J. Dvorkin, Y. Keehm, A. Nur, and W. Bosl, Permeability-porosity transforms from small sandstone fragments, *Geophysics*, in Review, 2004.

Mese, A., A. Tutuncu, A. Kameda, A. Nur, and J. Dvorkin, Digital rock physics for sands and shales, *Oil & Gas Network*, June, p.68, 2004.

Chapter 2
Rocks in the Virtual World

2.1 Abstract

An accurate representation of porous material in the digital space can enable researchers to conduct various numerical simulations to obtain properties such as permeability, electrical conductivity, dielectric permittivity, elastic moduli, and nuclear magnetic resonance (NMR) response. Arranging a three-dimensional matrix of zeros (pore) and ones (solid) to represent a realistic pore space is not an obvious task, as it is mathematically intractable to simulate real grain geometry and packing. State-of-the-art technology can simulate deposition of spherical grains, but it is far too complex and computationally expensive to deposit and pack irregularly sized and shaped grains as seen in natural sandstones. To overcome this problem, this chapter introduces a concept of *prototyping*. A prototype is a laboratory-packed sandstone consisting of actual sand grains of possibly varying size. These loose sand grains are taken from different depositional environments, such as coastal and eolian. The sand grains are mixed with epoxy, packed, and CT-scanned, to obtain the digital pore image. A prototype can also be a competent sample that does not need to be stabilized by epoxy. The mathematically challenging task of generating a realistic and complex pore space is thus accomplished by prototyping. The prototype images are then used to conduct numerical experiments as described in the following chapters.

2.2 Problem Formulation

Porosity and permeability are the sediment properties most relevant to the petroleum industry and environmental applications. Porosity determines how much fluid can be stored in rock, and permeability determines how fast it can flow. Permeability is arguably the most elusive bulk property of sediments. Its detailed distribution cannot be measured *in situ*. Decades of analysis of numerous laboratory data points have failed to produce rational and robust transforms between permeability and other rock properties such as porosity, lithology, and texture. The reason is the extreme variability of the pore space topology in rocks. This variability is caused by two principal factors: (a) variations in deposition and (b) variations in diagenesis. In this work, these two factors are quantitatively related to permeability by numerically simulating fluid flow in a realistic pore space. For this purpose, a 3D space occupied by porous rock can be represented by a three-dimensional matrix of zeros and ones, where zeros represent the pores and ones represent the solid (Figure 1).

The key question is how to arrange zeros and ones to represent a realistic geologic porous material. This is not an obvious task, because it is mathematically intractable to simulate *real grain* geometry and packing.

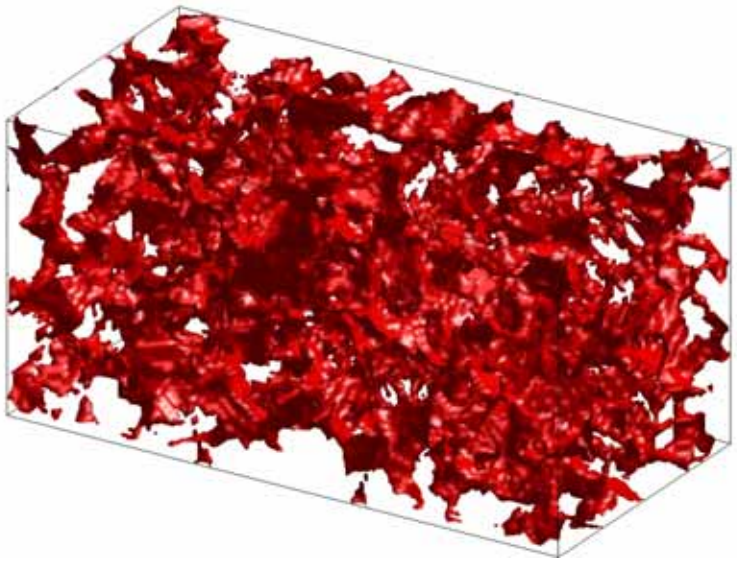

Figure 1. A three-dimensional digital pore space of Fontainebleau sandstone (Keehm, 2003). The pore space is shown in red.

2.3 Approach

Faced with a mathematical problem of accurately recreating physical sandstones in a digital world, this study takes the approach of "problem avoidance," which is an important part of problem solving (de Bono, 1992).

Instead of solving the problem you go upstream and alter the system so that the problem does not occur in the first place.

--Edward de Bono (Serious Creativity)

According to this concept, one can go upstream and create the pore space in the physical world first, then convert it to a digital representation, rather than attempting to do everything digitally and mathematically from the very beginning. Here I call this technique *prototyping*.

A prototype is a laboratory-packed sandstone, a physical mixture of differently sized grains whose size distributions mimic chosen architectural elements within a given depositional system, such as an eolian or coastal environment. Several prototypes thus created are impregnated with epoxy, CT scanned, and digitally mapped into ones and zeros in 3D. A prototype can also be a CT-scanned 3D. A prototype can also be a CT-scanned 3D image of competent, natural sandstone. Potentially, a large catalog of prototypes can be created and stored in the computer.

In the following chapters, the prototypes will be numerically altered as to simulate various diagenetic paths consistent with the initial composition and consequent burial, fluid migration, and other mechanisms. The diagenetic alteration of a prototype can be simulated mathematically by, for example, growing cement on the surface of the prototype's grains. In Chapter 7, I use an eolian prototype to see whether it can be numerically altered to match the 60 ft eolian core from a Wyoming field as a test case. If this approach is successful, prototyping, combined with numerical diagenesis tools, can simulate a site-specific rock altering process.

2.4 Previous Work

Oren and co-workers have significantly advanced the concept of pore space simulation for geologic material. For example, Bakke and Oren (1997) simulated the pore space of sandstone by placing *spheres* in 3D space. The size distribution of these

idealized grains was selected according to the grain-size distribution of realistic sandstone. Various depositional schemes helped reproduce low-energy and high-energy sedimentation as well as laminated grain-beds. Compaction and diagenesis were handled similarly to Bryant et al. (1993), where the Z-coordinate of every sphere center was shifted vertically. Overgrowth of grains was simulated by uniform expansion, similar to Bosl et al. (1998) and Keehm et al. (2001). Clay deposition was simulated by randomly placing small particles on the surface of the spheres. Fluid flow was modeled in a "ball-and-stick" network that was used to further idealize the pore space between the spheres.

By introducing and implementing the concept of prototyping, I avoid the complicated problem of virtual rock building such as described in Bakke and Oren (1997). Instead of mathematically arranging spheres in 3D and then altering their shape to make the virtual rock look realistic, I go directly to laboratory-built realistic arrangements of grains and pores.

2.5 Recipe for Virtual Rocks from the Finney Pack

Before arriving at the concept of prototypes, as a preliminary research, I altered the Finney (1970) pack to produce spherical grain packs with various sphere size distributions. I have developed a Matlab code that alters a pack of identical spheres to investigate the effect of sorting on permeability in porous media. The purpose of this investigation was to better understand the results of Beard and Weyl (1973) who show empirically that depositional texture (sorting) greatly affects the permeability and porosity of sandstones (Figure 2).

The code allows each sphere to have various sizes, thus allowing the user to control sorting and grain size (Figure 3A). The spheres are allowed to interpenetrate the neighbors much like in the numerical modeling of Bryant et al. (1993). The code allows for having various grain sizes and/or various rates of a radius increase per grain. The first results of this numerical experiment mimicked the results of Beard and Weyl (1973) that sorting is a primary controlling factor in determining porosity and permeability and that this dependence is non-linear (Figure 3B). However, while this code alters the grain size in the Finney pack, it does not re-pack the grains. The consequential loose packing configuration results in high porosity and permeability

even with poor sorting, which is not realistic for clastic rocks. There was a need to (1) adjust or deposit spheres of various sizes rather than letting the spheres penetrate each other, much like in Bakke and Oren (1997), and (2) give the grains various shapes instead of spheres. However, the mathematical task of depositing irregular 3D grains is daunting. Being able to scan actual sandstones or prototypes can help circumvent this daunting task and allow researchers to concentrate on numerical experiments on the digital rocks themselves.

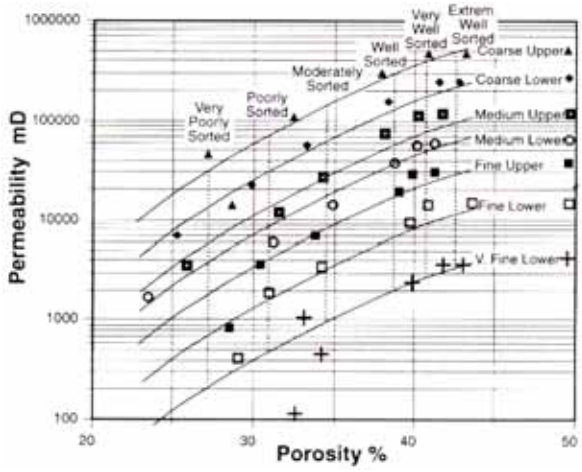

Figure 2. Porosity and permeability of sandstones of various depositional origins (Giles, 1997; data of Beard and Weyl, 1973). The data show the crucial role played by sorting and grain size (both indicated in the plot) in determining initial porosity and permeability. In this data set, other factors such as angularity and clay content play a secondary role in determining reservoir properties. Each curve has different depositional origin. Within the same depositional environment, the sorting and grain size determine porosity and permeability.

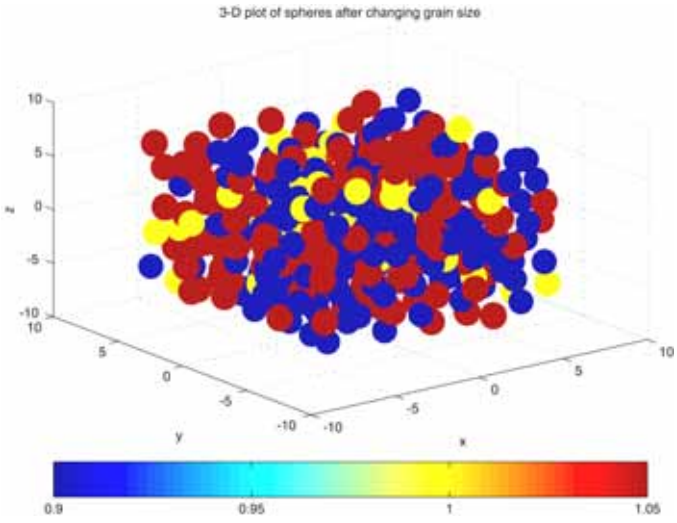

Figure 3A. 3D visualization of the Finney pack after sorting alteration. Colors indicate radius in mm.

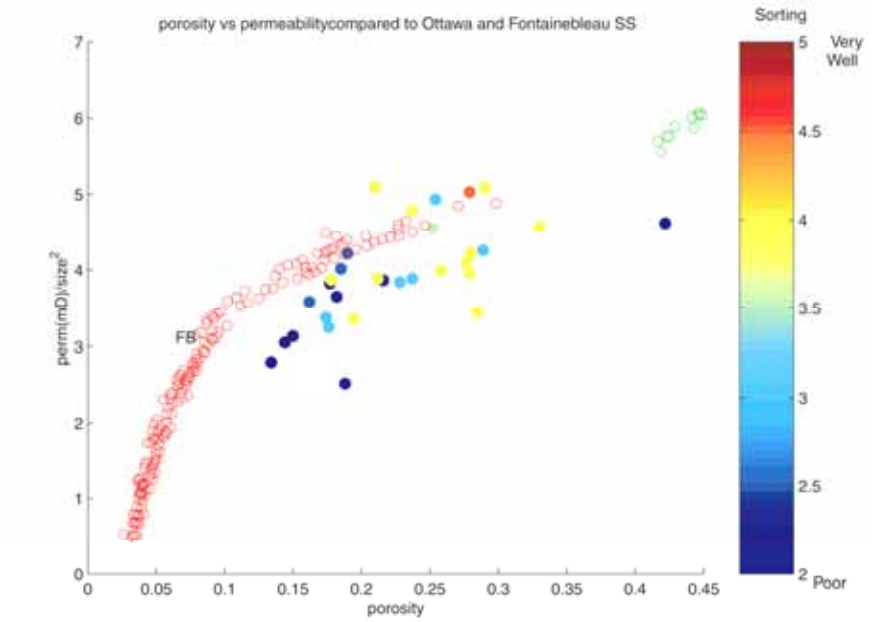

Figure 3B. Cross-plot of permeability and porosity for various altered Finney packs, with color indicating sorting. Empty red circles are Fontainebleau sandstone data (FB). The permeability values are normalized by 4 mm^2. Because spheres are altered to have different sizes but are not re-packed, some poor sorting can also mean small spheres floating loosely in the pore space, thus artificially increasing porosity and permeability. This is not a very realistic representation of naturally deposited sands.

2.6 Prototype Sample Description

This study uses loose sand grains from two depositional environments, (1) beach and (2) eolian, for producing prototypes. Beach sands were collected from a local (San Mateo County, California) coastal area, San Gregorio (SG) and Pomponio Beach (PB), and the eolian sands were collected from near the Año Nuevo coastal dune (AN) (Figures 4 and 5). Grain size analyses were conducted on all three samples (Figures 6 and 7). All the samples were moderately well sorted and had grain sizes in the medium size range.

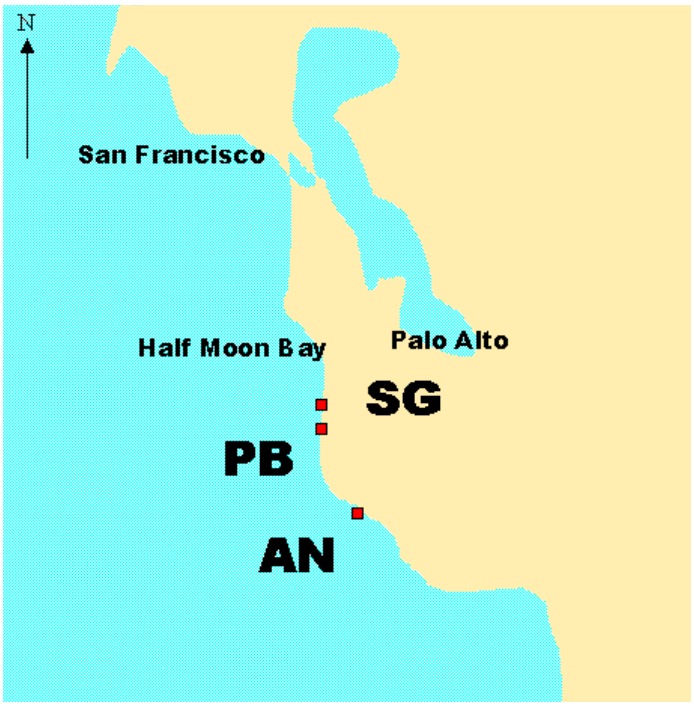

Figure 4. Map showing three beach locations, SG (San Gregorio), PB (Pebble Beach) and AN (Año Nuevo), near where samples were collected.

Figure 5. Aerial photo of a coastal dune system near Año Nuevo state beach (photo from 2002-2004 Kenneth Adelman collection in California Coastal Records Project)

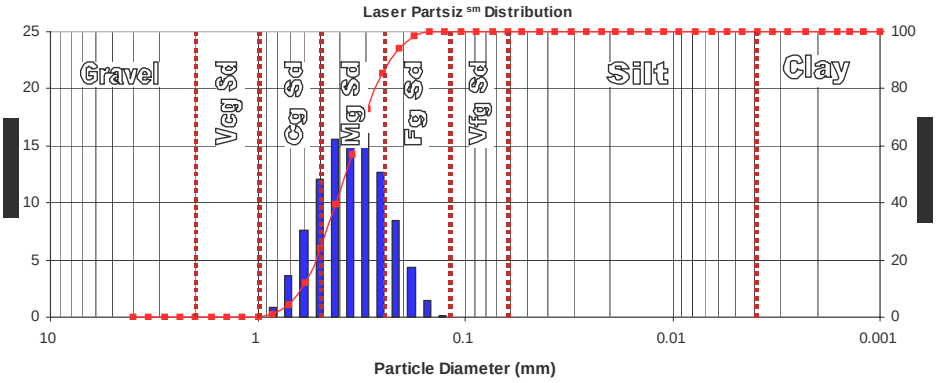

SG Sample
Folk Sorting Index 0.5592 (moderately well sorted), Mean Grain Size 392 µ

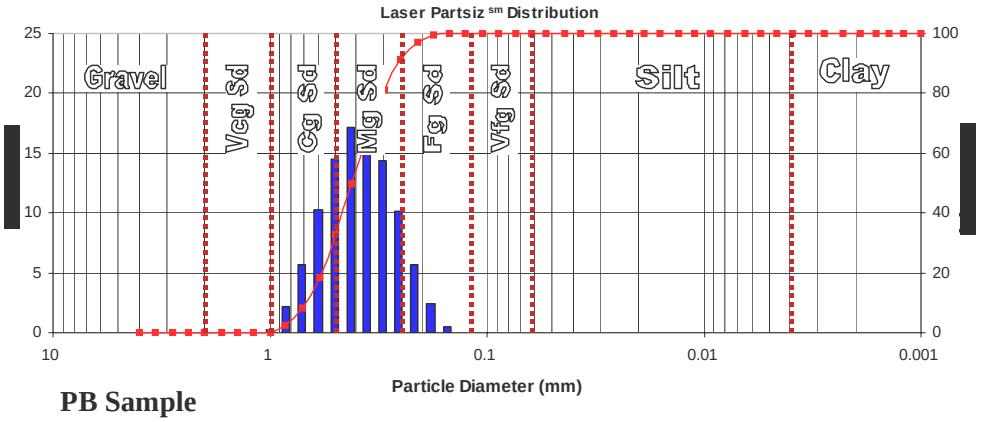

PB Sample
Folk Sorting Index 0.5548, Mean Grain Size 437 µ

Figure 6. Particle size distributions of the beach sands, SG (top) and PB (bottom). Grain densities of the samples were 2.66 g/cc for SG and 2.706 for PB. Measured lab permeability was 50 Darcy for SG and 58.4 Darcy for PB.

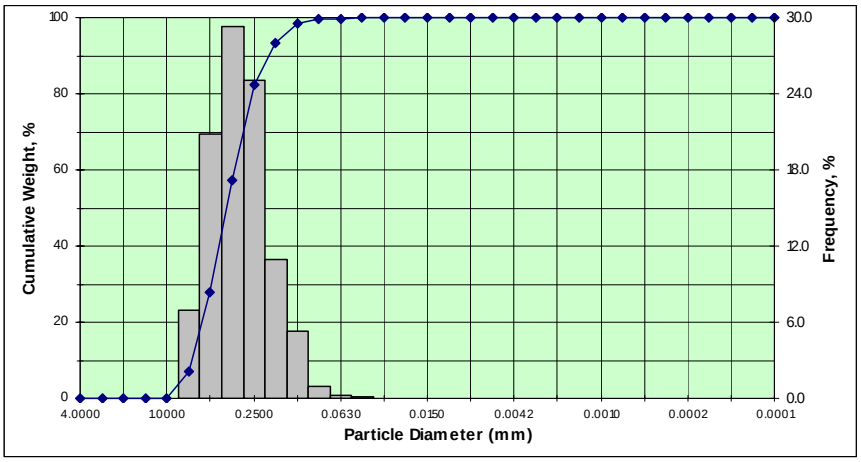

Figure 7. Particle size distribution of the dune sands AN. These sands are moderately well sorted with mean grain size 0.391 mm.

The loose sand grains were mixed in epoxy and then packed into 1 inch diameter metal tubing to produce epoxy-cemented sand-packs resembling a core plug (Figure 8). The resulting sand-packs were CT-scanned to obtain their digital pore geometry. The grain size-distribution of the beach or dune deposits is preserved in the prototype, but the original grain-distribution is no longer preserved.

Figure 8. Left: Packed eolian sand impregnated by epoxy (yellow). Right. Tomographic cross-section of the sample. The grains are white while the epoxy-filled pore space appears black.

2.7 CT-Scan

The 3D images of prototypes are digitized by High Resolution X-ray Tomography (CT-scanning). CT-scan produces multiple 2D slice-images of a rock that can then be used to reconstruct the 3D volume. Therefore, it is important to obtain consecutive CT-scan slices at high enough resolution to generate a dense array of 2D images. For example, features of interest, i.e., pore throats and cracks, can only be digitally described if the resolution is much smaller than their size.

CT scanners can be generally grouped into four categories based on their spatial resolution and the size of an object suitable for scanning, with the most common type being the conventional scanner with resolution on the order of a millimeter (Ketcham, 2001). The samples used in this study were scanned at the University of Texas, Austin, using an ultra-high-resolution (on the order of 10 micron) CT system.

The CT system used for this study can handle rock samples of up to a few cm in diameter. It employs a 200-kV microfocal X-ray source. The system's magnification increases with the specimen's proximity to the X-ray source. The system uses a fixed pixel size in the video image, which allows the user, by varying the magnification, to achieve the needed spatial resolution. The system is flexible enough to image specimens

from several cm to a few mm in diameter with spatial resolutions from ~250 μm down to ~10 μm. In addition, the ability of the microfocal source to provide a stable X-ray output, even at mean energies of 30-50 keV, permits high-quality discrimination among materials even with significant radiation attenuation. As a result, the mineral grains and epoxy can be easily discriminated from the pore space in the images of the prototypes.

Images from CT scanners have been widely used in geosciences, soil sciences and petroleum engineering for direct imaging of fluid flow in pores, as well as for detailed characterization of pore morphology. There are various commercial software packages and codes that can assist in reconstructing a 3D volume from the slices provided by the scanner and can also render these volumes in desired ways. For example, image files, such as '.jpeg' or '.tiff', can be read in digital format by using Matlab. I chose Matlab to process CT-scanned images because of the advanced image-processing tools and the flexibility of combining different user-created codes in the Matlab environment.

To process the images, I first convert the CT-scan images into bimodal images (0 and 1) and define 0 to be pore and 1 to be solid. In this study, the thresholds were set to achieve a match between the porosity of the digital sample and the physical porosity measurement. Thresholding can also be accomplished independently, from a digital image alone, using, e.g., edge detection. During flow simulation, the fluid flows only through the pore space ("zeros").

In Figures 9-18, I display 3D views as well as 2D slices of these 3D volumes of the prototype catalog collected in this dissertation work. I consider this visual display important because it provides the readers with an insight into the pore space structure of these prototypes. Each figure shows the entire volume as well as selected 2D slices in the x, y, and z directions.

Specifically, the figures show original-sized sphere packs (Figure 9), uniformly expanded sphere packs (Figures 10 and 11), a fluvial sandstone core-plug from Hibernia field (Figure 12), aeolian sandstone core-plugs from Wyoming (Figures 13 and 14), beach sand prototypes (Figures 15 and 16), a turbidite sandstone core-plug from the North Sea (Figure 17), and an aeolian sand prototype (Figure 18). Note also that the pore throat shapes are considerably more complex for natural sand-packs (Figures 12-18) than the sphere packs (Figures 9-10).

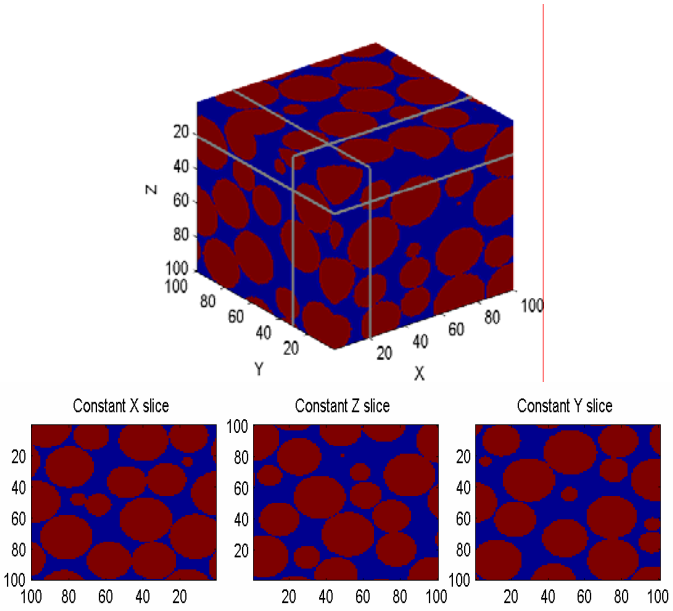

Figure 9. A sub-volume of a Finney pack (above) and its 2d slice images at x =20, y=20 and z=30. Notice that the spheres are packed randomly but the grain boundaries do not interpenetrate. The pore throats are very wide and well connected.

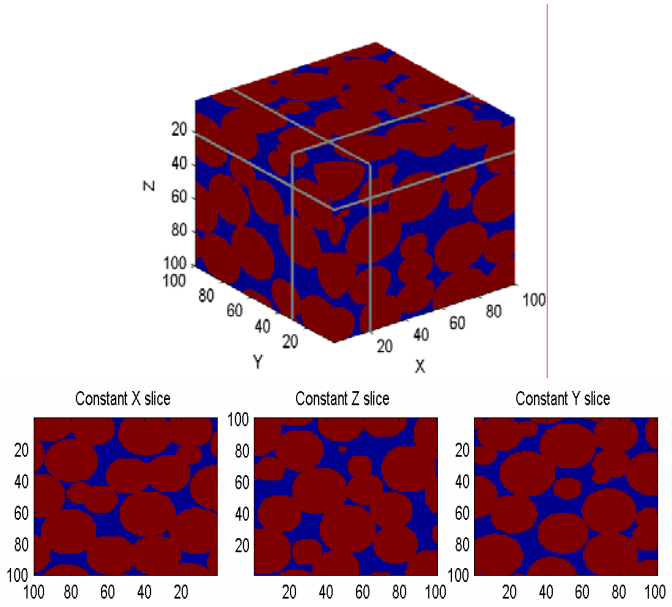

Figure 10. A sub-volume of a dilated Finney pack, where Finney spheres in Figure 9 were uniformly expanded by 3 pixels (above), and its 2d slice images at x =20, y=20 and z=30. Notice how the expanded spherical grains interpenetrate and how the structure of the pore space becomes more and more complex with narrow pore throats appearing between the grains.

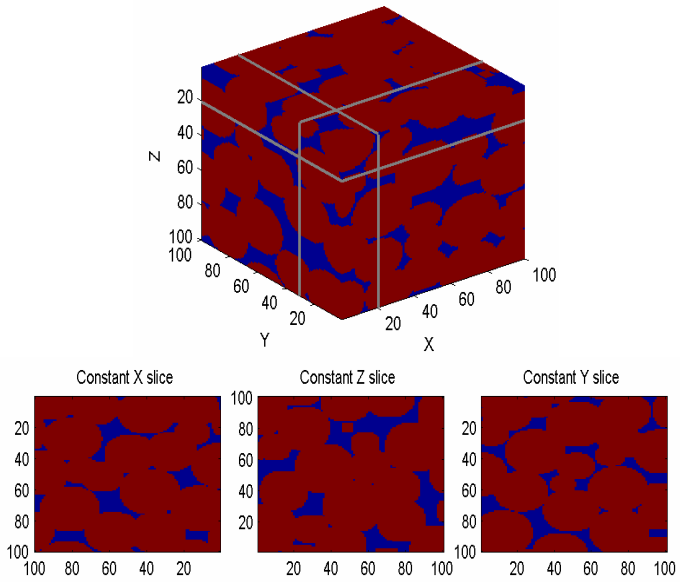

Figure 11. A sub-volume of a dilated Finney pack, where Finney spheres were uniformly expanded by 6 pixels (above), and its 2d slice images at x =20, y=20 and z=30. Notice how the expanded spherical grains interpenetrate even further than shown in the previous figure, and how the pore space becomes less connected with narrow pore throats appearing between the grains.

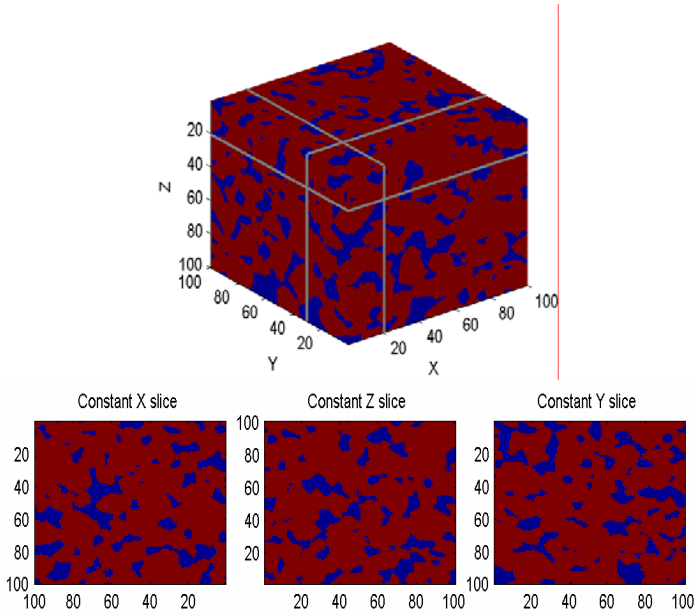

Figure 12. A sub-volume of a Hibernia fluvial sandstone core plug (above), and its 2d slice images at x =20, y=20 and z=30. Notice that the pore throats are more complex, and much narrower than that of the idealized sphere pack shown in Figure 9. The pores are also much smaller than grains.

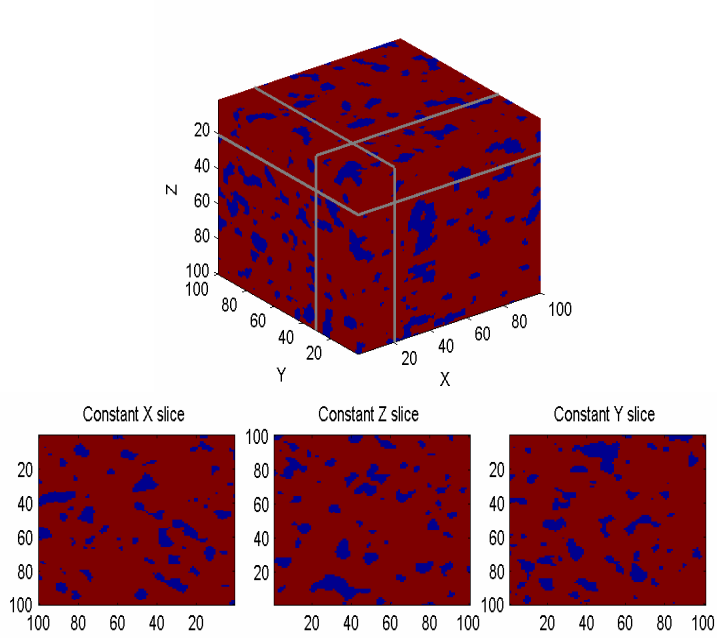

Figure 13. A sub-volume of an eolian sandstone core-plug #1 from the Minnelusa Formation, Wyoming (above), and its 2d slice images at x =20, y=20 and z=30. Notice that the porosity of this volume is much smaller (13.6 %) than that of the Hibernia sample in Figure 12 (20 %). The quartz grains in this sandstone are well cemented by quartz overgrowth and with anhydrite cements.

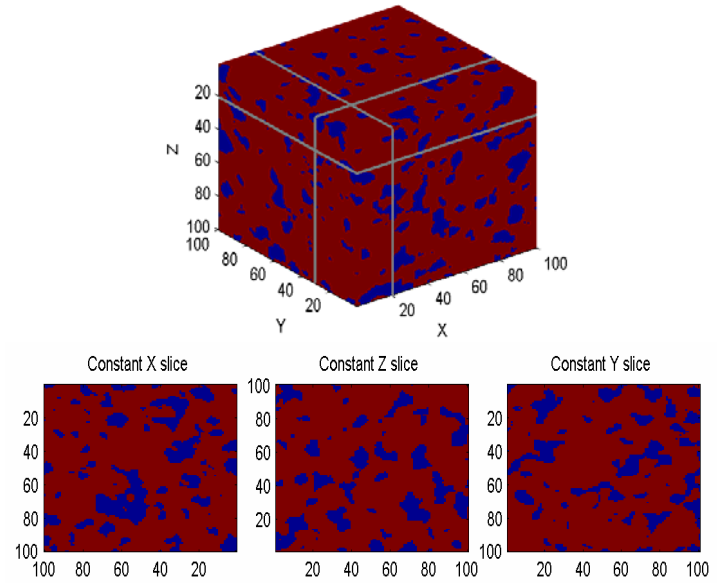

Figure 14. A sub-volume of eolian sandstone core-plug #2 from the Minnelusa Formation, Wyoming (above), and its 2d slice images at x =20, y=20 and z=30. The porosity of this volume is 16.7 %, and has less anhydrite cementation than the core-plug #1 shown in Figure 13. The pore throats are much less connected than seen in the Hibernia sample (Figure 12).

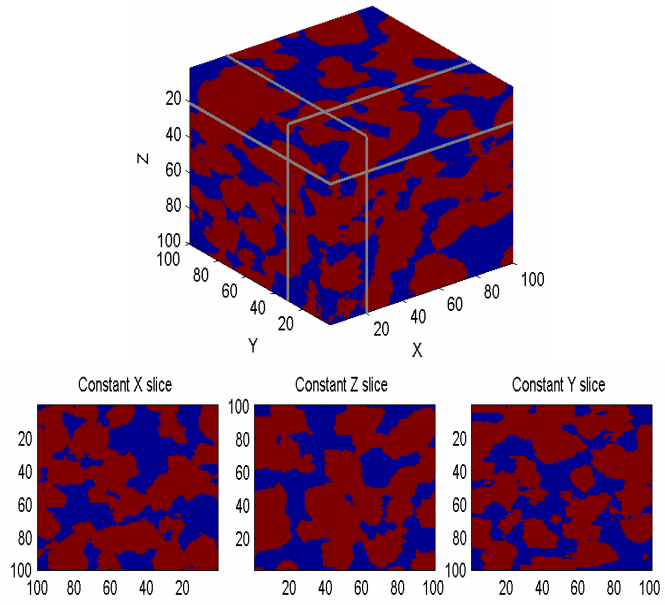

Figure 15. A sub-volume of a beach sand prototype SG (above), and its 2d slice images at x =20, y=20 and z=30. This artificial sand-pack has very loose packing compared to random sphere packs or natural sandstones (Figures 9-14).

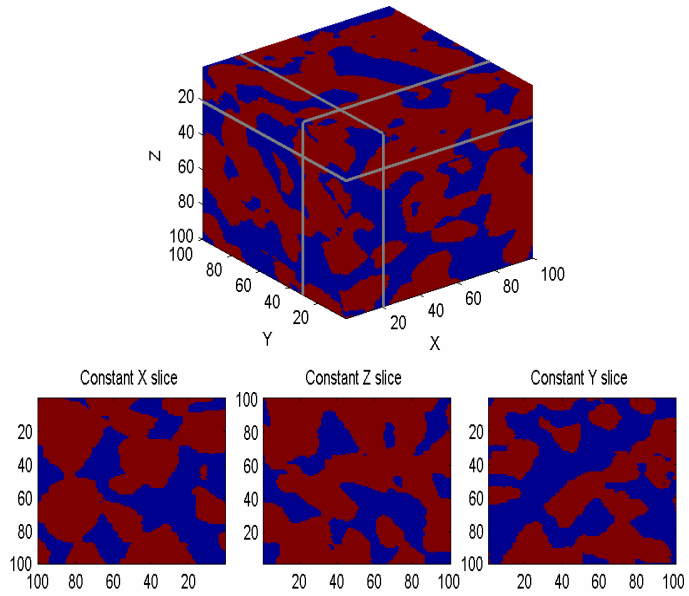

Figure 16. A sub-volume of a beach sand prototype PB (above), and its 2d slice images at x =20, y=20 and z=30. Notice that this artificial sand-pack also has very large porosity and that the pore throats are very wide.

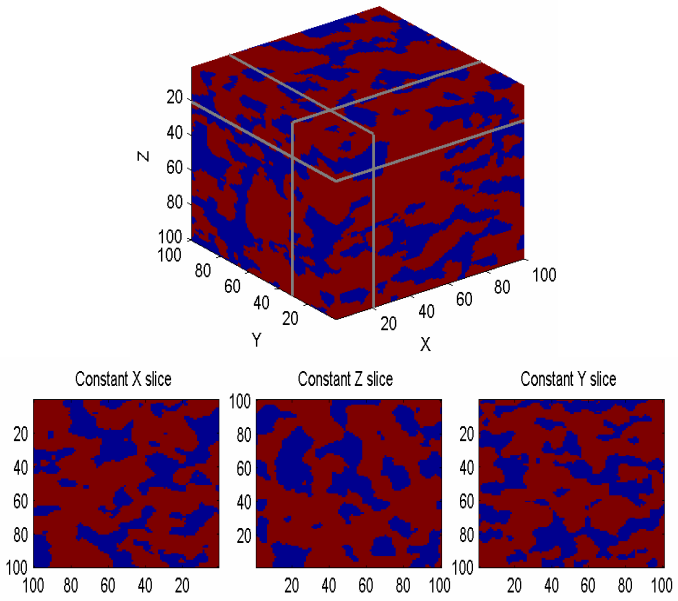

Figure 17. A sub-volume of a turbidite sandstone core-plug from the North Sea (above), and its 2d slice images at x =20, y=20 and z=30. Notice that the turbidite sandstone is not as well-sorted as the other sandstones, but the pore sizes are very large.

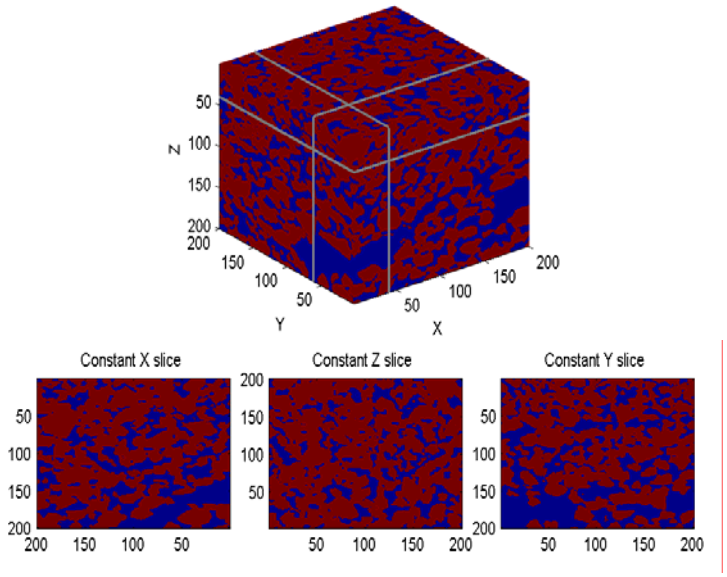

Figure 18. A sub-volume of an eolian prototype from Año Nuevo (above), and its 2d slice images at x =40, y=40 and z=60. Notice that the volume is 200 by 200 by 200 pixels rather than 100 by 100 by 100. The grains appear to be very fine because there are twice as many pixels in this display than in the other figures. Notice also that there is a large heterogeneity (a large pore structure) in this sub-volume.

2.8 Conclusion

The digital images of prototypes are created to be used for numerical fluid flow simulations to obtain permeability. Furthermore, the digital images are altered to simulate diagenesis. Creating physical sand-packs in the laboratory first, then digitizing them and altering them numerically, circumvented the overwhelming task of assembling irregular and realistic grains mathematically. This technique is simple, yet opens a wide variety of possible applications for numerical experimentation. Catalogs of prototypes from various depositional settings can serve as a library of digital pore space for various experiments and for simulating basin-specific evolution of rocks. Ideally, the prototypes are created *in situ* by pouring epoxy at the location where the grains are deposited. In this thesis, grains are re-packed in the laboratory, thus the original grain distribution is not preserved. However, the laboratory-packed prototype can still serve as a starting point to create a more natural digital rock structure, than that of the identical sphere-packs. It helps to avoid the problem of mathematically generating complicated 3D sandstone pore structure for numerical experiments.

2.9 References

Bakke, S., and P. Oren, 3-D pore-scale modelling of sandstones and flow simulations in the pore networks. *SPE Journal*, **2**, 136-149, 1997.

Beard, D.C., and P.K. Weyl, Influence of texture on porosity and permeability of unconsolidated sand: *AAPG Bull.*, **57,** 349-369, 1973.

Bosl, W., J. Dvorkin, and A. Nur, A study of porosity and permeability using a lattice Boltzmann simulation, *Geophysical Research Letters*, **25**, 1475-1478, 1998.

Bryant, S., Cade, C., and Mellor, D., Permeability prediction from geologic models: *AAPG Bull*., **77,** 8, 1338-1350, 1993.

De Bono, E., *Serious creativity: using the power of lateral thinking to create new ideas,* Harper Collins, New York, N.Y., 1992.

Finney, J., Random packing and the structure of simple liquids i. the geometry of random close packing, *Proc. Roy. Soc.*, **319A**, 479, 1970.

Giles, M.R., Diagenesis: a quantitative perspective implications for basin modelling and rock *property prediction*, Kluwer Academic Publishers, Netherlands, 1997.

Keehm, Y., *Computational rock physics: Transport properties in porous media and applications*, Ph.D. Dissertation, Stanford University, 2003.

Keehm, Y., T. Mukerji, and A. Nur, Computational rock physics at the pore scale: Transport properties and diagenesis in realistic pore geometries, *The Leading Edge*, **20**, 2, 180, 2001.

Ketcham, R.A., Acquisition, optimization and interpretation of X-ray computed tomographic imagery: applications to the geosciences, *Computers & Geosciences*, **27**, 381-400, 2001.

Chapter 3
Permeability from Thin Sections

The less toil there is, the more time and strength is left for artistic creativity.
–Small is beautiful, Schumacher, E.F., 1973.

3.1 Abstract

This chapter addresses how the permeability estimation problem could be implemented in the field by focusing on smaller, faster, cheaper solutions using virtual rock physics. Specifically, I investigate how a realistic 3D pore space can be reconstructed from small 2D images of rock, with permeability then numerically calculated from these 3D volumes by means of numerical experimentation.

Numerical simulations of fluid flow through 3D pore space can, in principle, provide accurate estimations of permeability. The digital volume required for these numerical experiments may be obtained directly by microtomography or statistically reconstructed from 2D thin sections. Such a digital pore volume has to be statistically representative of the original rock. However, only small rock fragments, such as drill cuttings, and only 2D images of those, may be practically available in the field or in storage. Can this limited input be used to estimate the permeability?

To address this problem, I select a number of natural and artificial medium- to high-porosity well-sorted sandstones. Relatively large 3D microtomography volumes (scans) are obtained from each of these physical samples. Then, in a process analogous to making thin sections of drill cuttings, a large number of small, 2D slices are selected from a 3D scan.

As a result, a single physical sample is used to produce hundreds of virtual-drill-cutting 2D images. Corresponding 3D pore space realizations are statistically generated from these 2D images, fluid flow is simulated in 3D, and a set of absolute permeability values is computed. As expected, most of these permeability values do not match the measured permeability of a physical sample, because of inherent statistical variations of pore-space geometry among the small, statistically under-representative images. However, a single and clear trend appears after cross-plotting the simulated permeability versus porosity, if the permeability is normalized by the grain size squared. This trend is common for all the physical samples under examination.

This trend is typical for clean sandstone. The simulated permeability of under-representative sandstone fragments does not match the physically measured data; instead it provides a valid permeability-porosity transform, which can be used to estimate permeability if porosity is independently known from well logs or seismic measurement.

3.2 Problem Formulation

Numerical experimentation is an attractive complement to physical measurement of rock properties. In such experiments, a physical process is simulated in a pore space and then the corresponding property is calculated. For example, a simulation of viscous fluid flow through pores provides permeability. Auzerais et al. (1996), Rothman et al. (1997), Bakke and Oren (1997), O'Connor and Fredrich (1999), and Keehm et al. (2001), among others, used pore-scale numerical methods, such as Lattice-Boltzmann and network modeling, and showed that absolute and relative permeability can be accurately estimated.

Massive and fast numerical experimentation can be used by the geoscientist and engineer in many applications, e.g., to (a) explore the effects of deposition and diagenesis on permeability by digitally altering the images of original samples; (b) estimate permeability from drill cutting and side-wall plugs which are not large enough for standard laboratory measurements; and (c) relate permeability to other properties, such as electrical conductivity, dielectric permittivity, elastic moduli, and nuclear magnetic resonance (NMR) response.

A necessary input for numerical experiments is a satisfactory digital representation of the pore space in 3D. These 3D descriptions can be obtained, for example, via X-ray tomography, with resolution as high as 5 μm, which is satisfactory for describing fine details of the pore space in most siliciclastic rocks. Another way of obtaining a digital pore space is by statistically simulating 3D pore structure from 2D images, such as thin sections. In all cases, the 3D image has to be statistically representative of the rock volume. If such images are small, we may expect a significant statistical deviation of the computed porosity and permeability from the "true" physically measured macroscopic values. Consider, for example, a sandstone thin section in Figure 1. Depending on which part of this relatively large image is sampled, the grain and pore characteristics vary, as well as the porosity, and, potentially, the simulated permeability.

There are practical situations where large images are simply not available. Examples are drill cutting, just a few grains across, or damaged rock samples, such as side-wall plugs. Even where large rock images are available, it may be more practical to deal with

small sub-samples to speed-up the computations and implement a real-time workflow on standard computer hardware.

Another practical problem is that obtaining a 3D scan of a rock fragment is still expensive and time-consuming. For example, X-ray tomography of a single sample may take a few hours. On the other hand, preparing a 2D image of a rock fragment is a cheaper and faster alternative to direct 3D scanning and is often done at the drill site.

In light of these practical problems, this chapter investigates how permeability can be estimated if only 2D images of small fragments of rock are available.

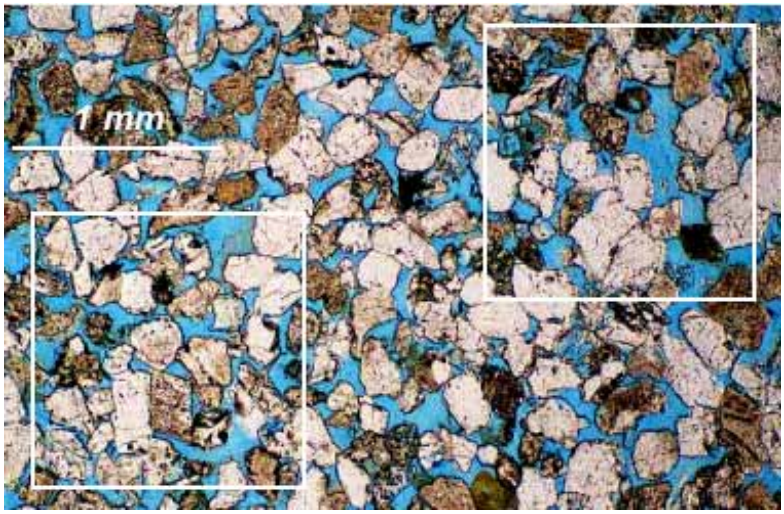

Figure 1. A thin section of a medium-porosity sandstone. The pores are shown in blue. The porosity and pore shape vary within the thin section image as seen in the highlighted squares

3.3 Hypothesis

It is most certain that the porosity and permeability of the small rock fragments will be statistically scattered around the macroscopic value measured on a large sample. Therefore, to obtain this macroscopic permeability from a single small fragment is unlikely. Instead, we investigate if there is an order in the statistical scatter of the porosity and permeability of the multiple small fragments. There may be a distinctive trend between the porosity and permeability of the fragments that, once established, can be used to estimate permeability from independent porosity data, coming from well logs or seismic remote sensing.

3.4 Workflow

3.4.1 Overview

There may be a number of practical situations where only small fragments of rock from the target interval in a well are available. These fragments may be drill cuttings collected at the surface or portions of a disintegrated side-wall plug. In this case, thin sections can be prepared from these fragments to image the pore space in 2D. It is most likely that each of these 2D images will be small and therefore will not be suitable for estimating the macroscopic porosity and permeability of the target. The goal in this chapter is to answer the core question: given that these rock fragments are available and good-quality 2D images of these fragments can be prepared, how does one estimate the macroscopic permeability?

To simulate this situation, several relatively large, high-resolution X-ray tomography 3D scans of natural and artificial sandstone samples are selected. From these scans, small 2D slices at even intervals along the plug are obtained. These slices are intended to represent 2D images of the actual rock fragments available in the field. From each 2D slice, statistical properties used to generate a 3D realization of the pore space are extracted. Finally, fluid flow is numerically simulated to obtain absolute permeability. The virtual database thus generated is analyzed.

3.4.2 Virtual Rocks: 2D to 3D

All existing methods of the reconstruction of 3D pore space are based on statistical properties of the porous medium extracted from 2D sections. An example of an object-based simulation is by Bakke and Oren (1997), who analyze the grain-size distribution in 2D and then reconstruct a 3D pack of spheres with the same size distribution as in 2D. Then they use various alteration schemes, such as cementation and clay particle deposition, to better simulate realistic sediments. Another example is by Lock et al. (2002), who represent the pore structure as a cubic network of pore tubes. The areas and perimeters of the tubes are estimated from the image-analysis of 2D sections.

Pixel-based simulation of 3D pore space is used, among others, by Yeong and Torquato (1998), who employ the 2-point probability function and the lineal path function as the morphological input. Similarly, Keehm et al. (2001) use a 3D statistical

indicator simulation, which honors the porosity and correlation length of the original 2D image. More sophisticated geostatistical methods are also available that honor not only the porosity, correlation length, and connectivity, but also the shapes of the grains and pores (Strebelle and Journel, 2001; Strebelle, 2002).

Any 2D-to-3D reconstruction will not be identical to the 3D pore structure of the original rock. However, the goal here is not to mimic the 3D rock topology but rather to accurately estimate a macroscopic physical property. Therefore, if a 3D reconstruction method leads to a correct permeability value, it is deemed appropriate for the applications discussed here.

This study adopts the pixel-based simulation of Keehm et al. (2001), which uses the porosity and the correlation length of a 2D image. A statistical generation of the third dimension from a 2D image requires that some measure of the shape, size, or scale of the pores and grains be honored. Simply reproducing the porosity of the image in uniform, randomly scattered points does not guarantee that the geometrical properties that control fluid flow are reproduced as well. This is why the correlation length, which describes the scale of pores or grains, is needed.

The porosity is computed by a point count while the correlation length is computed by a 2D Fourier transform of the image. These two parameters serve as input to the sequential indicator simulation (Deutsch and Journel, 1998). The simulation produces numerous equi-probable 3D realizations of the pore space.

This 3D reconstruction method can also simulate geometric anisotropy by assuming the horizontal-to-vertical correlation-length ratio. However, unless *a priori* knowledge of the anisotropy of the sample can be obtained, the assumption is that the rock is isotropic. The samples used in this study are isotropic, as confirmed by their variograms or correlation lengths being similar in all directions.

3.4.3 Flow Simulation

Once a 3D pore space is generated, viscous fluid flow is simulated to calculate the absolute permeability. For this purpose, this study employs the Lattice-Boltzmann (LB) algorithm, developed and used by Frisch et al. (1986), Succi et al. (1990), Chen et al. (1992), Ladd (1994), Inamuro et al. (1995), Martys and Chen (1996), Auzerais et al.

(1996), Maier et al. (1996), Rothman et al. (1997), Koponen et al. (1998), Martys et al. (1999), O'Connor and Fredrich (1999), Arns et al. (2001), Halliday et al. (2001), and Keehm et al. (2001), among others. LB is most appropriate for this application, because it can simulate slow, viscous fluid flow without any idealization of the complex pore structure.

LB describes fluid motion as collisions of imaginary particles that are larger than the real fluid molecules but show almost the same flow behavior at the macroscopic scale. While other methods, such as network modeling, the finite-element method, and the finite-difference method, discretize either the geometry or the governing equations, LB recovers the governing Navier-Stokes equations from the collision rules between the particles that move on a lattice. If the lattice is fine enough, LB can be readily implemented on an arbitrary pore geometry, without its idealization. A detailed description of the implementation of LB for single-phase fluid flow can be found in Keehm (2003).

3.5 Data Description

A number of medium- to high porosity clean sandstones are selected as a test case for the hypothesis. This is the first step toward investigating the applicability of the workflow. Only after the workflow is validated on simple porous systems, can it be tested on more complex natural rocks, such as shaly and tight sandstones and carbonates.

The test bed for most of the published methods of permeability estimation is the historic Fontainebleau sandstone dataset (see Bourbie and Zinszner, 1985, for data description). This dataset is publicly available and spans a large porosity and permeability range. The relation between porosity and permeability in Fontainebleau is well defined (Figure 2). One reason for this distinct trend is that the Fontainebleau samples are extremely clean and well sorted, consisting of 99.8 % quartz. After deposition, the sands underwent quartz overgrowth in different degrees, which produced a large span of porosity among the samples.

In spite of its uniqueness, the Fontainebleau dataset is relevant to hydrocarbon-bearing reservoir sandstones. Examples shown in Figure 2 indicate that several oil and gas reservoirs exhibit permeability-porosity trends similar to that of the Fontainebleau.

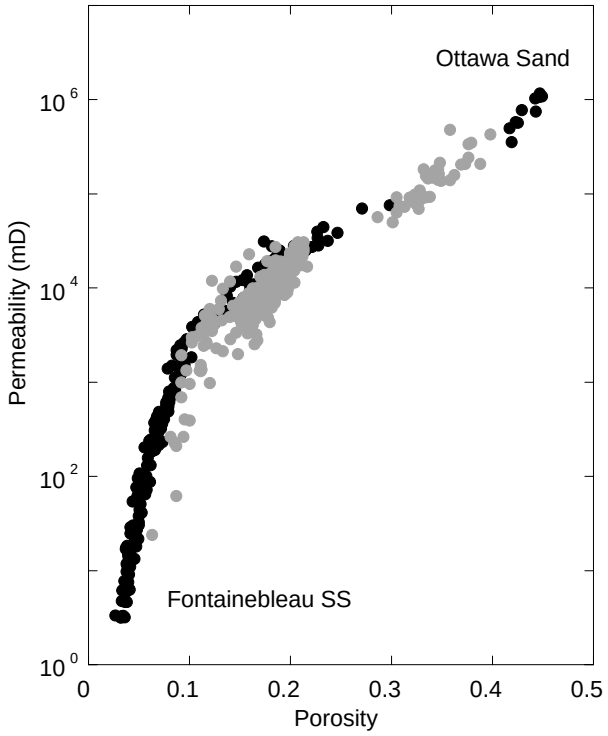

Figure 2. Permeability (mD) versus porosity in Fontainebleau sandstone (black) and Ottawa sand (black) compared with several hydrocarbon reservoir sands (gray).

This study uses 3D X-ray microtomography datasets from four natural sandstones, two artificially packed beach sand samples, and a 3D digital description of Finney's (1970) sphere pack. The original microtomography images come in gray-scale. The grains can be easily distinguished from the pores due to the large density contrast, even when the pore space is filled with epoxy, as in the beach sand samples. By setting a threshold on a gray-scale image, I convert it into a black-and-white image. In this study, the thresholds were set to achieve a match between the porosity of the digital sample and the physical porosity measurement. Binary conversion of images can also be accomplished independently, from a digital image alone, using, for example, edge detection. There is no universal threshold that works with all the samples. Each sample has unique density contrast and grain shapes, and the resolution of the grain boundaries is highly dependent on the shape of the sample itself. Therefore, one must use some criteria to decide which threshold to use, such as setting the threshold to arrive at the measured porosity value. If porosity is unknown in advance, then other criteria must be used, such

as automated edge detection using Matlab or other similar image analysis software, or by visual inspection.

The four natural sandstone samples are: Fontainebleau; a moderately well-sorted, high-energy, fluvial sandstone from the Hibernia offshore field; two clean eolian sandstone samples from the Wildcat field in Wyoming; and a turbidite sandstone from a North Sea oil field. Two artificially packed samples consist of beach sand from San Gregorio (SG) and Pomponio Beach (PB) from the Northern California coast. The beach sand samples were impregnated with epoxy and then hand-packed in the laboratory (Figure 3). The properties of the samples are summarized in Table 1. The measured large permeability of some of the samples is due to their large grain size. The tomography resolution (Table 1), defined here as the distance between two consecutive slices in X-ray microtomography images, is satisfactory because it is much smaller than the grain size.

The original volumes scanned by microtomography were on the order of a centimeter. For example, the Hibernia plug was 20 mm in diameter and 10 mm in height, which amounted for about 100 million pixels. For this study, I selected cubes of 100^3 pixels from different parts of the digitized volumes. Each of these cubes is, in essence, a stack of one hundred 2D slices acquired along the physical sample at even intervals of the scan resolution, as shown in Figure 4.

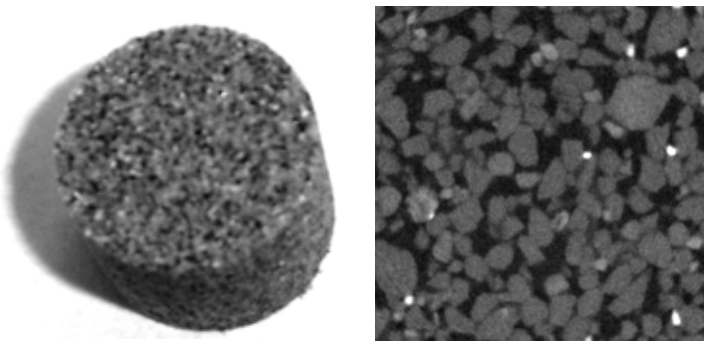

Figure 3. Left: Packed beach sand impregnated by epoxy. Right: Tomographic cross-section of the sample. The grains are light gray while the epoxy-filled pore space appears black.

Table 1. Properties of samples used in this study. For all samples, except the Finney pack, the average grain diameter was measured in the laboratory or numerically estimated from a digital image; porosity and permeability were measured in the laboratory or computed from a large 3D digital image. Resolution is the distance between two consecutive slices in X-ray microtomography images.

Sample	Grain Size (mm)	Porosity	Permeability (D)	Resolution (mm)
Fluvial SS from Hibernia	0.680	0.200	5.700	0.03910
Eolian Fontainebleau SS	0.250	0.150	1.000	0.00750
Eolian SS from Wyoming 1	0.250	0.136	0.666	0.01578
Eolian SS from Wyoming 2	0.250	0.162	1.300	0.01578
Turbidite SS from North Sea	0.390	0.347	32.039	0.01578
Artificial beach sand pack SG	0.392	0.390	50.000	0.01470
Artificial beach sand pack PB	0.437	0.340	58.400	0.01470
Finney Pack	2.000	0.360	159.000	N/A

For each sample, such stacks of one hundred 2D slices were selected and then used to calculate the porosity and correlation length, stochastically reconstruct the 3D pore space, and then compute the absolute permeability by means of LB simulation. As a result, for each of the selected cubical sub-volumes, we obtained 100 image slices, 100 reconstructed 3D pore space volumes, and 100 computed porosity and permeability data points.

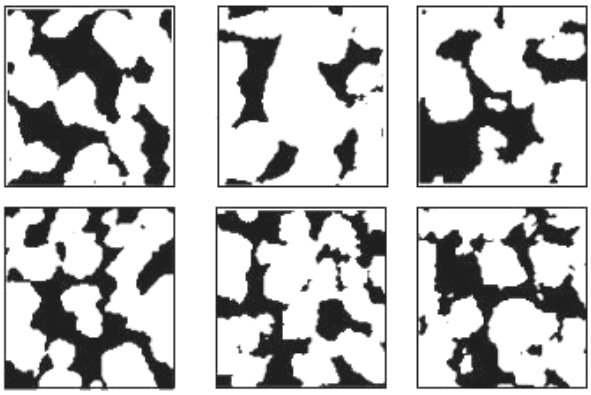

Figure 4. 2D slices of the PB (top) and SG (bottom) beach sand samples. Here, only three slices from each CT-scan are shown. The CT-scan actually consists of hundreds of such image slices per sample.

3.6 Results

3.6.1 Fluctuations of Properties

Figure 5 displays the computed porosity and permeability for 100 consecutive 2D slices for some of the samples. For each case, including those not displayed in Figure 5,

there is a significant fluctuation of the calculated porosity around the mean value (the latter being very close to the measured porosity as shown in Table 1). The same is true for the calculated permeability.

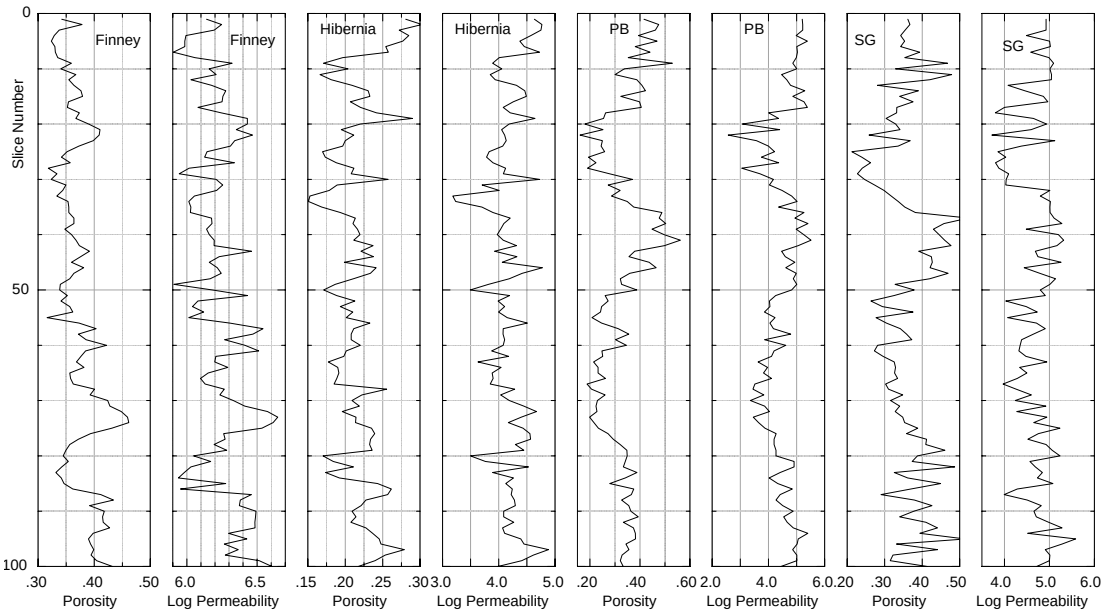

Figure 5. Profiles of porosity and permeability (mD) as calculated from 2D slices for four samples. The vertical axis corresponds to depth along each core and is marked by the slice number. From left to right: the Finney pack, Hibernia, PB, and SG.

3.6.2 Sample Cube Size and Resolution

In general, the smaller the sample size, the larger the fluctuation. This effect is illustrated in Figure 6, where the size of the 3D sampling cube in a Finney pack was gradually increased. Scale-related fluctuation in both porosity and permeability is evident where the sampling size is small. Once the cube size exceeds two-grain diameter, the fluctuation becomes negligible.

The fluctuation of porosity and permeability values computed in our statistically generated digital rock samples (Figure 5) implies that the selected small 2D images are not statistically representative of the rock. Therefore, the "true" porosity and permeability *cannot* be consistently reproduced from a small portion of a thin section.

In addition to the sample size, one must consider the effects of image resolution (pixel size) on computed permeability. In general, coarse gridding or poor resolution leads to an over-estimation of permeability due to an excessively coarse simulation of

laminar flow through the pore space (Figure 7). When different resolutions are used to compute flow through a Finney pack, for example, the porosity-permeability curves start out above the Fontainebleau curve. However, they shift down toward the correct trend as the resolution improves and, eventually, the simulated curve merges with the Fontainebleau curve (Figure 8). When different resolutions are used to compute flow in digital rocks reconstructed from CT-scanned images of a single Fontainebleau sample, the coarse gridding results in a large scatter (or fluctuation) of the computed permeability and porosity values (Figure 9). However, unlike the simple pore space of a spherical pack, such as the Finney pack, this natural sandstone pore space has an unexpected property: higher resolution leads to a deviation of the permeability-porosity curve in the lower porosity range.

This may be due to an artifact of the geostatistical code employed in this study that honors correlation length (pore scale) and porosity, but does not describe the shape of the pore throat. At a lower porosity range, accurately describing a pore-throat shape may be more critical. This problem is inherent in the workflow that incorporates a geostatistical code to generate 3D digital rock volumes from 2D images. This problem can be addressed by altering the geostatistical approach used in this work.

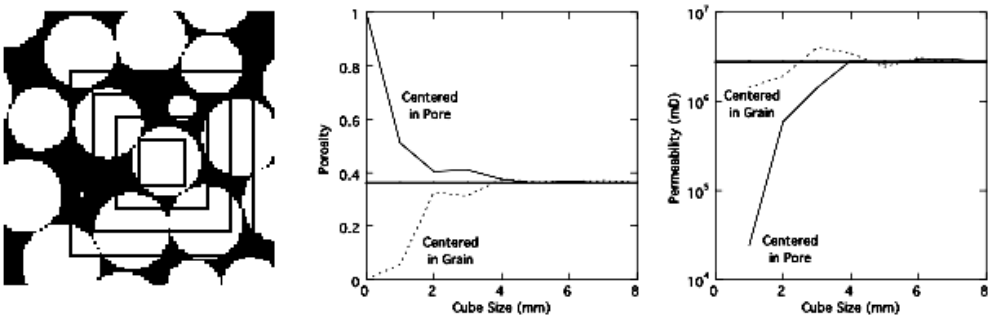

Figure 6. The effect of the cube size on porosity and permeability in the Finney pack (after Bosl et al., 1998). Left: A cartoon showing a thin section image of the Finney pack with expanding sampling size. The sampling cubes can be centered in a pore or in a grain. The Finney pack porosity is 0.36, but when the sampling size is small the porosity can be as low as 0 (pore space) or as high as 1 (grain). Center: The computed porosity. Right: The computed permeability. Both porosity and permeability converge at the macroscopic values of the entire pack (shown as the horizontal lines) after the cube size exceeds about 4 grain radii.

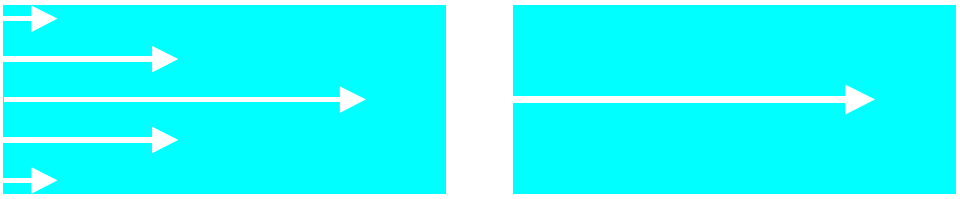

Figure 7. Schematic figures showing the effect of gridding on computing laminar flow via Lattice-Boltzmann simulation. Left: Fine gridding accurately describes laminar flow (white arrow) in the pore space (blue). Right: Coarse gridding can only describe the maximum flow in the pore space, thus over-estimating the permeability.

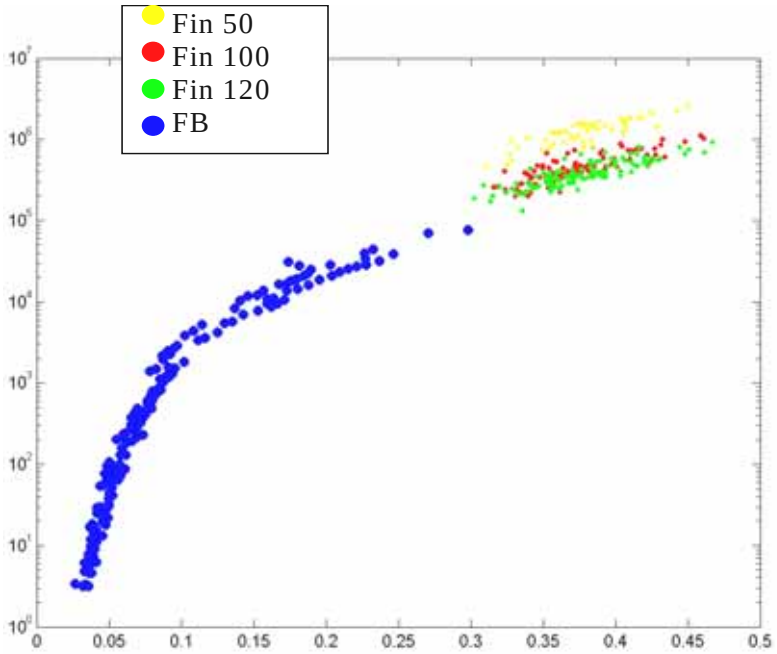

Figure 8. The effect of resolution or the pixel size (50^3, 100^3, and 120^3) on porosity and permeability in the Finney pack compared to Fontainebleau data set. The 50 by 50 by 50 cube has a coarse grid and over-estimates permeability. As the resolution gets better, permeability estimates become consistent with that of the Fontainebleau curve (FB).

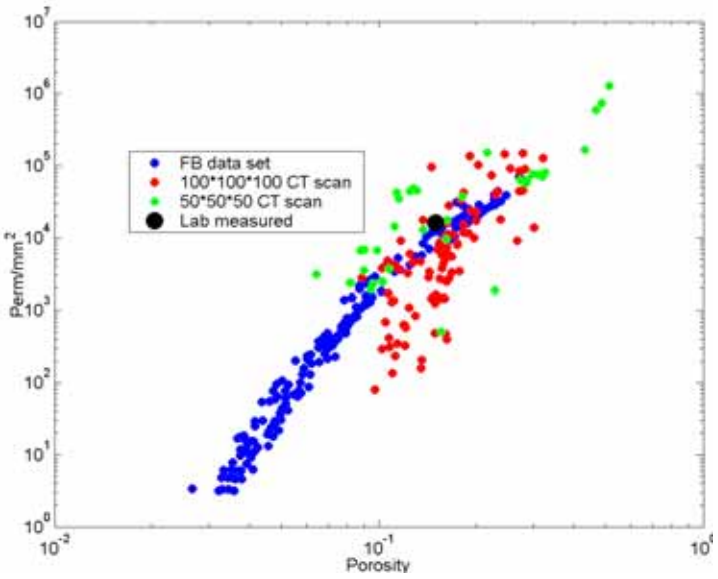

Figure 9. The effect of resolution on a CT-scanned Fontainebleau sample. Blue data points are Fontainebleau dataset (FB) measured in the laboratory. Green points are geostatistically generated digital rock permeability computed on a 50 by 50 by 50 CT-scanned sample of a Fontainebleau sandstone. Red points are permeability values computed on the 100 by 100 by 100 CT-scanned sample. Note the coarser gridding (green) produces larger scatter in porosity and permeability than the finer grid (red). Also, The finer grid results (red) deviate from Fontainebleau curve (blue) in the lower porosity range. At this point, it is not clear whether the observed deviation is a numerical artifact or a physical phenomenon.

3.6.3 Cross-Plots of Results

Next, the computed porosity and permeability are cross-plotted. In Figure 10, these cross-plots are superimposed upon reference data for Fontainebleau sandstone and Ottawa sand (Estes, 1994). The permeability is normalized by the grain size squared.

Figure 10a illustrates the results for the Finney pack. Most of the computed data points deviate from the sample's "true" porosity and permeability, shown as a large green symbol. In spite of the strong fluctuation among the computed values, their cross-plot forms a distinctive trend that connects with the laboratory Fontainebleau and Ottawa trends.

Additionally, by altering the Finney pack I create three new digital samples. Specifically, the original Finney pack grains are uniformly expanded, thus producing lower-porosity samples with macroscopic porosities 0.258, 0.163 and 0.109. The same procedure is used as for the original Finney pack. The resulting permeability-porosity trends are shown in Figure 10a in orange, brown, and yellow, respectively. All these data

still form a tight trend that continues the trend observed on the original Finney pack into the lower-porosity domain and matches the laboratory Fontainebleau trend. This result is far from trivial, because each data point in these trends was calculated from a small, under-representative 2D image of the original sample.

Similarly, this study examines a number of sandstone samples, starting with a turbidite sample from a hydrocarbon-producing field in the North Sea (Figure 10b, red symbols). The simulation results are very similar to those shown in Figure 10a. As expected, most of these data points do not match the sample's "true" porosity and permeability. However, the scatter plot forms a distinctive trend that connects with the laboratory Fontainebleau and Ottawa trends.

Similar results are reproduced for other sand samples from different depositional environments: fluvial sandstone from the Hibernia field (Figure 10c); eolian sandstones from Wyoming (Figure 10d); and artificially packed beach sands from California (Figure 10e).

The final frame in Figure 10 displays the results for a single medium-porosity (0.15) Fontainebleau sample (Keehm, 2003) that was scanned and digitized. The trend formed by the porosity and permeability computed from small 2D slices of this sample deviates from the laboratory Fontainebleau trend in the low-porosity domain. A similar behavior can be observed in Figure 10d for the lower-porosity eolian sample. Moreover, laboratory data trends shown in Figure 2 also deviate from the Fontainebleau trend in the low-porosity range. At this point, it is not clear whether the observed deviation is a numerical artifact or a physical phenomenon.

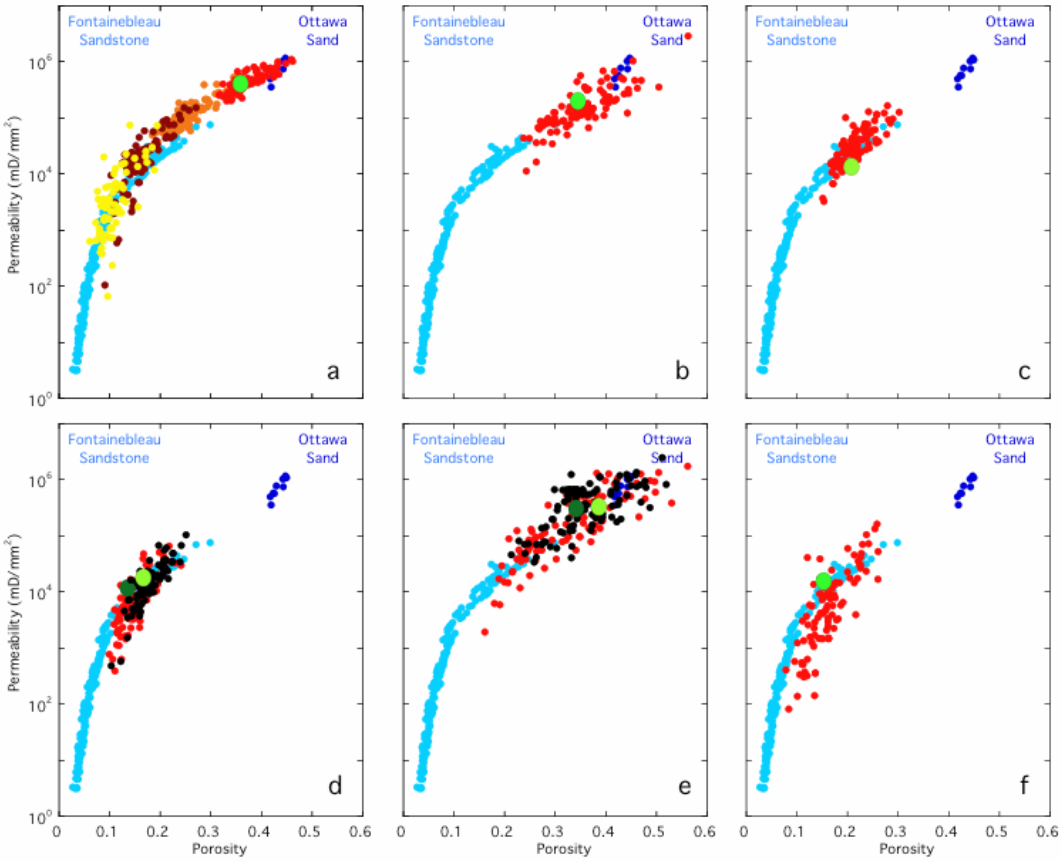

Figure 10. Permeability, normalized by the grain size squared, versus porosity for digital samples under examination. (a) Finney pack (red, orange, brown, and yellow); (b) turbidite sandstone from the North Sea (red); (c) fluvial sandstone from the Hibernia field (red); (d) eolian samples from Wyoming (red and black); (e) artificially packed beach sand samples PB (red) and SG (black); and (f) a scanned Fontainebleau sample (red). Large green circles show porosity and permeability for each 3D sample, as given in Table 1. Where more than two samples are displayed, the tabulated data are shown as dark-green (for red-color trends) and light-green (for black-color trends) symbols. In all frames, laboratory data trends are shown for Fontainebleau sandstone (light-blue) and Ottawa sand (dark-blue).

These results indicate that while the "true" porosity and permeability cannot be reproduced from small, statistically under-representative, 2D images, a valid permeability-porosity trend can still be established. This result has an important practical implication: in medium- to high-porosity well-sorted sandstones, a permeability-porosity trend can be obtained from small rock fragments unsuitable for standard laboratory measurements. Then this trend can be used to assess permeability from porosity, which may be independently estimated from log or seismic data.

3.7 Discussion

The results of the numerical simulation indicate that all simulated data points fall very close to the trend outlined by the Fontainebleau and Ottawa sand laboratory data. The same trend can be expressed by the historic Kozeny-Carman equation (Carman, 1961), which was modified by Mavko and Nur (1997) to include the effect of the percolation threshold at low porosity:

$$k = \frac{1}{72}\frac{(\phi-\phi_p)^3 d^2}{[1-(\phi-\phi_p)]^2\tau^2} = \frac{1}{2}\frac{(\phi-\phi_p)^3}{S^2\tau^2}, \quad (1)$$

where k is permeability; d is the average grain diameter; ϕ is porosity; ϕ_p is the percolation porosity; τ is the tortuosity; and S is the specific surface area. The specific surface area is related to the grain diameter as $S = 6(1-\phi)/d$. The geometric factor that accounts for the shape of the pore cross-section is expressed in this equation by the coefficient 1/72. Of course, this coefficient may vary to reflect the variability of the pore shape. The tortuosity can also vary to reflect the geometry of the pore space. Here I use τ = 3.5, 2.5 and τ = 1.5. I also fix the percolation porosity ϕ_p at 0.02. These curves are plotted in Figure 11a, together with all data from Figure 10.

Another class of equations, such as by Tixier (1949), Wyllie and Rose (1950), and Timur (1968), link permeability to porosity and irreducible water saturation S_{wi}. Timur's equation is

$$k = 0.136\frac{\phi^{4.4}}{S_{wi}^2}, \quad (2)$$

where permeability k is in mD and porosity ϕ and irreducible water saturation S_{wi} are both in %. I superimpose Equation 2 upon all data points and find that the best fit is achieved for S_{wi} = 0.07 (Figure 11b). Of course, this S_{wi} is data-specific and should not be taken as a universal value.

The Kozeny-Carman and Timur curves accurately describe the data. This is in spite

of the fact that the Kozeny-Carman functional form was derived from a highly idealized representation of a pore space as a set of pipes. Nevertheless, the equations seem to accurately predict the permeability of many natural types of sandstone, if the constants (the geometrical factor, tortuosity, grain size, percolation porosity, and irreducible water saturation) are appropriately selected. This conclusion is supported by Blair and Berryman (1992) who calculated the tortuosity and specific surface area by image processing of 2D thin sections and then used the Kozeny-Carman equation to accurately predict permeability in sandstones. The numerical-experiment data trends generated in this study are corroborated by laboratory data (Fontainebleau and Ottawa) and also by simple theoretical (Kozeny-Carman) and empirical (Timur) equations.

This conclusion definitely holds for clean, well-sorted, medium- to high-porosity sandstones. It is not clear yet whether the same approach will be valid to determine permeability-porosity trends for poorly sorted and/or clay-rich clastics or other rock types. This question can be addressed by further numerical experimentation on natural and digitally produced porous media. For example, a large 3D pore-space volume can be digitally populated by smaller (clay) particles. Then small 2D slices can be produced to conduct the procedure described here.

Notice that the trend obtained for a medium-porosity (0.15) Fontainebleau sample (Figure 10f) deviates from the experimental Fontainebleau trend in the low-porosity range. It is not clear whether this is a numerical artifact or physical phenomenon. If this is a numerical artifact, it may be because the pore-space connectivity is not fully described by 2-point statistics which introduces a significant underestimation of permeability in the low-porosity range. The issue can be resolved by testing different geostatistical methods of 2D-to-3D simulation, such as a multi-point statistical algorithm by Strebelle and Journel (2001), that may better simulate grain shapes and connectivity in the low-porosity domain.

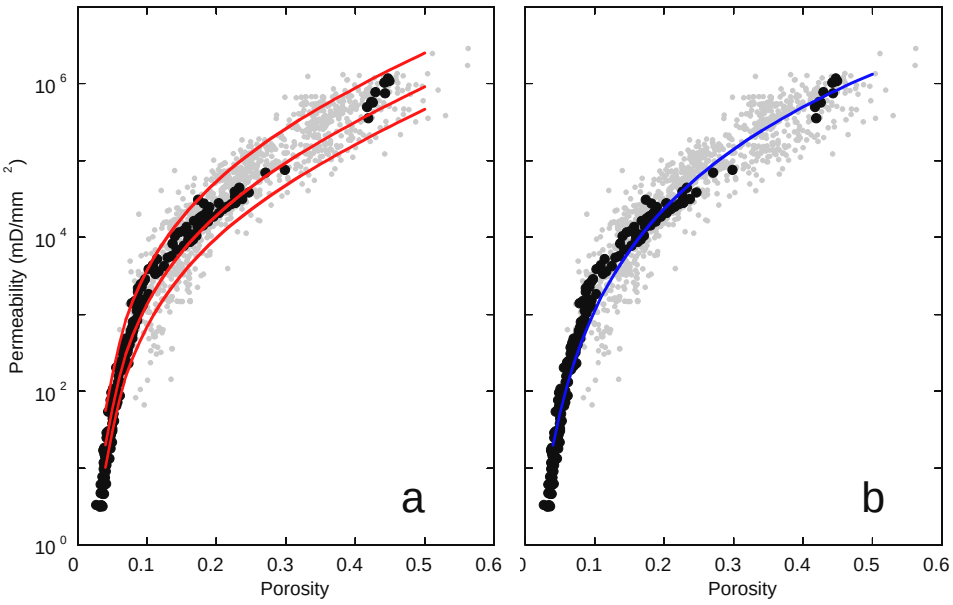

Figure 11. Permeability, normalized by the grain size squared, versus porosity for all simulations from Figure 10 (gray symbols), as well as the Fontainebleau sandstone and Ottawa sand laboratory data (black symbols). a) The Kozeny-Carman curves for tortuosity 1.5, 2.5, and 3.5 are shown in red. b) The Timur curve is shown in blue.

3.8 Conclusion

Small fragments of medium- to high-porosity sandstones that are not statistically representative of a larger sample cannot be used to numerically calculate the exact porosity and permeability of the sample. Nevertheless, by using a significant number of small fragments, one can obtain a valid permeability-porosity trend, which can be used to estimate the absolute permeability from independent porosity data.

3.9 References

Arns, C.H, M.A. Knackstedt, W.V. Pinczewski, and W.B. Lindquist, Accurate estimation of transport properties from microtomographic images, *Geophysical Research Letters*, *28*, 17, 3361-3364, 2001.

Auzerais, F.M., J. Dunsmuir, B.B. Ferreol, N. Martys, J. Olson, T.S. Ramakrishnan, D.H. Rothman, and L.M. Schwartz, Transport in sandstone: A study based on three dimensional microtomography, *Geophys. Res. Letters*, **23**, 705-708, 1996.

Bakke, S., and P. Oren, 3-D pore-scale modelling of sandstones and flow simulations in the pore networks. *SPE Journal*, **2**, 136-149, 1997.

Blair, S.C., and J. G. Berryman, Permeability and relative permeability in rocks, *Fault Mechanics and Transport Properties in Rocks*, Academic Press, London, 169-186, 1992.

Bosl, W., J. Dvorkin, and A. Nur, A study of porosity and permeability using a lattice Boltzmann simulation, *Geophysical Research Letters*, **25**, 1475-1478, 1998.

Bourbie, T., and B. Zinszner, Hydraulic and acoustic properties as a function of porosity in Fontainebleau Sandstone, *Journal of Geophysical Research*, **90**, 13, 11,524-11,532, 1985.

Carman, P.C., L'écoulement des gaz à travers les milieux poreux. Bibliothèque des Sciences et des Techniques nucléaires, P.U.F., 52, 1961.

Chen, H., S. Chen, and W.H. Matthaeus, Recovery of the Navier-Stokes equations using a lattice-gas Boltzmann method, *Phys. Rev. A*, **45**, 5339-5342, 1992.

Deutsch, C.V., and A.G. Journel, *GSLIB: Geostatical Software Library and User's Guide*, Oxford University Press, New York, 369, 1998.

Estes, C.A., G. Mavko, H. Yin, and T. Cadoret, Measurements of velocity, porosity, and permeability on unconsolidated granular materials, *Stanford Rock Physics and Borehole Geophysics Project Annual Report*, **55**, G1-1 – G1-9, 1994.

Finney, J., Random packing and the structure of simple liquids, I. the geometry of random close packing, *Proc. Roy. Soc.*, **319A**, 479, 1970.

Frisch, U., B. Hasslacher, and Y. Pomeau, Lattice-gas automata for the Navier-Stokes equation, *Phys. Rev. Lett.*, **56**, 1505-1508, 1986.

Halliday, I., L.A. Hammond, C.M. Care, K. Good, and A. Stevens, Lattice Boltzmann equation hydrodynamics, *Phys. Rev.*, E, **64**, 011208, 2001.

Inamuro, T., M. Yoshino, and F. Ogino, A non-slip boundary condition for lattice Boltzmann simulations, *Phys. Fluids*, **7**, 2928-2930, 1995.

Keehm, Y., *Computational rock physics: Transport properties in porous media and applications*, Ph.D. Dissertation, Stanford University, 2003.

Keehm, Y., T. Mukerji, and A. Nur, Computational rock physics at the pore scale: Transport properties and diagenesis in realistic pore geometries, *The Leading Edge*, **20**, 2, 180, 2001.

Koponen, A., D. Kandhai, E. Hellén, A. Alava, A.G. Hoekstra, M. Kataja, K. Niskanen, P. Sloot, and K. Timonen, Permeability of three-dimensional random fiber webs, *Phys. Rev. Lett.*, **80**, 716-719, 1998.

Ladd, A.J.C., Numerical simulations of particulate suspensions via a discretized Boltzmann equation: Part 1. Theoretical foundation, *J. Fluid. Mech.*, **271**, 285–309, 1994.

Lock, P.A., X. Jing, and R.W. Zimmerman, Predicting the permeability of sandstone from image analysis of pore structure, *Journal of Applied Physics*, **92**, 10, 6311-6319, 2002.

Maier, R.S., R.S. Bernard, and D.W. Grunau, Boundary conditions for the lattice Boltzmann method, *Phys. Fluids*, **8**, 1788-1801, 1996.

Martys, N.S., J.G. Hagedorn, D. Goujon, and J.E. Devaney, Large scale simulations of single and multi-component flow in porous media, *Proc. SPIE*, **3772**,205-213, 1999.

Martys, N.S., and H. Chen, Simulation of multicomponent fluids in complex three dimensional geometries by the lattice Boltzmann method, *Phys. Rev. E*, **53**, 743-750, 1996.

Mavko, G., and A. Nur, The effect of a percolation threshold in the Kozeny-Carman relation, *Geophysics*, **62**, 1480–1482, 1997.

O'Connor, R.M. and J.T. Fredrich, Microscale flow modeling in geologic materials, *Phys.*

Chem. Earth (A), **24**, 7, 611-616, 1999.
Rothman, D.H. and S. Zaleski, Lattice-gas cellular automata; simple models of complex hydrodynamics, *Monographs and Tests in Statistical Physics*, **5**, 297, 1997.Schumacher, E. F., *Small is beautiful; economics as if people mattered*, Harper & Row, New York, 1973.
Strebelle, S., Conditional simulation of complex geological structures using multiple-point statistics, *Mathematical Geology*, **34**, 1, 1-21, 2002.
Strebelle, S., and A. Journel, Reservoir Modeling Using Multiple-Point Statistics, *SPE Annual Technical Conference and Exhibition*, SPE71324, 2001.
Succi, S., A. Cancelliere, C. Chang, E. Foti, M. Gramignani, and D. Rothman, A direct computation of the permeability of three-dimensional porous media, C*omputational methods in subsurface hydrology*, Comput. Mech. Publ., Southampton, United Kingdom, 129-136, 1990.
Timur, A., An investigation of permeability, porosity, and residual water saturation relationships for sandstone reservoirs, *The Log Analyst*, **9**, 4, 8-17, 1968.
Tixier, M.P., Evaluation of permeability from electric-log resistivity gradients, *Oil and Gas J*., June 16, 1949.
Wyllie, M.R.J., and W.D. Rose, Some theoretical considerations related to the quantitative evaluation of the physical characteristics of reservoir rock from electrical log data, *J. Pet. Tech*., **4**, 189, 1950.
Yeong, C.L.Y., and S. Torquato, Reconstructing random media. II. Three-dimensional media from two-dimensional cuts, *Physical Review E,* **58**, 224-233, 1998.

Chapter 4
Sandstone Diagenesis

4.1 Abstract

The goal of this study is to better understand the effect of diagenesis and texture on fluid transport properties of sandstone. The approach consists of numerical experimentation of fluid flow in a realistic pore space at the grain scale. The pore space is obtained via images of sandstone captured in thin section or X-ray microtomography. Such virtual or digital sandstone can then be altered in the computer to simulate diagenesis. This chapter presents various diagenetic processes of sandstone that will later be used to model diagenesis of the digital rocks in Chapter 5.

4.2 Diagenesis of Sandstone

4.2.1 Diagenesis Overview

Diagenesis refers to processes that alter sediments or sedimentary rock subsequent to deposition. The diagenetic processes are physical, chemical and biological in nature. The sediment provenance as well as transport mechanisms (air, water, and gravity forces) determine the initial texture, including grain size, sorting and grain shape. The post-depositional alteration and diagenesis change the texture by compaction, cementation, replacement, recrystallization, and dissolution. Pore structure in sandstone and other clastic sediments, and, consequently, porosity and permeability, are altered by diagenesis (e.g., Beard and Weyl, 1973). All depositional and diagenetic factors affect the pore-space topology, and thus the porosity and permeability (Figures 1 and 2).

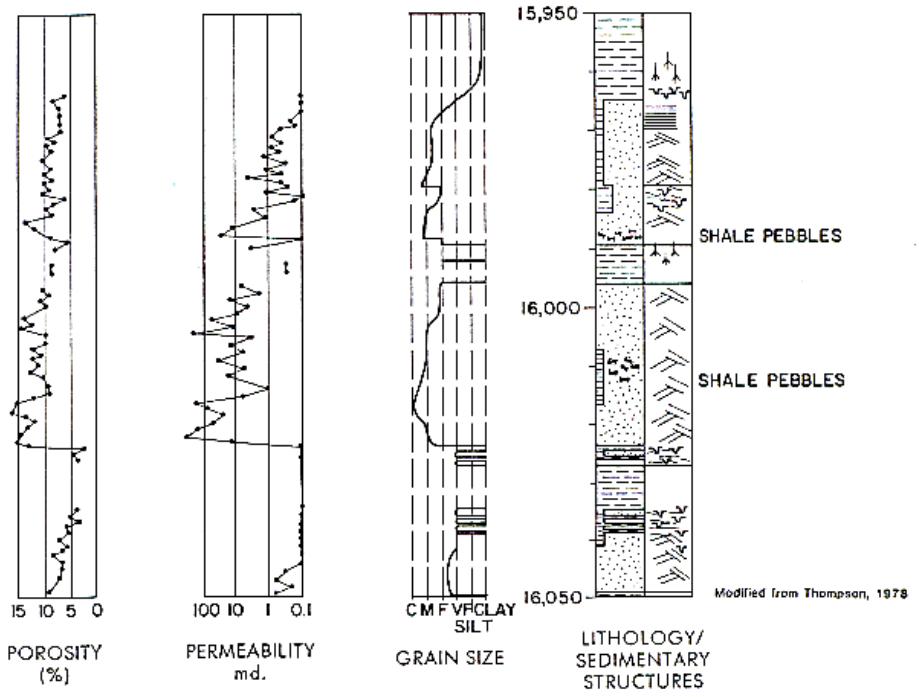

Figure 1. This log (Wilson and Stanton, 1994) shows vertical variations in porosity and permeability in deeply buried channel sandstone. Porosity and permeability closely correlate with the grain size and matrix content (lithology).

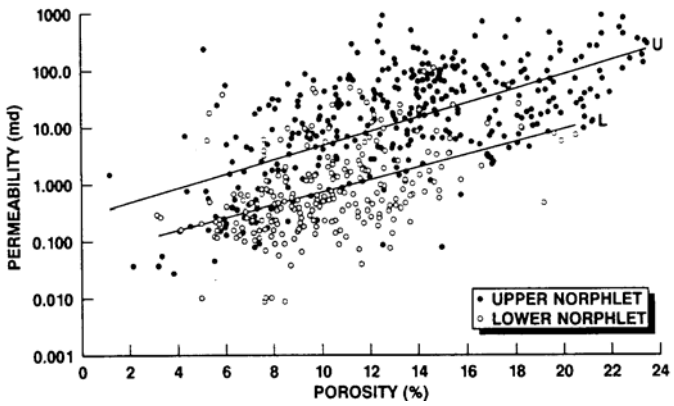

Figure 2. Porosity versus permeability in eolian sandstone of the Norphlet Formation, Mississippi (Studlick et al., 1990). Upper and lower Norphlet formations had different diagenetic paths, that affect the permeability values. The permeability of the lower Norphlet, where fibrous illite and halite cement are present, is an order of magnitude lower than that of the upper Norphlet. Illite and halite practically do not affect porosity but act to greatly reduce permeability. On the other hand, upper Norphlet experienced dissolution of evaporitic cements (such as anhydrite, carbonate, and halite) after the initial cementation.

Diagenesis includes both physical and chemical processes (Figure 3). Physical diagenesis includes both bioturbation and compaction. Some examples of chemical diagenesis are cementation, dissolution, replacement, recrystallization, and hydrocarbon generation (Boggs, 1992).

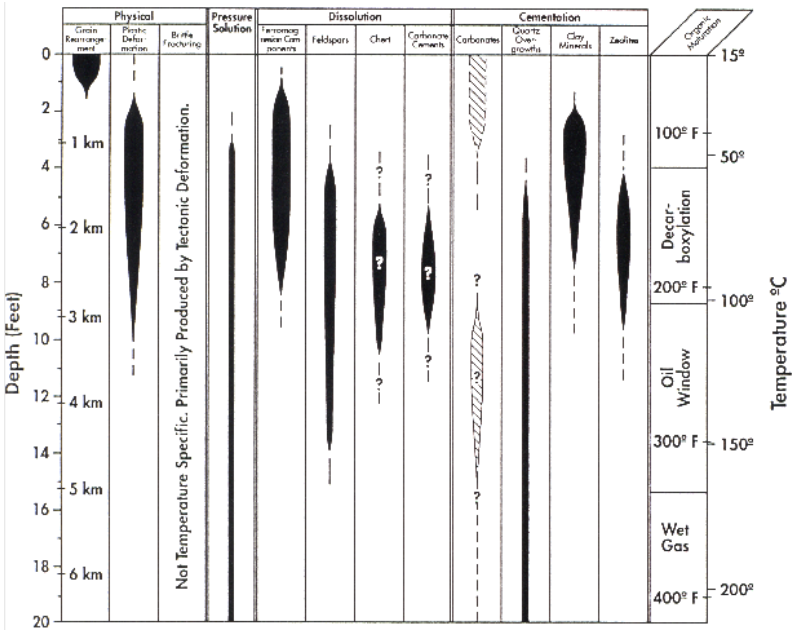

Figure 3. Generalized depth and temperature regimes for the major diagenetic processes from Wilson and Stanton (1994). The widths of the bars indicate the relative rates at which the processes operate.

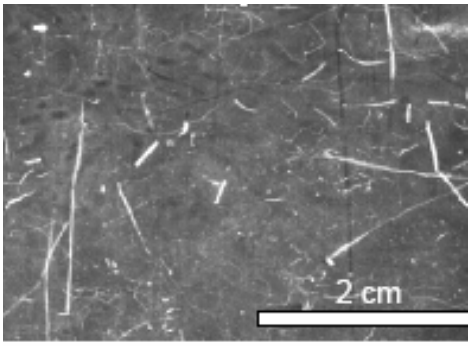

Figure 4. Microburrows of sediments in the southern Portuguese continental slope (Lowemark, 2003).

Bioturbation (Figure 4) reworks the deposited sediments through various crawling, burrowing and sediment-ingesting of organisms, thus destroying primary depositional features. However, subsequent changes in porosity due to compaction overshadow the effects of bioturbation.

Compaction is the reduction of sediment volume and decrease in porosity resulting from sediment loading and tectonic forces. Overburden weight results mainly from the sediment rock mass. At a 10 km depth the rock pressure is roughly 2.5 kb (Boggs, 1992). Temperature also influences compaction by promoting pressure solution. Physical diagenesis, therefore, is intimately related to chemical diagenesis (Figure 5).

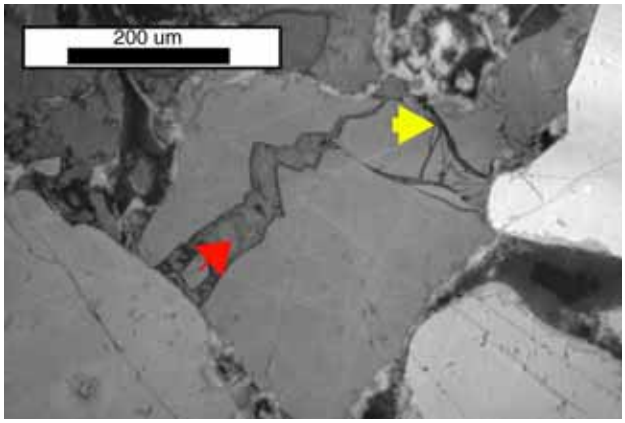

Figure 5. Scanning Electron Image showing the effect of compaction of a sandstone from Frio Formation, Gulf of Mexico (Makowitz and Milliken, 2002). The yellow arrow shows a partially filled fracture. The red arrow shows a quartz-filled fracture. Compaction is intimately related to chemical diagenesis.

Chemical diagenesis is a process caused by chemical reactions in rock due to change in pressure and temperature. As most sediments are either deposited subaqueously or buried below the water table, they become saturated with water. During burial, minerals are in constant contact with water that may contain various levels of salinity and various redox conditions, oxic to anoxic. The pore waters may also contain dissolved organic carbon. Sandstone commonly contain less than about 0.5 percent organic carbon (Boggs, 1992). Organic contents are reactive and can generate reaction products such as hydrogen and bicarbonate ions that change initial pore-water conditions and make other mineral components unstable. During early burial, these chemical reactions can lead to the precipitation of pyrite, chlorite, illite/smectite, quartz and feldspar overgrowth, and the precipitation of carbonate cements (Burley et al., 1985).

4.2.2 Cementation

Cementation plays a major role in reducing porosity and can inhibit compaction if cementation occurs at an early stage of diagenesis. Minerals that are most common in sandstone include carbonate, silica, and clay minerals. Carbonate cements, commonly calcite or dolomites, may fill pore spaces with a mosaic of fine crystals or with a single large crystal (Figure 6). Silica cements most commonly occur as overgrowths on quartz grains (Figure 7, 10). Quartz is the most important porosity destroying cement in sandstone reservoirs (Giles et al., 2000). Most sandstone, by definition, contain little detrital clay, but alteration of feldspars and ferromagnesian minerals can form authigenic clay (Figure 8, 9, 10). Also, pore waters from shale sequences can migrate into sandstone and may lead to clay precipitation there. There are cements that grow around the grains (rim cements) as well as cements that fill the pore space (occluding cements) (Figure 11). Such different growth-patterns can greatly affect permeability.

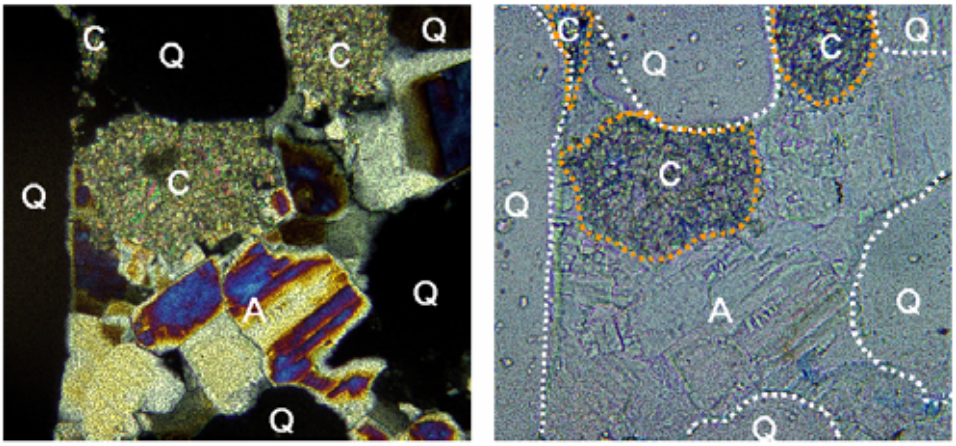

Figure 6. Photographs illustrating carbonate cementation from Eolian sandstone in the Minnelusa core used in Chapter 7. The pore space between quartz grains (Q) is filled with anhydrite (A) as well as dolomite (C). The dolomite may have been detrital in origin, then later deformed to become cement, or precipitated as cement *in situ*, or occur as a replacement to another unstable mineral. Photograph taken by Ayako Kameda.

Figure 7. A thin section of Fontainebleau sandstone showing quartz overgrowths shown as angular black shape around the grains, from Bryant et al. (1993).

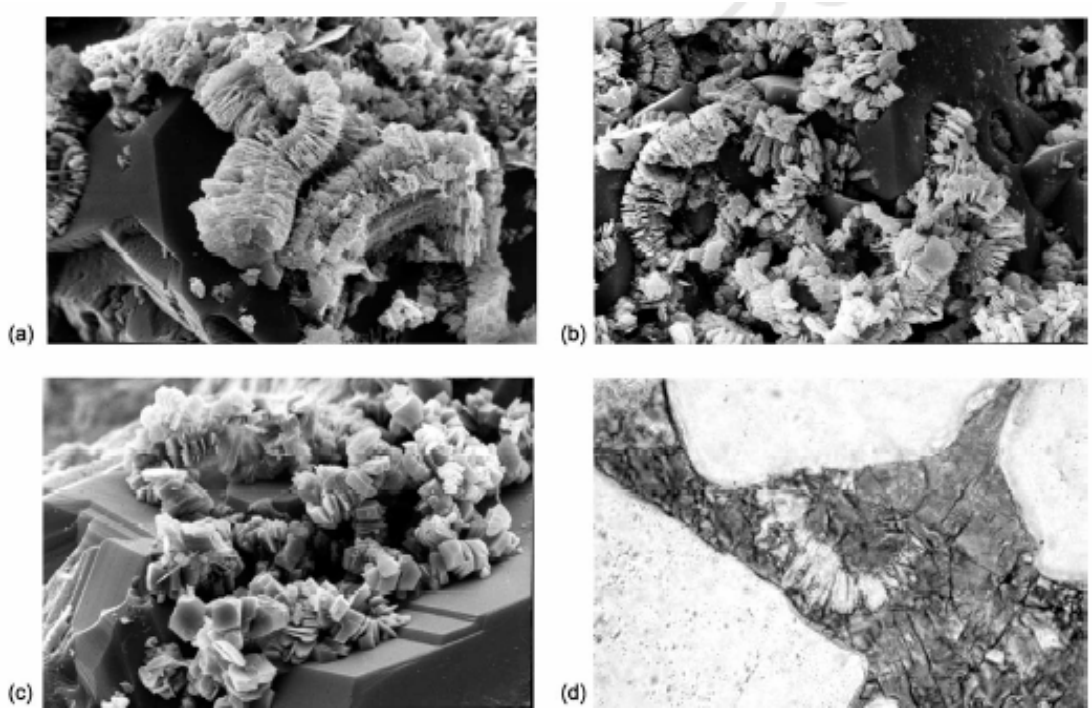

Figure 8. SEM images showing evolution of kaolinite cement morphologies (Wilkinson, 2003). (a) Early vermiform crystals which progressively dissolve, (b) while the blocky crystals grow within the verms, a pasta like wormy structure, until (c) only blocky crystals remain, (d) the vermiform kaolin is early in the paragenetic sequence as it occurs as a minor phase enclosed within some early calcite concretions. There is no visible porosity in this photomicrograph, the spaces between three quartz grains is entirely filled with an early ferroan dolomite cement which has been stained dark blue (shows as gray in the photo) for identification purposes.

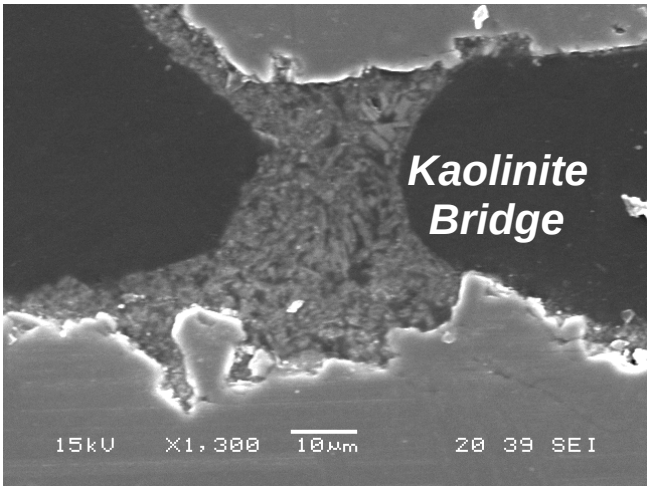

Figure 9. An example of diagenetic patterns in sandstone showing kaolinite clay bridging two sand grains. Photo courtesy M. Prasad. Kaolinite forms as blocky crystal form and as it grows it grows into the intergranular pore space. The image is ultrasonic microscopy.

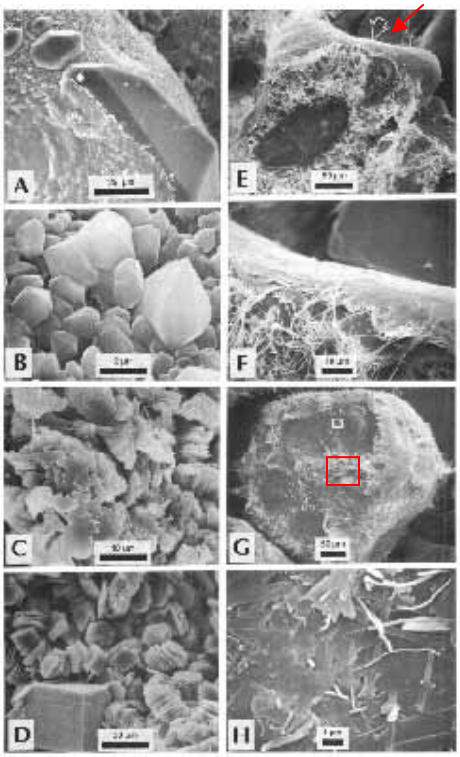

Figure 10. SEM photos of various cementing materials of sandstone from Wilson and Stanton (1994). A--isolated quartz overgrowth; B--small randomly oriented quartz overgrowth occurring over chert grain; C--authigenic kaolinite with ragged outlines plugs intergranular pores in a sandstone; D--books of dickite; E--grain-concentric illitic coats over the grain; F--high magnification of the view E indicated by a red arrow; note the illite is fibrous; G--grain shown is coated by a concentric coat of illite with only minor fibrous illite; and H--magnified view G indicated in red square, highlighting the bald grain contact area covered by illite ribbons.

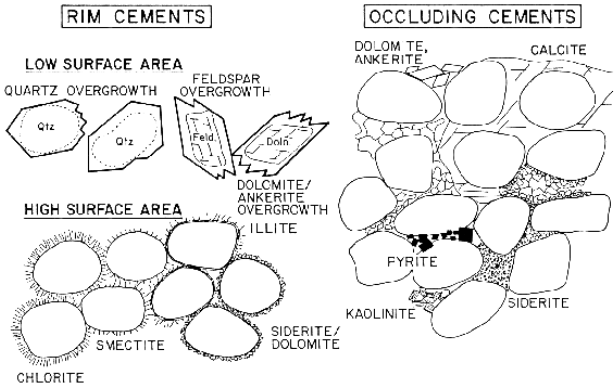

Figure 11. Major categories of cements, rim and occluding cements, from Wilson and Stanton (1994). While rim cements grow around the grains, the occluding cements fill the pore space.

4.2.3. Dissolution, Replacement and Recrystallization

Dissolution is responsible for most of the secondary porosity in sandstone. It includes dissolution of silica from quartz by circulating pore fluids as well as pressure solution of quartz at the points of contact. Dissolution of carbonate grains and cements in sandstone can also produce large secondary porosity in sandstone. Replacement involves dissolution of one mineral and precipitation of another in its place. Examples most commonly observed in sandstone are replacement of silicate minerals by calcite or dolomite, replacement of feldspars by clay and albitization of feldspars as shown in Figure 12 (Boggs, 1992). There is no net change in volume of the mineral during replacement. However, recrystallization is a process that involves changes in the size and/or shape of crystals of a given mineral such as transformation of SiO_2 polymorphs from opal-A to opal-CT to quartz (chert) as shown in Figure 13 (Boggs, 1992).

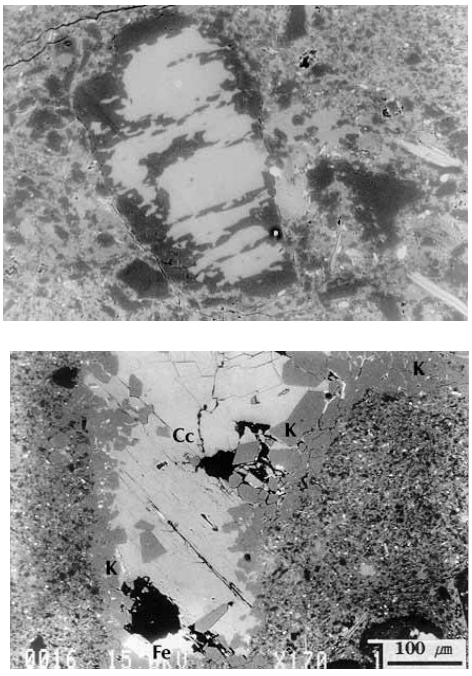

Figure 12. Back-scattered scanned electron images of mudrocks in Cretaceous Jeomgog Fm. by Lee, 2004, http://plaza.snu.ac.kr/~lee2602/atlas/bscatter.html. Top: Albite (dark gray) and calcite (light gray) replacement of K-feldspar (medium gray). Bellow: Euhedral K-feldspar (K) and calcite (Cc) filling in fracture of mudrock.

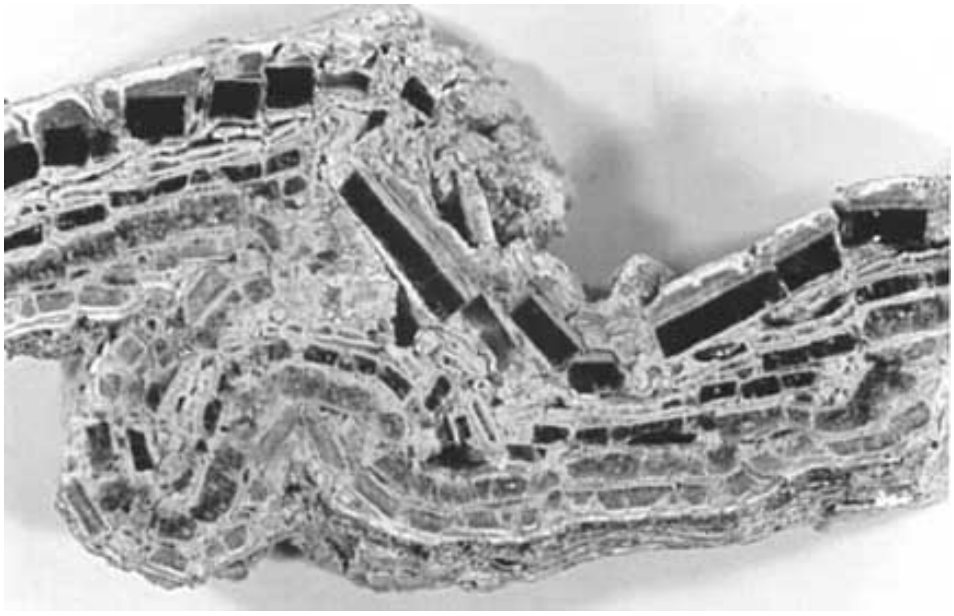

Figure 13. Photograph of a chert folded by brecciation into many fragments from the Miocene Monterey Formation (Eichhubl, P. and Behl, 1998). Transformation from opal-CT (light gray/white) to quartz (black) occurred in isolated fragments, from the center outwards; at this point the quartz chert fragments still retain a thin rim of light gray opal-CT. The size of the image is 7 cm.

4.3 Summary

Diagenesis encompasses all of the processes that act to modify sediments after deposition. The timing of porosity loss and enhancement due to diagenesis is of great interest to the petroleum industry. Numerical simulation of diagenesis can allow researchers to experiment with forward modeling for a specific rock type in a specific condition. This chapter compiles the up-to-date knowledge that will be used in the next chapter to formalize methods for numerically altering the digital pore space geometry to investigate the effect of diagenesis on rock permeability.

4.4 References

Beard, D.C., and P.K. Weyl, Influence of texture on porosity and permeability of Unconsolidated Sand, *AAPG Bull.*, **57,** 349-369, 1973.

Boggs, S., Jr., *Petrology of sedimentary rocks*, Macmillan Publishing Company, New York, 1992.

Bryant, S., Cade, C., and D. Mellor, Permeability prediction from geologic models, *AAPG Bull.*, **77,** 8, 1338-1350, 1993.

Burley, S.D., J.D. Kantorowicz, and B. Waugh, Clastic diagenesis, in Brenchley, P.J. and B.P.J. Williams, eds., in *Sedimentology, recent developments and applied aspects*, Blackwell, Oxford, 189-226, 1985.

Eichhubl, P., and R.J. Behl, Field guide to Diagenesis, deformation, and fluid flow in the Miocene Monterey Formation: Ventura-Santa Barbara-Jalama Beach-Grefco Quarry/Lompoc, *SEPM Pacific Section Special Publication*, **83**, 85-98, 1998.

Giles, M.R., *Diagenesis: a quantitative perspective implications for basin modelling and rock property prediction*, Kluwer Academic Publishers, Netherlands, 1997.

Lowemark, L., Automatic image analysis of X-ray radiographs: a new method for ichnofabric evaluation, *Deep-Sea Research I*, **50**, 815–827, 2003.

Makowitz, A. and K.L. Milliken, Quantitative measurements of brittle deformation with burial compaction, Frio Formation, Gulf of Mexico Basin. *GCAGS Transactions*, **52**, (in press) 2002.

Studlick, J.R.J., R.D. Shew, G.L. Basye, and J.R. Ray, A giant carbon dioxide accumulation in the Norphlet Formation, Pisgah Anticline, Mississippi, *Sandstone Petroleum Reservoirs*, Springer-Verlag, New York, 181-203, 1990.

Wilkinson, M., R. S. Haszeldinea, R.M. Ellamb, and T.E. Fallickb, Hydrocarbon filling history from diagenetic evidence, *Marine and Petroleum Geology*, in press, accepted 2003.

Wilson, M.D., and P.T. Stanton, Diagenetic mechanisms of porosity and permeability reduction and enhancement, *SEPM short course* **30**, 59-118, 1994.

Chapter 5
Numerical Diagenesis of Virtual Rocks

5.1 Abstract

The previous chapter introduced diagenesis, which commonly occurs in sandstone. This chapter focuses on several of these processes and demonstrates how digital rocks can be numerically altered to simulate the alteration of the pore space due to diagenesis. Specifically, quartz overgrowth and patchy pore filling cementation are modeled, to be applied later to the Wyoming core. Other numerical alteration schemes, such as random pore-filling and bridging of grains, are also introduced as ways of simulating deposition and diagenesis.

Ideally, in all numerical diagenesis simulations, one can write codes that will alter a 3D volume directly. However, it is very complicated to program such alterations in a

realistic 3D pore space. Moreover, one may not have access to high-quality 3D images of rocks, and the only choices maybe 2D thin sections.

In light of these limitations, this chapter also explores the "problem avoidance" technique of altering 2D images of digital rocks instead of 3D images. For example, a geologist alters a 2D image simply by hand-drawing or by using a relatively simple Matlab routine. Then, using a geostatistical sequential-indicator simulation, 3D realizations are produced from these altered 2D images. Will such alteration of 2D images, and the subsequent 3D pore-space realizations, result in the same calculated permeability as the 3D volumes that underwent direct numerical alterations?

To address this question, three numerical alteration schemes are chosen: shaly sand simulation (insertion of sub-resolution particles), quartz overgrowth (uniform expansion of grains), and patchy cementation (insertion of large patches of cement). The results show that for these three cases, the numerical alteration of a 2D image produces essentially the same porosity-permeability trend as the direct numerical alteration of 3D volumes. Therefore, for the cases examined, diagenetic alteration of virtual rock for the purpose of permeability modeling can be conducted on 2D images.

5.2 Modeling Diagenesis: Previous Work

This study employs numerical alteration of digital pore space as an approach to model diagenesis and its effect on fluid flow. Ideally, the physical, chemical and biological nature of diagenesis can be fully quantified and modeled on the computer. Many workers have integrated various aspects of diagenesis into reservoir simulation and geochemical modeling. In this thesis I focus on how to extract fluid flow properties of sandstone from digital rock structures at the pore scale and link these properties to diagenetic alteration of the digital pore space.

There are four different approaches in modeling diagenesis, (1) an empirical approach based on depth trends observed in sediments (e.g., Falvey and Deighton, 1982; Baldwin and Butler, 1985; Byrnes, 1994; Giles, 1997), (2) geochemical modeling (e.g., Boles, 1979; Boles, 1991; Wood, 1994), (3) quantitative and mathematical modeling based on measurable or quantifiable parameters such as grain size, composition, cementation, chemical reaction rates, and thermal and burial history (e.g., Beard and Weyl, 1973;

Berner, 1980; Estes et al., 1994; Bloch, 1994; Boudreau, 1997; Bray et al., 2000), and (4) numerical alteration of digital pore space (e.g., Bryant et al., 1993; Bosl et al., 1998; Keehm et al., 2001).

This thesis builds on approach #4, and expands the work started by the previous researchers in the numerical diagenesis field. Altering a digital rock structure (diagenesis) and computing permeability on the altered structure can give us a direct cause-and-effect connection from diagenesis to permeability. In the end, quantitative modeling of 3D pore geometry and accurate simulation of fluid flow through the pore space can become powerful tools to understand the interaction between diagenesis and fluid flow.

Cementation is a process that converts loose grains into solid rock by filling pore space with authigenic material, commonly calcite, quartz, and clay minerals. Contacts between grains are favorable for nucleation and are often where cementation initiates (Berner, 1980). However, as the sediments are buried, grain contacts become unfavorable for cementation due to increased insolubility caused by excess pressure.

Here, diagenetic changes will be numerically superimposed upon the digital pore space by, e.g., growing cement on the grain surface, filling corners between adjacent grains with clay, and bridging adjacent grains with clay. Digital pore space used can be obtained via thin-section images (2D) or X-ray microtomography of sandstone (3D). Depositional texture will be partly represented by grain-size distributions used in the original digital pore space. Additional depositional variability will be achieved by the numerical placement of silt/clay particles in the prototype pore space and on the digital grain surfaces. Permeability will be treated as a process-dependent parameter that evolves together with the pore-space evolution.

Here, the numerical modeling is in fact a geometrical alteration and does not involve geochemical modeling. It is not intended to disregard the large body of work that models geochemistry. In fact, geochemistry can be incorporated into the digital rock physics platform as input to numerical alteration of the pore space. However, for the purpose of this thesis, the diagenesis modeling approach will be mostly based on the simplified observable geometrical or physical description of diagenesis.

5.3 3D Numerical Alteration

5.3.1 Compaction

Three different types of numerical alteration of digital pore space have been used by researchers such as Bryant et al. (1993), Bosl et al. (1998), and Keehm et al. (2001): compaction, random pore-filling cementation, and uniform expansion. In this section, I will introduce the compaction method, and in the following sections I will discuss random pore-filling and uniform expansion schemes.

Bryant et al. (1993) modeled compaction by assuming that the center of a sphere with original coordinates *x*, *y*, and *z* will move to *x*, *y*, and *z*′ if

$$z' = z_0 + \lambda(z - z_0)$$

where z_0 is an arbitrary reference value and λ measures the degree of compaction. (Authors used $0.7 < \lambda < 1.0$.) This is equivalent to packing spheres in a vertical tube and compressing them vertically while the spheres are confined horizontally (Figure 1). The spheres are allowed to interpenetrate at the grain boundaries. The volume of interpenetration corresponds to the mass released by pressure solution (Bryant et al., 1993). This method, by no means, represents an actual compaction process, but it numerically simulates the geometrical alteration due to compaction in a very simplified manner.

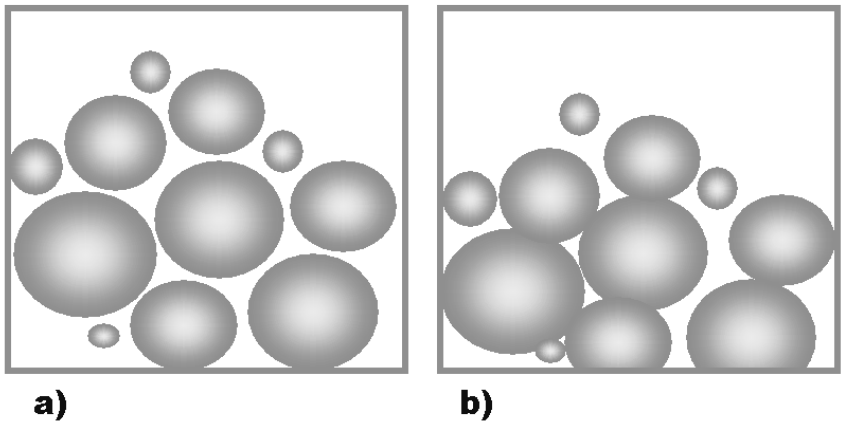

Figure 1. Cartoon representation of the compaction scheme on a Finney pack by Bryant et al. (1993). They shift the sphere centers vertically by the compaction amount, e.g., 30 %, and let the spheres interpenetrate at grain contacts. This is analogous to packing spheres in a rigid container that prevents horizontal movements. The volume lost by grain penetration can be a direct analog of the mass released by pressure solution.

5.3.2 Random Pore Filling and Bridging

The random pore-filling cementation scheme used in previous workers' research is much like turning 'clean' sand to 'dirty' sand, populating the pore space with much smaller particles representing silt or clay.

In the following chapter, a case study on a Wyoming eolian core will be used to illustrate an application of digital Rock Physics technology. In the Wyoming core, there is no evidence for authigenic clay, and very little detrital clay or mud is found in the dune deposits; therefore there is no need at this stage to develop such modeling techniques.

However, due to the limitation of X-ray microtomography technology, it is often difficult to visualize sub-resolution particles such as clay or silt; thus there may be a situation where one needs to numerically populate sandstone 3D images with small particles. Therefore, I will use this section to discuss (1) bridging and (2) random pore filling with small sub-resolution particles.

Unlike quartz overgrowth, authigenic clay cements can have inter-pore space-clogging geometry (kaolinite), book-like shapes (dickite) or concentric coating around the grain (illite). Such geometry can have a significant effect on fluid flow through the pore space. Similarly, whereas some cements such as quartz overgrowth grow around the rim, some cements fill the pore space, as in the case of kaolinite (Chapter 4, Figure 9).

This is accomplished by an image-processing tool within the Matlab platform. Here, I use a Finney pack as an original fabric on which to grow bridging cements. To do this, a slice of a 3D image is taken. Then by using commands in Matlab, bridging cements as seen in the kaolinite example above can be simulated (Figure 2). This operation requires a starting binary image and the command *bwmorph*. If the original binary image is called BW1, connecting formerly disconnected pixels can be done by typing *BW2=bwmorph(BW1, 'bridge', inf)* followed by *BW3=bwmorph(BW2, 'fill', inf),* where BW3 is shown in Figure 2 (right).

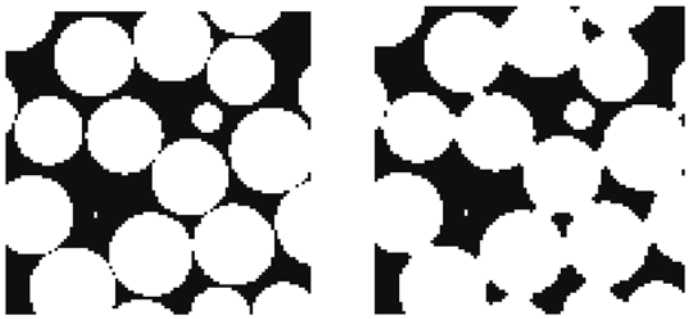

Figure 2. An original image of a Finney-pack thin section, BW1 (left), and the altered image after the bridge-and-fill operation in Matlab BW3 (right).

Detrital clay in the pore space of sandstone that is due to deposition, as opposed to diagenesis, will be modeled by randomly filling the pore space with small particles representing clay or shale (Figure 3). Specifically, random pixels are selected in the 3D space, and if the pixel is within the pore space represented as '0', it is converted to a solid, which is represented as '1' in a binary image. In the below figure, newly inserted solid pixels are represented as '2' so the new pixels (or clay) appear as yellow in the dark pore space (Figure 3).

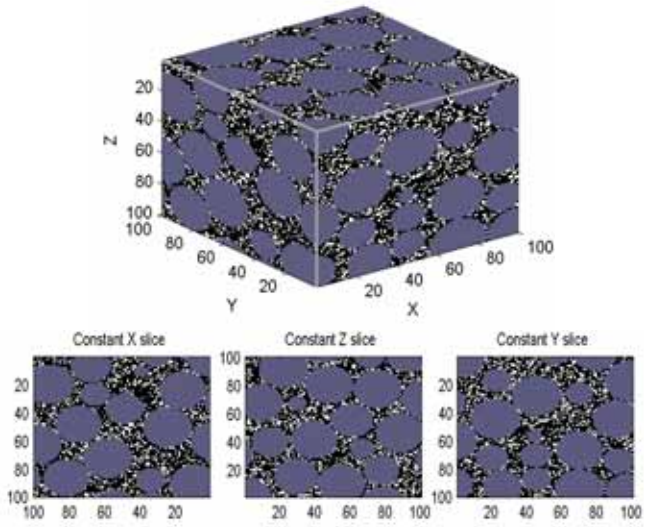

Figure 3. Finney pack volume filled with randomly inserted pixels (yellow) representing sub-resolution particles such as clay.

5.3.3 Quartz Overgrowth

Quartz is the most important porosity-destroying cement in many quartz sandstone reservoirs. The worldwide trends indicate that quartz cementation is controlled by fundamental processes that are common to all basins (Giles et al., 2000). Previous workers (Bryant et al., 1993; Bosl et al., 1998; Bray et al., 2000; and Keehm et al., 2001) used uniform expansion of grains to represent quartz overgrowth (Figure 4).

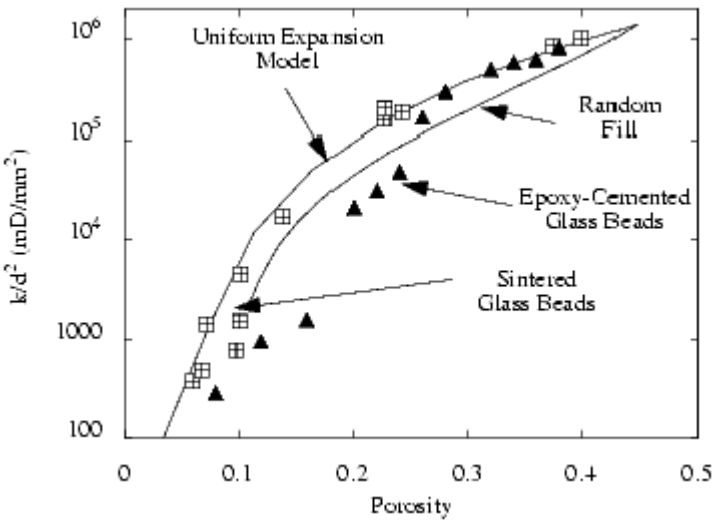

Figure 4. Computed porosity-permeability curves from cementation modeling and artificial sphere-pack data. Uniform expansion allowed cement to grow uniformly around grains that are spherical and equal in size originally. Random filling inserted cement randomly in the pore space. Figure from Bosl (1999).

In this study, quartz overgrowth will also be modeled as uniform expansion of non-spherical grains that are digital images of sandstone, such as the one shown in Chapter 4, Figure 7. This type of alteration of grain geometry can be achieved via Matlab. A binary image, *I*, can be dilated by typing *I2 = imdilate(I,SE)* in the Matlab command window, where *SE* is a command that determines the way image is dilated (i.e., shape and number of pixels added), and can be set by typing *SE = strel('square',3)*. The resulting dilation is as shown in Figure 5.

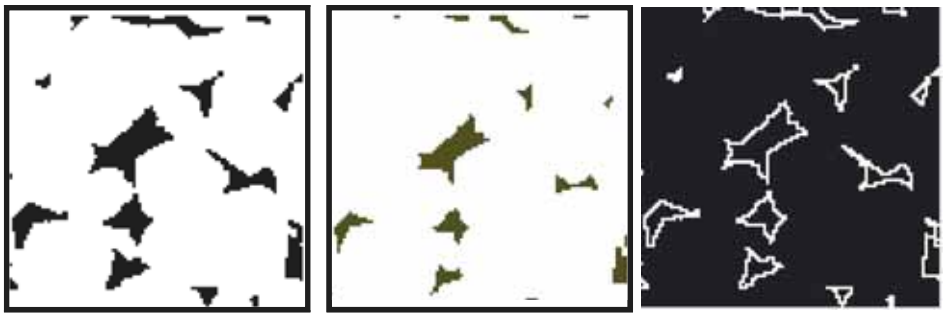

Figure 5. Fontainebleau sandstone thin section image (left), altered image after expansion of grains (center), and outline of expanded portions of the grain shown in white (right).

5.3.4 Patchy Cementation

In addition to compaction, random pore filling, and uniform expansion, I need to develop a numerical diagenetic scheme observed in the Wyoming core used in the later chapters. Anhydrite cements occur in patchy clusters in the eolian sandstone core. To model the patchy cementation, a simplified version of the cement patches will be represented as spherical clusters. The Matlab code allows the user to specify cement radius and the number of patches to be inserted. Random seeds are inserted into the sandstone fabric and spheres are grown around the seeds (Figure 6).

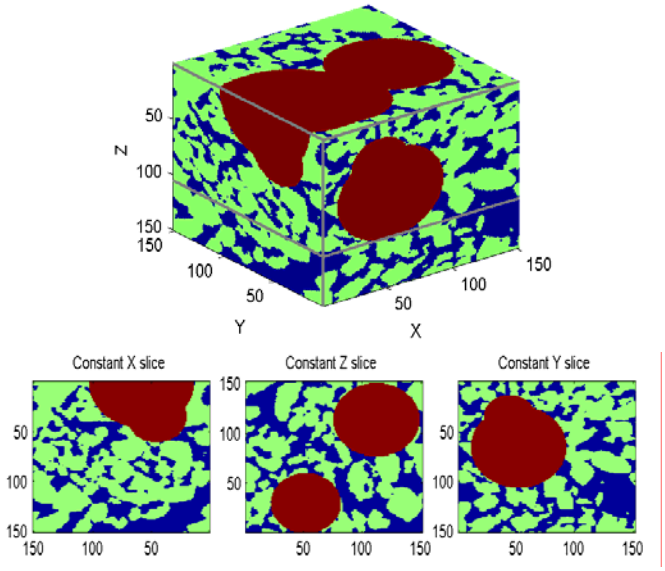

Figure 6. Eolian prototype sandstone (green) with three large cement patches (red) that blocks the pore space (blue).

5.4 Problem Avoidance by 2D Numerical Alteration

5.4.1 Workflow A: Compare Computed Permeability Values

In this section, I introduce a workflow to compare computed permeability values of digital rocks made from (1) 3D CT-scan images and (2) 3D geostatistical rock realization generated from 2D images (Figure 7).

Numerical alteration of digital pore space can be very complicated when programmed in 3D. Often packages such as Matlab come with simple 2D image analysis tools but are not equipped to handle 3D volumes without some modifications. Furthermore, 3D image scans of sandstone may not be available. Hence, thin sections, or 2D images, are usually more accessible and easier to deal with.

Can numerical alteration of digital rocks be done in 2D, instead of 3D? Can geostatistics then be used to produce 3D digital rocks that reflect the numerical alterations and still have the same calculated permeability as directly altered 3D images?

To answer these questions, I experiment using both 2D and 3D alteration techniques (uniform expansion, random pore filling, and patchy cementation) on Finney packs and on an eolian prototype, Año Nuevo, to see if the porosity-permeability trends are affected by different methodologies. The first method directly alters a 3D volume of digital rock. The second method alters one image slice of a rock, then simulates a 3D realization using a geostatistical indicator simulation. Then, the digital rocks generated by the 3D image (method 1) and the 2D image (method 2) are used to compute permeability via numerical fluid-flow simulation. The computed permeability values are then compared to one another.

Overall, the results show that both methodologies (3D and 2D alterations) produce very similar porosity and permeability (Figure 8, 9). However, the computed porosity and permeability are not a perfect match. This is due to the inherent difference between the pre-alteration porosity of the 3D image and the 2D image. A single 2D image does not represent the porosity of the overall 3D rock volume to begin with, so one must either choose a 2D image large enough to represent 3D pore-topology characteristics, or choose multiple 2D images to account for the natural variation of porosity among images.

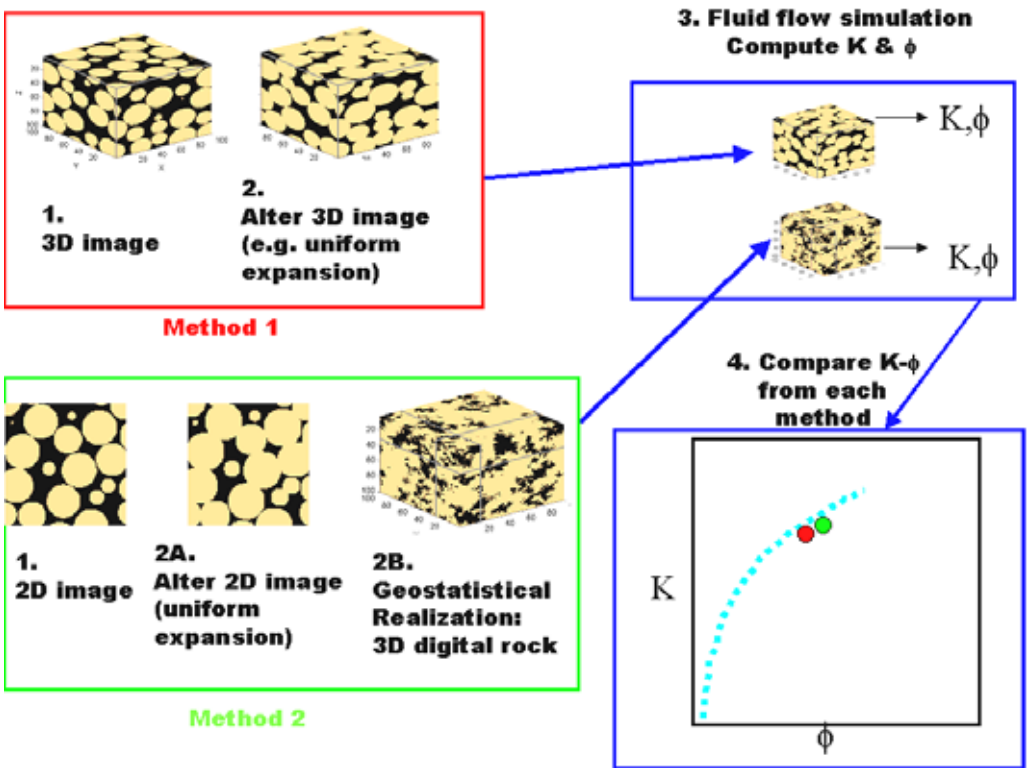

Figure 7. Workflow A, showing how to compare computed permeability of digital rock created by direct 3D scanning (method 1) and by geostatistics (method 2). In Workflow A, only ***one*** set of permeability and porosity values is computed per starting image.

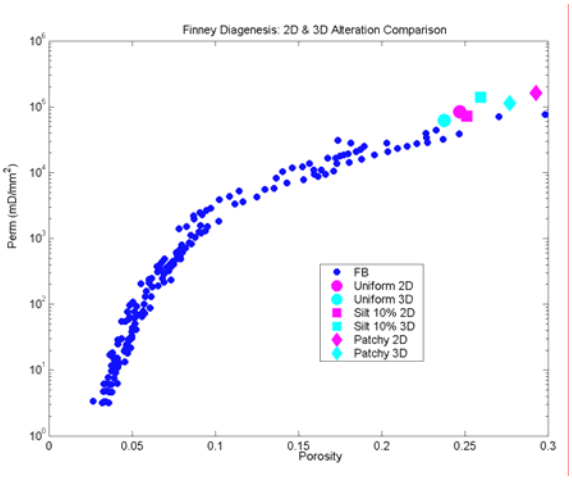

Figure 8. Workflow A results on a Finney pack, showing a porosity-permeability cross-plot. The blue trend is the Fontainebleau data set. Three schemes (uniform expansion, silt insertion, and patchy cements) are used to compare the computed permeability values between CT-scanned 3D rocks and geostatistically generated rocks from 2D images.

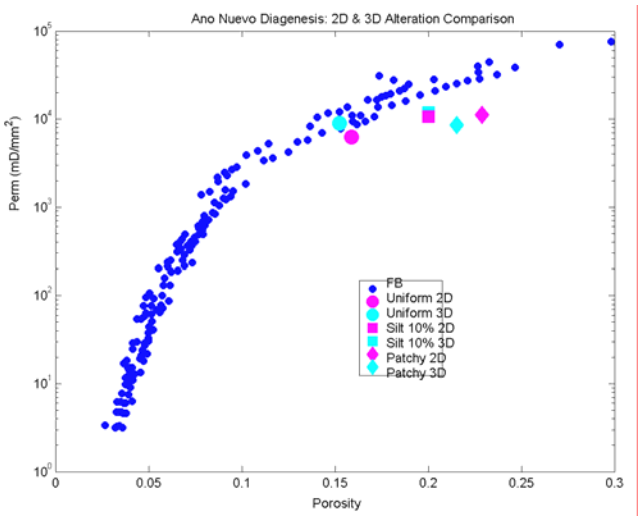

Figure 9. Workflow A results for the Año Nuevo eolian prototype pack, showing a porosity-permeability cross-plot. The blue trend is the Fontainebleau data set. Three schemes (uniform expansion, silt insertion, and patchy cements) are used to compare the computed permeability values between CT-scanned 3D rocks and geostatistically generated rocks from 2D images.

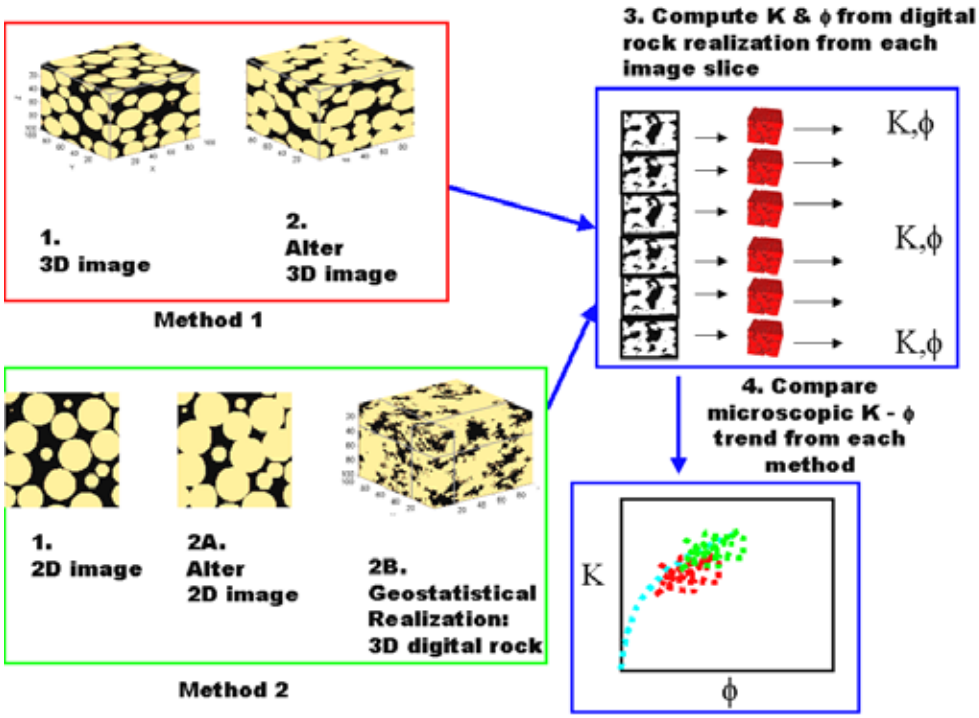

Figure 10. Workflow B, showing how to compare computed permeability-porosity trends of digital rocks created by direct 3D scanning (method 1) and by geostatistics (method 2). For each scheme of numerical alteration of the digital pore space (shown here is random insertion of cement), both altering a 3D volume and altering a 2D image are tried. After the pore space is altered, permeability and porosity trends are computed and cross-plotted for comparison. Unlike the workflow A, this workflow produces *multiple* porosity and permeability values per starting image. Each image (both 2D and 3D) produces a ***trend*** of permeability and porosity values.

5.4.2 Workflow B: Compare Porosity-Permeability Cross-Plot Trends

5.4.2.1 Workflow B: Introduction

Workflow A results show that the same experiments can be conducted in 2D instead of 3D, and they arrive at the same computed permeability (Figures 8 and 9). The next question is: can this random pore-filling experiment be conducted on a 2D image, instead of on a 3D volume, and still result in the same computed porosity-permeability trend?

In Workflow B, rather than comparing computed permeability of digital rocks produced by direct scanning (method 1) and geostatistics (method 2), I compare computed porosity-permeability trends (Figure 10). As in Workflow A, both a Finney pack and an eolian sandstone are altered via (1) random pore filling, (2) uniform expansion, and (3) patchy cementation. In the following sections, I go through the results for each of the alteration schemes in Workflow B.

5.4.2.2 General Results for Random Pore Filling Scheme

Random pore filling is a digital rock alteration scheme that can help simulate a random, pore-clogging cement (diagenesis), which is the same as filling a clean sand sample with silt or clay (depositional). Keehm (2003) has compared random pore filling to uniform expansion (referred to as a boundary cementation scheme), and found that random pore filling has a steeper permeability-porosity curve than does uniform expansion (Figure 11).

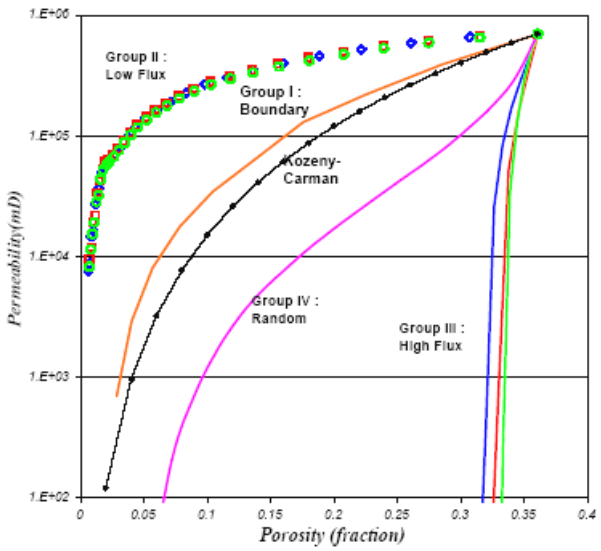

Figure 11. Permeability-porosity cross-plot by Keehm (2003) for various digital rock alteration schemes: boundary (uniform expansion), random, high flux and low flux cement precipitation.

Similarly, I conduct a random pore-filling experiment on a 3D digital pack of identical spheres. The results show that when inserting random particles into the pore space, the porosity and permeability curve is steeper than that of the Fontainebleau curve (same curve as the uniform expansion curve: see Chapter 3, Figure 10a), especially for results below 20-25 % porosity for this particular set of numerical experiments (Figure 12).

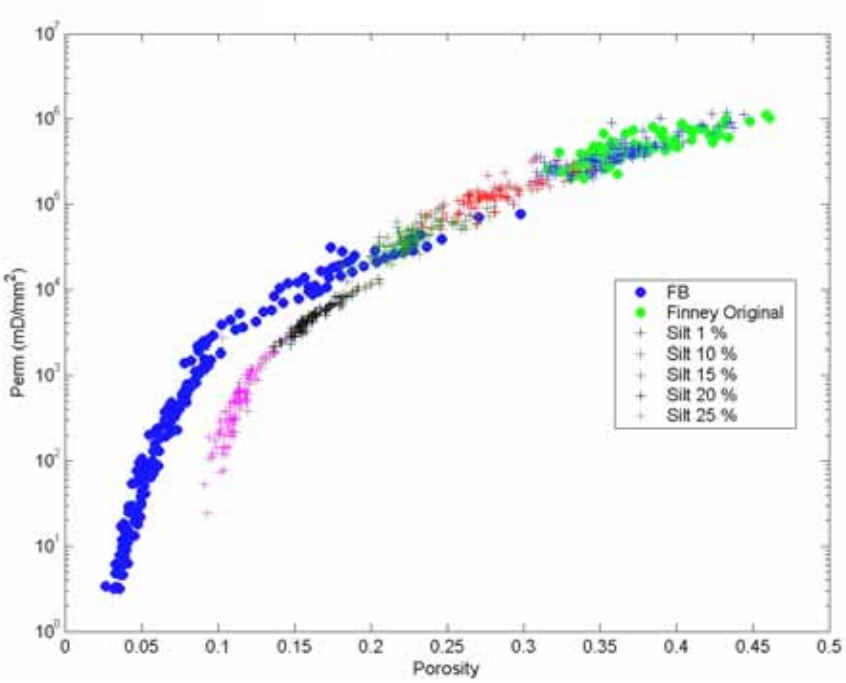

Figure 12. Permeability-porosity cross-plot comparing the Fontainebleau sandstone data set (FB) and random cement insertion (silt insertion) on a 3D Finney pack. The original Finney scatter is shown in green. The Fontainebleau data set, which forms a trend that overlaps the uniform expansion curve, is blue.

5.4.2.3 Comparing 2D & 3D Alteration for a Random Pore Filling Scheme

Using Workflow B introduced in Figure 10, a 2D image of a sphere pack and a 3D volume of sphere pack are altered to simulate random pore filling (Figure 13). In both cases, particles equivalent to 10% of the bulk volume are added to the pore space randomly. The results show an overlapping trend between Method 1 (add cement in 3D) and Method 2 (add cement in 2D, then make a 3D digital rock via geostatistics). This shows that when using micro-images and geostatistics as a way to compute massive

porosity and permeability, altering a 2D image produces the same porosity-permeability trend as direct alteration of a 3D volume.

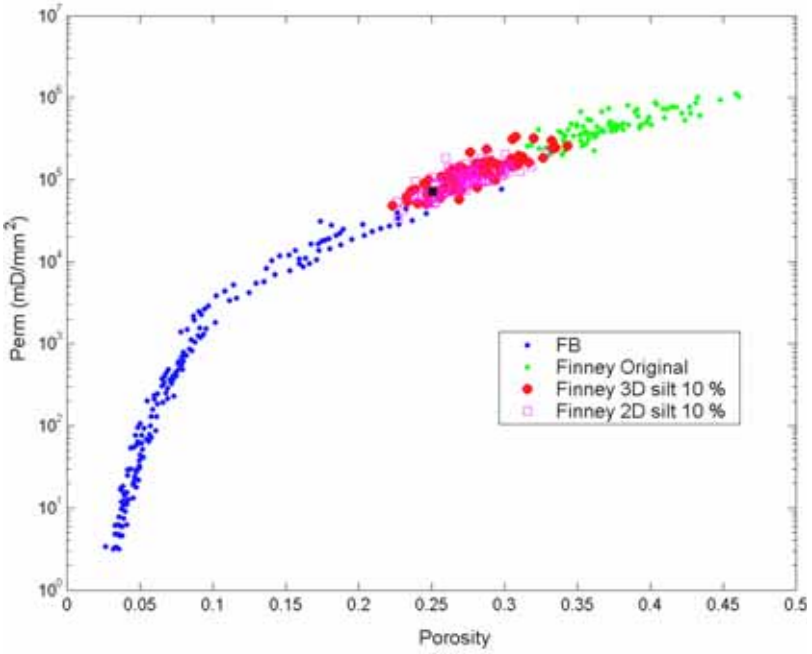

Figure 13. Permeability-porosity cross-plot comparing 2D and 3D random cement insertion (silt insertion) on a Finney pack. The original Finney scatter is shown in green. The Fontainebleau data set in blue. Method 1 (3D alteration) is shown as red circles, and Method 2 (2D alteration) is shown as pink squares. Both Method 1 and 2 have overlapping trends.

To further validate the conclusion that diagenetic or depositional alteration can be conducted on a 2D image and, as a result, valid porosity-permeability trends can be calculated, I expand the numerical experimentation to include a natural sandstone sample.

A CT-scan image of an eolian core from the Minnelusa Formation in Wyoming (Chapter 7) is used for this experiment. After adding random particles into the pore space, the two scatter trends formed by Method 1 (3D) and Method 2 (2D) are essentially the same (Figure 14). In addition, both methods predict a trend that is steeper than that of the Fontainebleau trend; with reduction in pore space due random pore filling, the permeability drop is more rapid than if the same sandstone was subjected to uniform expansion. Although the particular Wyoming eolian core contains very little clay in reality, if one wished to create a digital rock with similar fabric and more clay particles, one can use simple image analysis tools to do so on a 2D image and predict a porosity-

permeability trend. In Chapter 3, the results for porosity-permeability trends were limited to clean sands due to limitations in CT-scanning capabilities. This result, however, shows that a digital rock can be modified using simple tools to accommodate such limitations in imaging techniques.

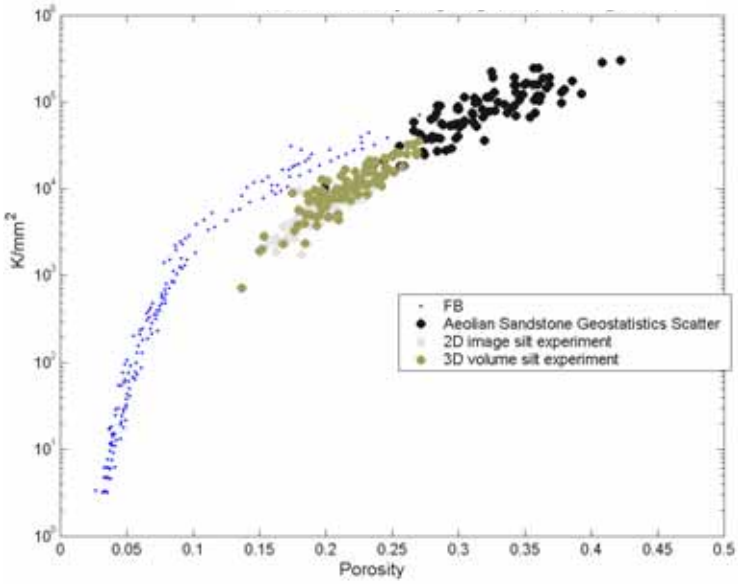

Figure 14. Permeability-porosity cross-plot comparing 2D and 3D random pore-filling schemes on eolian core CT scan from Wyoming. Original eolian core scatter is shown in black. The Fontainebleau data set is shown in blue. Method 1 (3D alteration) is shown as green circles, and Method 2 (2D alteration) is shown as gray circles. Both Method 1 and 2 have overlapping trends. Particles (referred for convenience as silt, although this has no mineralogical implications) added to the pore space are 10 % of the volume of the sample in both cases.

5.4.2.4 Comparing 2D & 3D Alteration for Uniform Expansion Scheme

The random pore-filling scheme, or a method to fill otherwise clean sandstone images with silt, is not strictly a diagenesis or pore-alteration scheme such as the one required to simulate diagenesis of eolian sandstone in a later chapter. However, quartz overgrowth, or uniform expansion of grains, is a very common form of diagenesis that occurs in sandstone and is observed in the thin sections of the eolian cores from the Minnelusa Formation in Wyoming. Here, I conduct uniform expansion directly on a 3D volume (Method 1) as well as on 2D images (Method 2) of the Finney pack and eolian core plug, and use workflow B shown in Figure 10 to produce porosity-permeability scatter. The results show that both 3D and 2D images produce essentially the same porosity-

permeability trend on a Finney pack and on eolian sandstone digital pore structures (Figure 15 and 16).

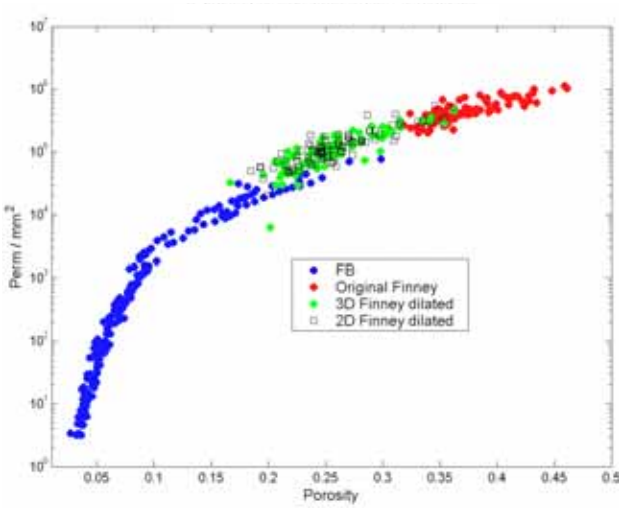

Figure 15. Permeability-porosity cross-plot comparing 2D and 3D uniform expansion on a Finney pack. Original Finney pack scatter is shown in red. Fontainebleau data set is shown in blue. Method 1 (3D alteration) is shown as green circles, and Method 2 (2D alteration) is shown as empty squares. Both the 2D and 3D alteration schemes have overlapping trends. The Matlab command for uniform expansion in a 2D image is "*imdilate*," where grains are dilated, or expanded, uniformly.

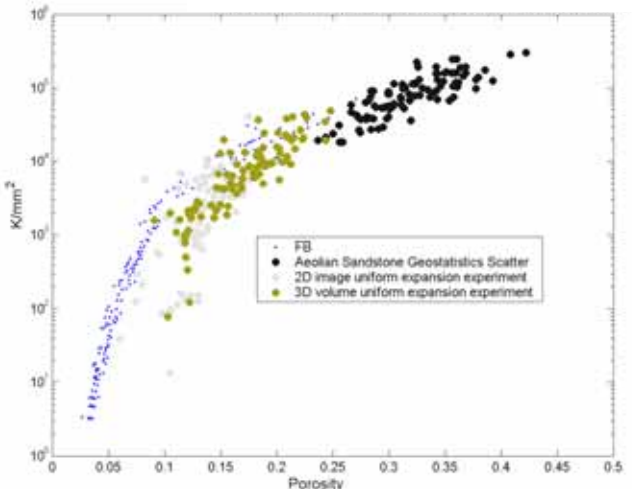

Figure 16. Permeability-porosity cross-plot comparing 2D and 3D uniform expansion on an eolian core plug from Wyoming. Original eolian scatter is shown in black. The Fontainebleau data set is shown in blue. Method 1 (3D alteration) is shown as green circles, and Method 2 (2D alteration) is shown as gray circles. Both Method 1 and 2 have overlapping trends.

5.4.2.5 Comparing 2D & 3D Alteration for Patchy Cementation

A similar numerical experiment is conducted for patchy cementation on a Finney pack. Figure 17a shows the 3D Finney pack altered with a patchy-cementation

algorithm. Figure 17b shows the 3D structure after altering a single 2D-thin section image of the Finney pack using a 2D patchy-cementation algorithm, and using indicator geostatistics to simulate a realization of a corresponding 3D pore space. Here, the patches are chosen to be equivalent to the grain size (2mm) in diameter, but the code allows for any choice of patch sizes. In the Wyoming sample, the patches often cover several grain sizes in the sandstone section.

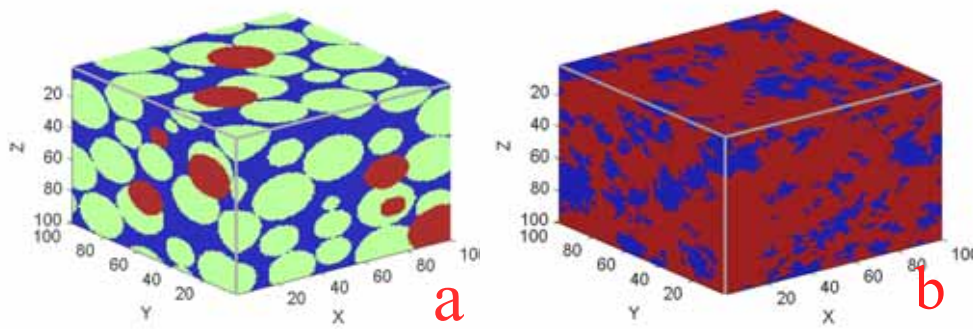

Figure 17. Digital structure of patchy cementation, Method 1 and Method 2, on a Finney pack. (a) Method 1, where patchy cementation is conducted on a 3D Finney pack. Blue is pore, green is grains, and red is the patchy cement; (b) Method 2, after patchy cementation is conducted on a 2D image of the Finney pack, then brought into 3D structure using indicator geostatistics. Blue is pore space, whereas red is the solid (original grain and the patchy cement). Note that the two-point statistics used in the indicator geostatistics code does not simulate patterns or shapes of grains. Also, indicator statistics recognizes 1 (solid) and 0 (pore), so the cement is considered the same as the grains (solid=1).

The geostatistical representation of rock structure with patchy cementation, in many ways, no longer looks spherical because the geostatistics code is limited to 2-point statistics. Despite such limitation in the algorithm, the porosity-permeability trends computed from Methods 1 ands 2 are essentially the same (Figure 18). This implies that if one has access to only 2D thin-section images of a core, it is possible to conduct patchy cement alteration on the 2D images, then use the workflow shown in Figure 10 to produce a porosity-permeability scatter.

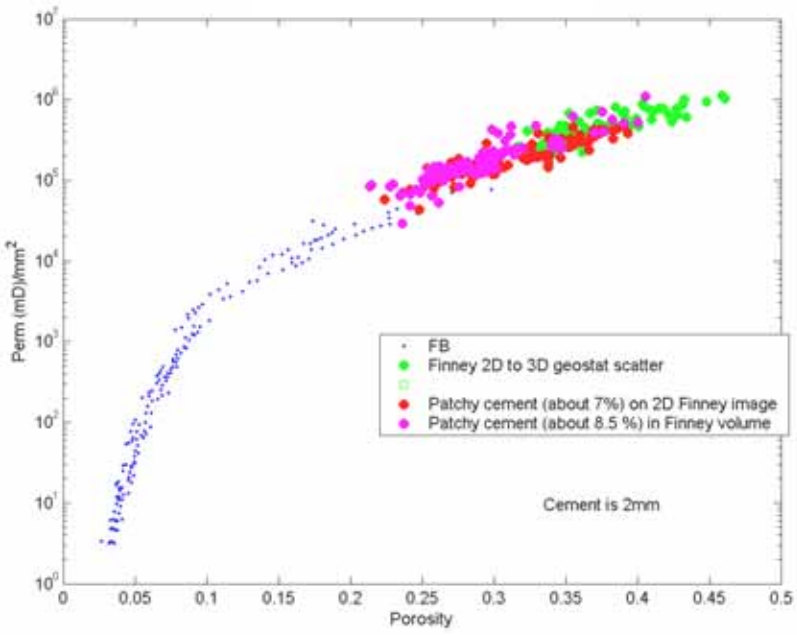

Figure 18. Permeability-porosity cross-plot comparing 2D and 3D patchy cementation on a Finney pack. The original Finney pack scatter is shown in green. The Fontainebleau data set is shown in blue. Method 1 (3D alteration) is shown as green circles, and Method 2 (2D alteration) is shown as empty squares.

5.5 Does 2D Alteration Work?

For the random pore-filling scheme, uniform expansion, and patchy cementation, 2D alteration produces computed permeability similar to the 3D results. However, the choice of the 2D image used for diagenetic alteration can be crucial in controlling the computed permeability. To circumvent this problem, one needs a large enough 2D image that will represent the porosity of the overall sample. However, such an image may not be available, and conducting numerical fluid-flow experiments on a 3D realization of such large image will be costly. Therefore, I also experimented with producing porosity-permeability trends from the altered digital pore structure. The results show that the 2D alteration produces computed porosity-permeability trends similar to those from 3D alteration.

However, this is confirmed only for the aforementioned schemes (random, uniform and patchy), and is valid for permeability, a fluid-flow property. If, for example, a researcher wishes to conduct an elastic experiment, resolving contacts between grains is extremely crucial, and thus this particular methodology of expanding a 2D image to a 3D digital pore space may not work as well. As shown in Figure 17, the digital structure that

results from Method 2 using geostatistics has very different grain contacts than the digital structure from Method 1. Therefore, one must use much caution and not assume that the "problem avoidance," or altering 2D instead of 3D, works universally in all cases, on all rocks, in all experiments.

However, it will save much time, cost, and effort if one has access only to thin section images or only to 2D image analysis tools and wishes to simulate fluid flow through these structures. In addition, a geologist may want to make an artistic judgement on the type of alteration scheme that can occur in a particular rock. Then it is possible to let the geologist "draw" the diagenetic modification of the pore structure on a 2D-thin section image, then use Method 2 to obtain a porosity-permeability trend. This discovery, that the 2D alteration can be used, albeit in a limited setting, can help us "avoid" the complicated problem of obtaining 3D scan images and writing complex 3D algorithms to simulate diagenesis.

5.6 References

Baldwin, B., and C.O. Butler, Compaction curves, Bull. *Am. Assoc. Petrol. Geol.*, **69**, 4, 622-626, 1985.

Beard, D.C., and P.K. Weyl, Influence of texture on porosity and permeability of unconsolidated sand, *AAPG Bull*., **57,** 349-369, 1973.

Berner, R.A., *Early diagenesis: a theoretical approach*, Princeton University Press, 1980.

Bloch, S., Effect of detrital mineral composition on reservoir quality, *SEPM short course* **30**, 161-182, 1994.

Boles, J.R., Active ankerite cementation in the subsurface Eocene of Southwest Texas, *Contributions to Mineralogy and Petrology*, **68**, 13-22,1979.

Boles, J.R., Plagioclase dissolution related to oil residence time, North Coles Levee Field, California, *AAPG Bull.*, **75**, 544, 1991.

Bosl, W.J., J. Dvorkin, and A. Nur, A study of porosity and permeability using a lattice Boltzmann simulation, *GRL*, **25**, 1475-1478, 1998.

Boudreau, B.P., *Diagenetic models and their implementation,* Springer-Verlag, Berlin, 1997.

Bourbie, T., and B. Zinszner, Hydraulic and acoustic properties as a function of porosity in Fontainebleau sandstone, *JGR*, **90**, 11524-11532, 1985.

Bray, A.A., R.H. Lander, C.A. Watkins, C.J. Lowrey, and M. Owen, Characterisation and prediction of clastic reservoir quality, an integrated model for use in exploration, appraisal and production projects, *AAPG Bull.*, **84**, 9, 1408, 2000.

Bryant, S., C. Cade, and D. Mellor, Permeability prediction from geologic models, *AAPG Bull*., **77,** 8, 1338-1350, 1993.

Byrnes, A.P., Empirical methods of reservoir quality prediction, *SEPM short course* **30**, 9-22, 1994.

Estes, C.A., G. Mavko, H. Yin, and T. Cadoret, Measurements of velocity, porosity, and permeability on unconsolidated granular materials, *Stanford Rock and Borehole Geophysics Project Annual Report*, **55B**, G1-1-G1-9, 1994.

Falvey, D.A., and I. Deighton, Recent advances in burial and thermal geohistory analysis, *Aus. Pet. Explor. Assoc. J*., **22**, 65-81, 1982.

Finney, J., Random packing and the structure of simple liquids i. the geometry of random close packing, *Proc. Roy. Soc.*, **319A**, 479, 1970.

Giles, M.R., *Diagenesis: A quantitative perspective implications for basin modelling and rock property prediction*, Kluwer Academic Publishers, Netherlands, 1997.

Keehm, Y., *Computational rock physics: Transport properties in porous media and applications*, Ph.D. Dissertation, Stanford University, 2003.

Keehm, Y., T. Mukerji, and A. Nur, Computational rock physics at the pore scale: Transport properties and diagenesis in realistic pore geometries, *The Leading Edge*, SEG, **20**, 180-183, 2001.

Wood, J.R., Geomechanical Models, *SEPM short course* **30**, 23-40, 1994.

Chapter 6
Case Study Part 1: Geological Evolution of Eolian Core from the Minnelusa Formation, Wyoming

6.1 Introduction

Previous chapters outlined basic methodologies of using digital rock images to compute permeability. In the next two chapters, these principles and basic methods are applied to a 60-ft eolian core from the Minnelusa Formation in the Powder River Basin, Wyoming. The goal of the project is to show how digital prototypes may be used to model diagenesis and the subsequent porosity-permeability evolution in geologic time and in geologic space.

The digital images used are CT-scanned images of sandstone plugs, as well as the eolian prototype produced from loose sands taken from a modern eolian depositional environment. Petrographical analysis helped determine the type of diagenesis that affected the sandstone. Then, using the numerical diagenesis tools introduced in the previous chapter, I simulate such diagenetic processes on the digital representations of the sandstone.

This chapter describes the geological background and the thin section analysis to determine depositional environment and diagenetic evolution of the samples. In the next chapter, the geological evolution described in this chapter is simulated on the computer using the digital rock approach.

6.2. Geological Background

6.2.1 Overview

The well log and core used in this study are from the Upper Minnelusa Formation of the Powder River Basin, Wyoming (Figure 1). The data were provided by Lake Ronel Oil Company from its #1 State 36-10 well in the Wildcat Field. The Upper Minnelusa was formed during early Permian time (Fryberger, 1984). The sands were sourced by northeasterly trade winds and were deposited in a land area close to the Lusk embayment, a restricted extension of the Permo-Pennsylvanian Sea (Kelly et al., 1985). These deposits are mixtures of marine and eolian sediments that occurred during transgressions and regressions (Fryberger, 1984). The samples used in this thesis are interpreted to be of eolian and marine dolomite deposits by the Lake Ronel Oil Company based on the seismic and well-log as well as observation of the core. During marine transgressions, the dune deposits were submerged and preserved by the continued subsidence of the shallow embayment.

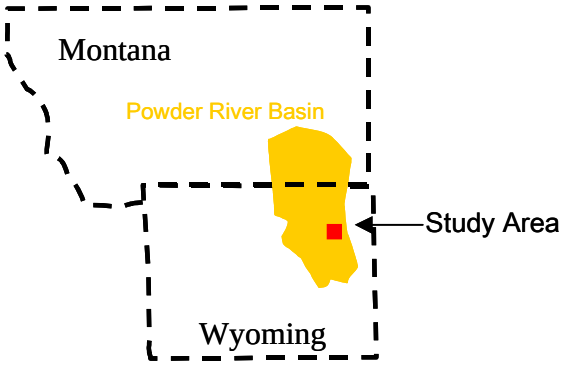

Figure 1. Location of the study area: Eastern Powder River Basin, in Wyoming.

6.2.2 Idealized Vertical Sequences

There are three major sequences within Lake Ronel's exploration area, named the A, B, and C sequences. The designation system employed here is the "Shell System," in which the sand immediately above the dolomite takes the letter of the dolomite, thus the B sand overlies the B dolomite. In terms of deposition, however, the dolomite is closely related to underlying sands, thus B dolomite is closely tied to the underlying C sand (Fryberger, 1984).

An idealized vertical sequence of lithologies is based on many cores from the

Minnelusa Formation (Figure 2). The specific core we use in this study misses some of these sequences.

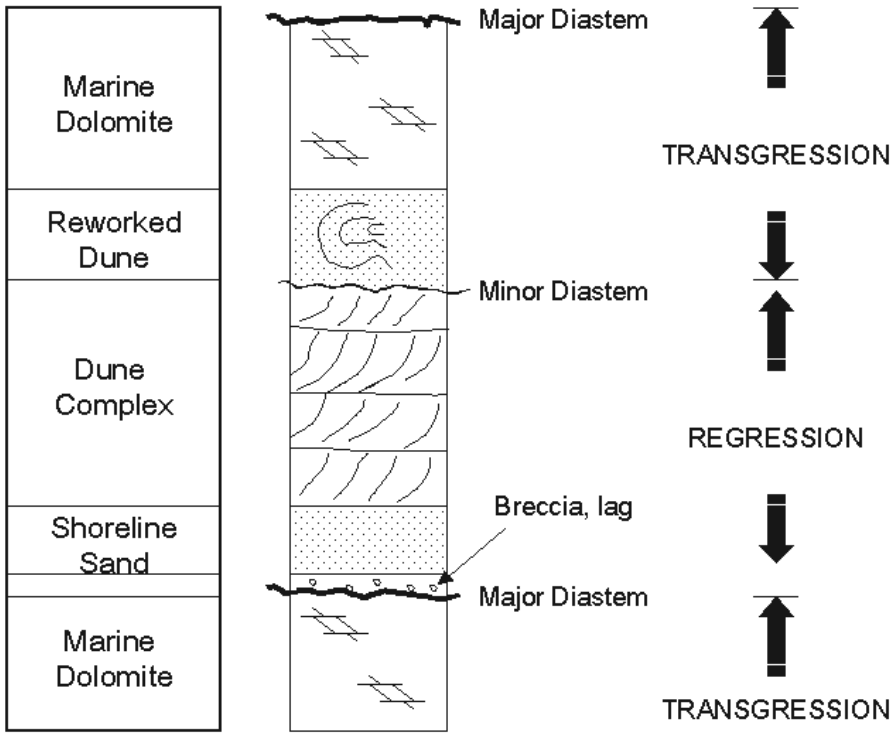

Figure 2. The idealized vertical sequence of Minnelusa lithologies, modified from Fryberger, 1984. This is a typical sequence found in many of the studies from the Minnelusa cores. In the core used in this study, mostly dune-interdune complex and the marine dolomite are present. Diastem is a depositional break that records little or no erosion before the deposition was resumed.

6.2.3 Core and Well Log

The 60-ft core consists of sequence B eolian sandstone which overlies the sequence B marine dolomite (Figure 3). The B dolomite of the Upper Minnelusa is an evaporitic unit containing two anhydrite units separated by a shaly zone. The core penetrates the upper part of the B dolomite, and does not penetrate into the shaly zone (Figure 3).

The gamma ray and resistivity for the entire well, as well as for the core interval, are shown in Figures 4 and 5. The Lake Ronel Oil Company took 21 plugs throughout the core and measured permeability, porosity, saturation and grain density on each plug. These plugs are no longer available, but the measurements are available and are discussed in Section 6.2.5.

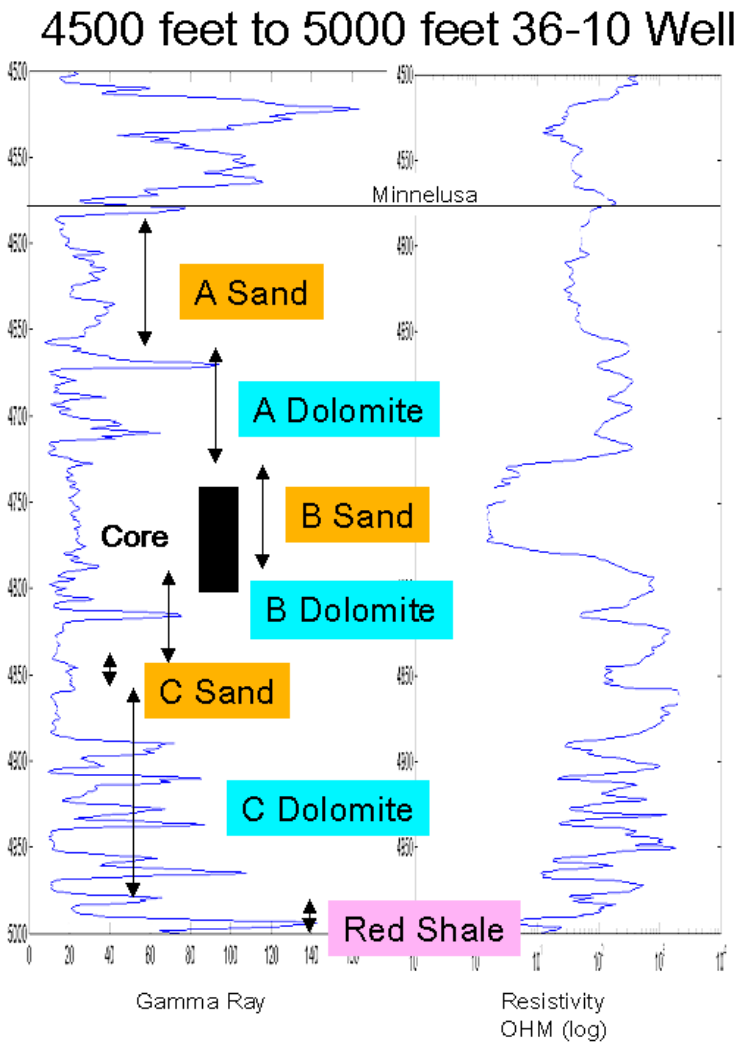

Figure 3. Well log between 4500 and 5000 feet depth superposed on interpreted sedimentary sequence. B dolomite gamma ray is often used as datum for electric log correlation. Note the sharp spike in the middle of the B: dolomite gamma ray kick. This is due to a shaly layer that separates two anhydrite-rich evaporitic dolomite B sequence. The naming convention is that of the published literature, called the "Shell System." Note that depositionally, B dolomite is closely tied to the underlying C sand, rather than the B sand.

6.2.4 Dune Morphology

The dune complexes have very distinctive geomorphic forms. Specifically, barchanoid dunes (Figures 4 and 5) are analogous to modern Saudi Arabian dunes shown in the satellite photograph in Figure 6. The Wyoming 3D seismic survey conducted by the Lake Ronel Company covers the State 36-10 well and shows clearly the development of barchanoid dunes and interdune complexes in the B sequence (Figure 7). Comparison with the modern analogue from Saudi Arabia shows striking similarity and consistency

between the geomorphology and the dominant wind direction. The 36-10 well penetrates one of the barchanoid dunes through the center of the dune complex (Figure 8).

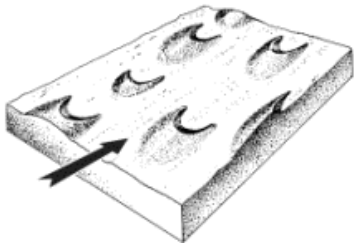

Figure 4. Plan-view barchanoid dune geomorphology from McKee, 1979. The black arrow indicates wind direction. Note the cusp-like shapes of the barchanoid dunes with respect to the wind.

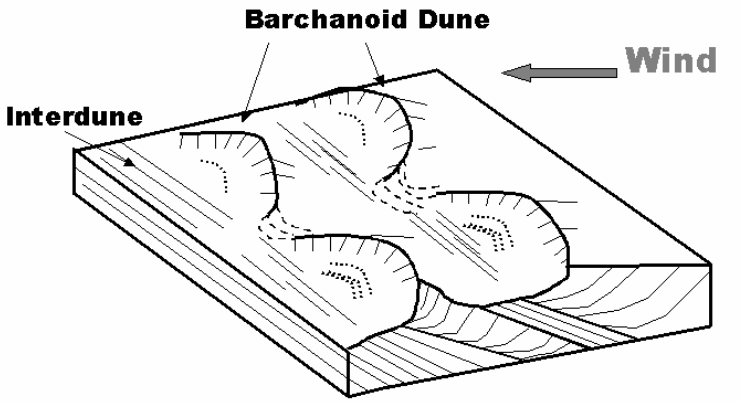

Figure 5. Cartoon drawing illustrating plan view and cross-sectional view of interdune and barchanoid dune complex.

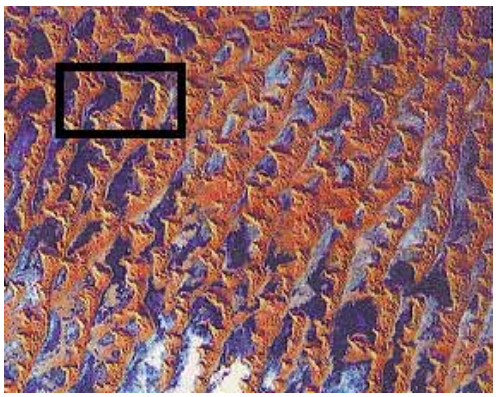

Figure 6. Satellite photograph of barchanoid dunes in Saudi Arabia (Sheffield, 1981). The rectangle represents the approximate area scale of the 3D seismic acquisition of the Wildcat field that covers well 36-10.

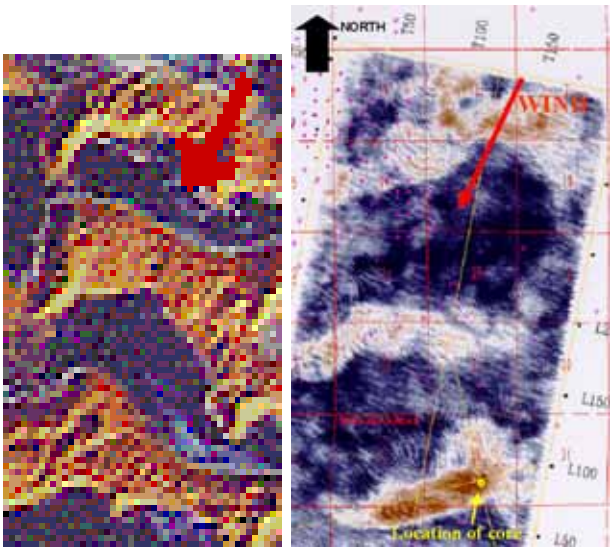

Figure 7. Comparison between modern barchanoid dunes from Saudi Arabia (left) and Wyoming seismic survey of the study area (right). The satellite photo is from the rectangular area in Figure 5, and rotated by 90 degrees to match the orientation of the wind direction and dune pattern in the seismic survey. The seismic survey is a relative amplitude time slice of Minnekahta + 28 msec (approximately at the top of sand sequence B from the Wyoming 3D data set. Brown areas (dune) are negative amplitudes (troughs) and blue (interdune) areas are positive amplitudes (peaks). The location of the core from well 36-10 is shown in yellow. This seismic amplitude map is consistent with a low-impedance sand bounded above and below by high-impedance carbonates and evaporites.

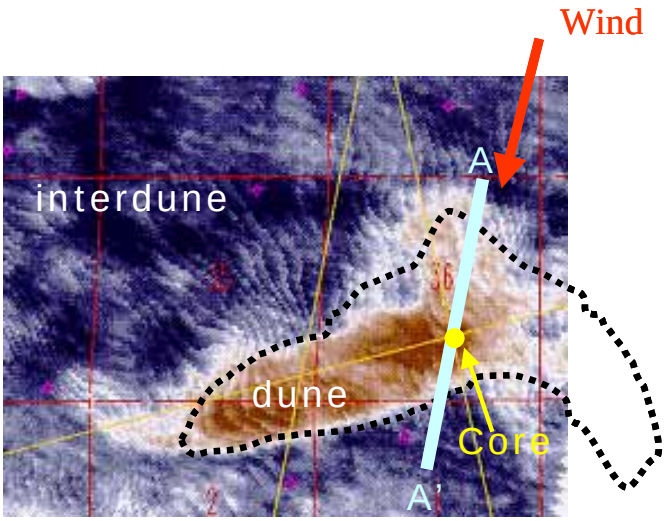

Figure 8. Close-up view of the seismic amplitude map in sequence B of the Upper Minnelusa Formation. Location of core taken in well 36-10 is shown in yellow. The core penetrates the center of the dune sand complex of sequence B, which appears as a negative amplitude (brown). The plan view of the dune geomorphology is barchanoid, and the presumed wind direction, based on the geomorphology, is northeasterly (red arrow). This is consistent with wind directions investigated by other workers such as Kelly et al., 1985. In Figure 9, a schematic model of the cross-sectional view through A-A' is shown.

Based on the cross-sectional geomorphology of typical barchanoid dunes (Figure 5) and studies of the overall Minnelusa Formation by Fryberger (1984), I produce a model of a sequence B dune (Figure 9). This model is a cross-section through line A-A' shown in Figure 8. The model takes into account the wind direction, dune/interdune deposits, and the vertical sequences shown in Figure 3. The cross-stratification of the dune sand complex is a preserved lee-side of the dune deposit as the dune migrated downwind. During lower Permian time, the topography was a low-relief with a gentle eastward slope (Fryberger, 1984), which is reflected in the model (Figure 9). Laterally, the Upper Minnelusa sandstone is part of the Wolfcampian sandstone that extends from North Dakota to Wyoming and beyond.

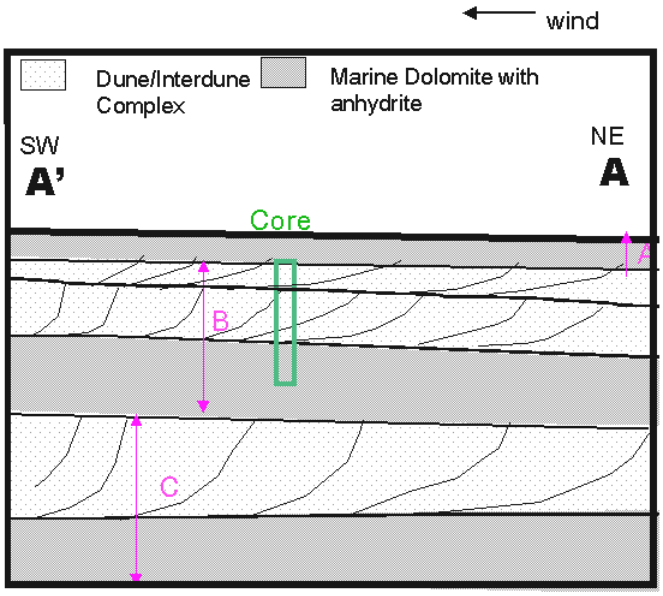

Figure 9. Schematic cross-section through A-A' in Figure 8. The core penetrates though sequence B, which consists of dune and interdune complexes as well as the marine dolomite. The B sequence overlays sequence C below and is underlain by sequence A above. There is no significant dip observed in the NE-SW direction, as studied by Fryberger, 1984; thus the layers are close to horizontal. Based on the later core analysis, sand B has perhaps 14-15 dune-interdune episodes (not shown here, but described in Figure 16).

6.2.5 Plug Measurement

Measurements on the 21 plugs taken by the Lake Ronel Company show higher porosity for eolian sands and lower or no porosity for marine dolomites. Around 4775 ft, where the marine dolomite B sequence begins, both the porosity and permeability drop

dramatically (Figure 10). The porosity and permeability of Lake Ronel core plugs are plotted together with the Fontainebleau sandstone data set (Figure 11). Fontainebleau sandstone is also well-sorted, clean eolian sandstone. The porosity-permeability cross-plots of the eolian sandstone of the Minnelusa core cluster in the medium porosity range, whereas the marine dolomite deposit data points are located at the low porosity and permeability end of the plot.. There is a single, anomalously low porosity measurement taken from the eolian core at about 4744 ft. This low porosity is most likely due to localized, patchy cementation. A thin section was made from such a patchy-cemented area and is shown in Figure 12.

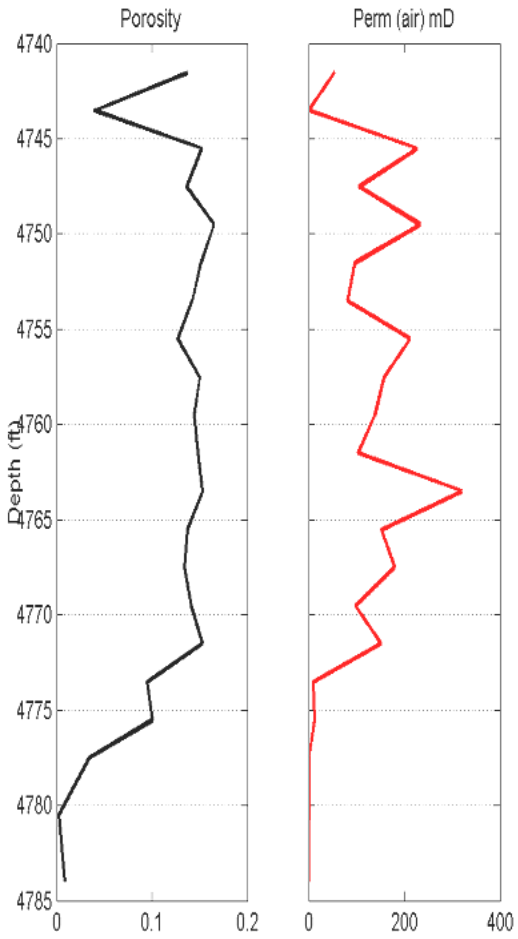

Figure 10. Porosity and permeability measured on the 21 plugs by the Lake Ronel Oil Company of Sand B. Note dramatic reduction in porosity around 4775 ft, where marine deposits (mostly dolomite) begin. There is an anomalously low porosity measurement around 4744 ft in the sand B sequence, where the plug was taken from a patchy cemented area. A thin section image of one such cemented areas was taken and shown in Figure 12.

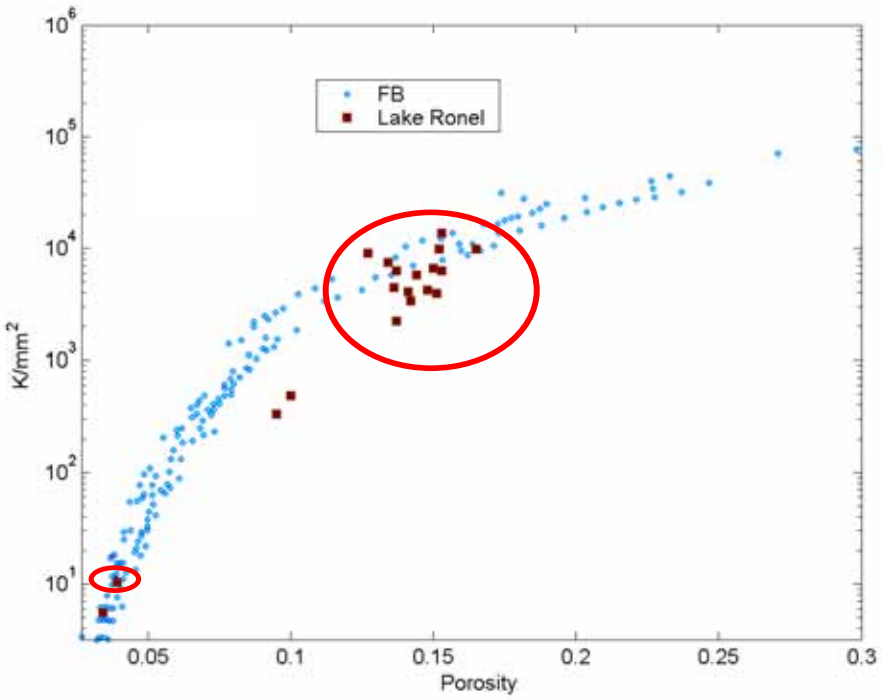

Figure 11. Normalized permeability vs. porosity of the 21 Lake Ronel core-plugs compared to Fontainebleau (FB) sandstone data. Sand B plugs are circled in red. There are three dolomite B plug measurements (outside the red circles). Overall, sand B measurements have higher porosity and permeability. However, there is a single measurement of sand B at very low porosity. This is due to the heterogeneity within sand B-- a patchy cement was observed in some parts of the core. The Fontainebleau permeability is normalized by .25x.25 mm^2, which is the square of the average grain size for that data set, while the Lake Ronel permeability is normalized by .1.5x1.5 mm^2.

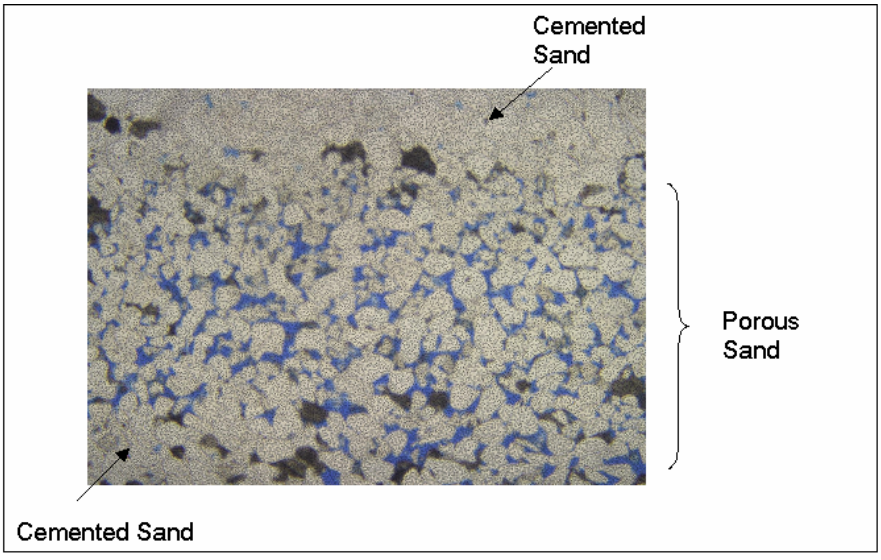

Figure 12. Thin section image of the upper part of sand B, showing patchy cementation. The blue part is the pore space.

6.3. Core Description and Thin Section Analyses

6.3.1 Overview of the entire core

The upper part of the 60 ft core consists of the B sand, which is cross-bedded eolian sand interbedded with thin parallel lamination (interdune deposits). The sand B (Figure 13) overlies dolomite B (Figure 14). The sand B eolian deposits are red sandstone, fine to medium grained and well sorted, with high porosity and permeability. In contrast, dolomite B has very little porosity and contains massive anhydrite precipitations. A composite display of the entire 60 ft core is shown in Figure 15.

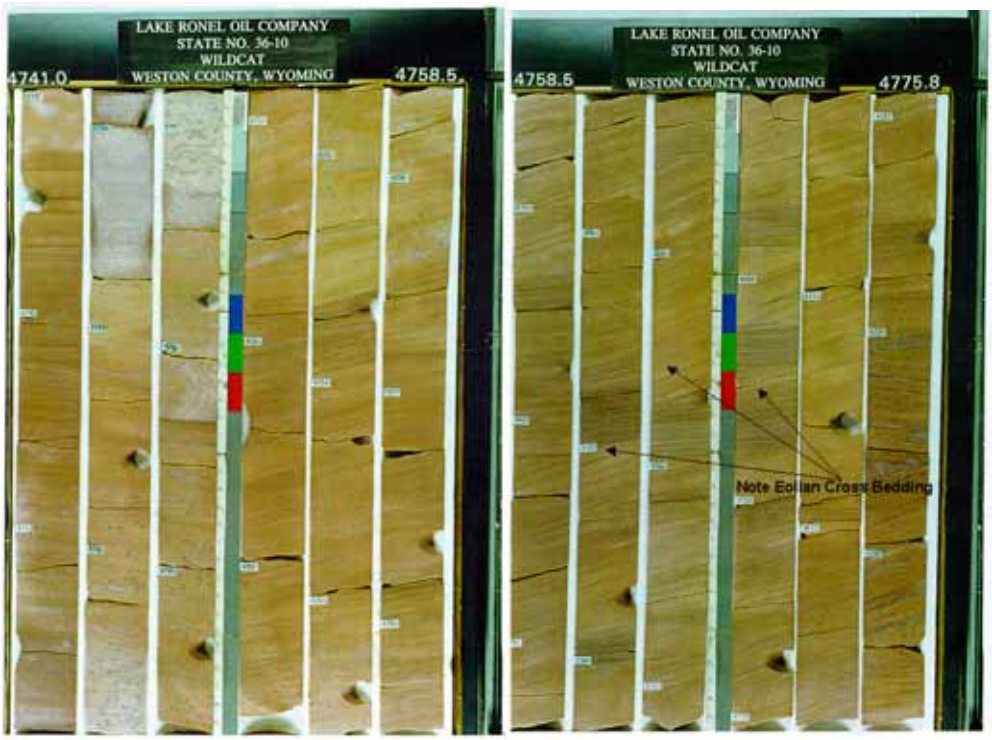

Figure 13. Lake Ronel State 36-10 well core Sequence B sands, from 4741.0 ft to 4775.8 ft. These are dune and interdune deposits. Note clean sands and cross-stratifications. The holes indicate locations where Lake Ronel Company took plugs for measurement.

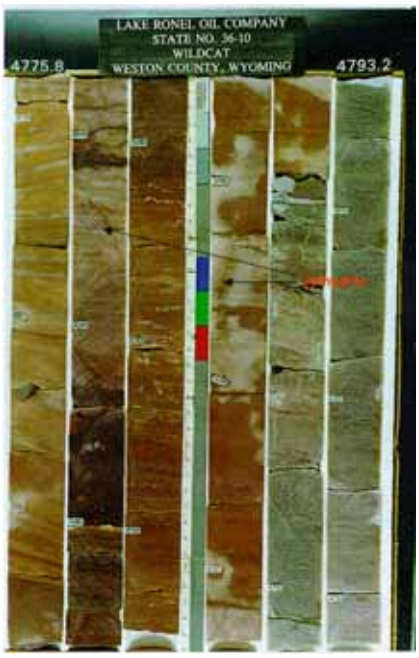

Figure 14. Lake Ronel State 36-10 well core Sequence B marine dolomite, from 4775.8 ft to 4793.2 ft. This marine dolomite consists of red and gray dolomite with extensive anhydrite patches. Some laminations are visible, mostly discontinuous and massive.

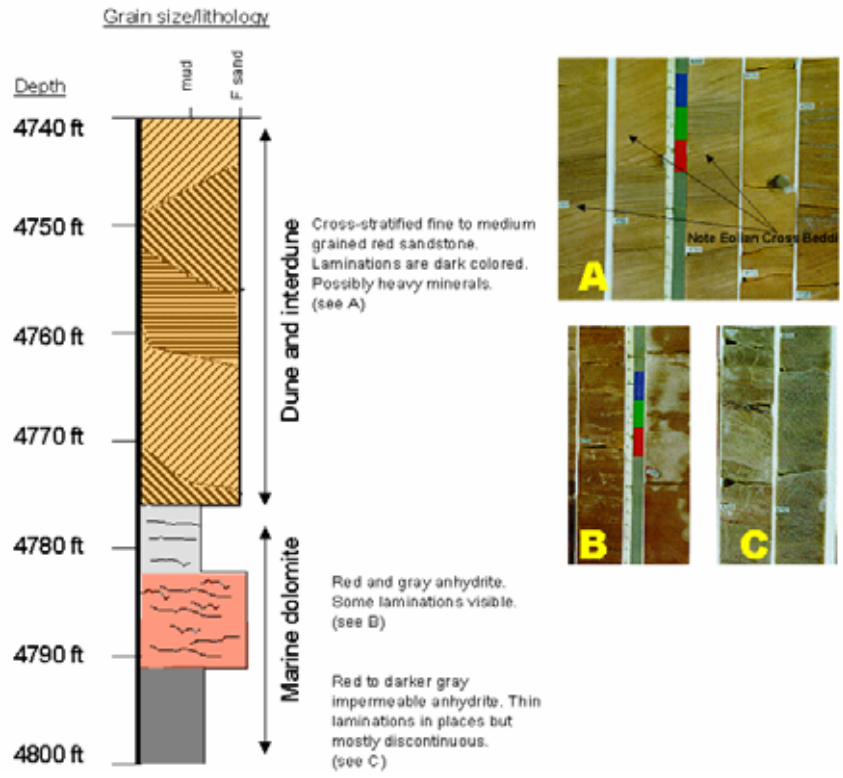

Figure 15. Summary of Figures 13 and 14.

6.3.2 Detailed description of sand B

I describe the sand-B segment of the core in detail using the lithofacies described in the Minnelusa cores studied by Fyberger (1984). Based on this lithofacies scheme, the sand-B portion of the core displays mostly dune or interdune deposits.

Dune deposits in Minnelusa are either steeply dipping avalanched-produced strata or more shallow dipping ripple-produced strata (Fryberger, 1984). Avalanche-produced strata have 1-2 centimeters thick inverse-graded beds, and fade-out lamination typical of avalanche-produced strata in dry dune sands (Fryberger, 1984). The ripple-produced deposits are finely laminated and often contain recognizable cross-sections (in core) of wind-ripples (Fryberger, 1984). On the other hand, interdune and sand sheet deposits are normally nearly flat-lying, and consists of stacks of fine laminae, some of the wind – ripples can be seen in the core (Fryberger, 1984).

I identified 14-15 flat-laminated intervals, interbedded with dipping strata, in the sand B section of the core (Figure 16). Based on Fryberger's (1984) observation and lithofacies scheme for Minnelusa sandstone, this could be indicative of dune-interdune sequence. In fact, such vertical dune-interdune sequence is observed in many wells across the Powder River Basin in the Minnelusa Formation (Fryberger, 1984). Laterally, this dune-interdune system was quite extensive, ranging from North Dakota to Wyoming and beyond (Fryberger, 1984).

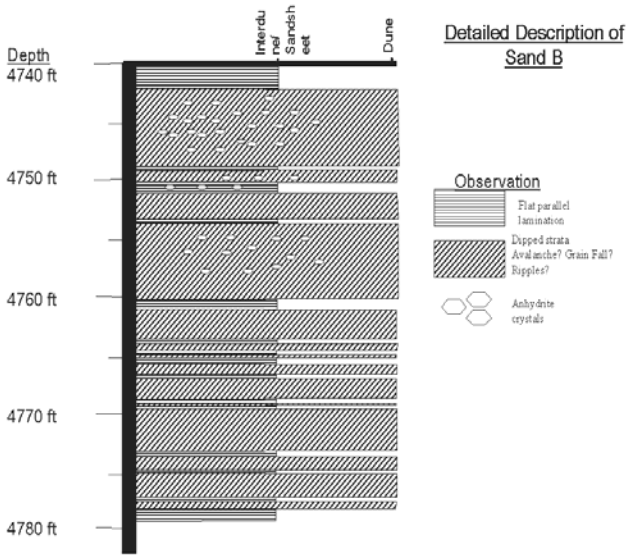

Figure 16. Detailed description showing interchanging flat lamination and dipped strata for sand B of the Well 36-19 core. The dipped strata may be avalanche, grain-fall, or ripple-produced. This may be a vertical sequence of about 14 dune-interdune intervals.

X-ray diffraction analysis on a sample from this unit reveals that the sandstone is mostly quartz (86 %) with small amounts of dolomite, anhydrite, and K-feldspar (Figure 17). These non-quartz minerals occur both as granular detrital material and cement. I do not observe dark minerals in laminae. The core is overall light color and pink, probably from K-feldspar and possibly anhydrite.

X-Ray Diffraction Data

Bulk Mineralogy														
Quartz	Plagioclase	K-Feldspars	Calcite	Dolomite	Siderite	Ankerite	Clinoptilolite	Analcime	Gypsum	Anhydrite	Barite	Pyrite	Hematite	Total Clay
86	0	3	0	6	0	0	0	0	0	4	0	0	0	1

Figure 17. X-ray diffraction for a sample from sand B. The sandstone mostly consists of quartz, but also includes small amounts of K-feldspar, anhydrite and dolomite.

6.3.3 Diagenesis Observed in the Thin Section Images: Sand B

Overall, sand B consists mostly of rounded quartz grains with overgrowth cement, with some laminations. There are also detrital, rounded dolomite grains as well as dolomite cement. Large pore space is often occupied by anhydrite cement. There is very little clay and a minor amount of K-feldspar.

In Figures 18-23, I show thin-section images that I photographed under the microscope. Sedimentary fabrics such as laminations of quartz grains are observed (Figure 18). These laminations are bands of smaller, well-sorted quartz sand grains within the larger quartz grain zone. Quartz grains show overgrowth, where euhedral rims of quartz cementation have grown around the original grains (Figure 19). There are also dolomite grains that show deformation, possibly fractured and altered during the process of lithification (Figure 20, 21, 22).

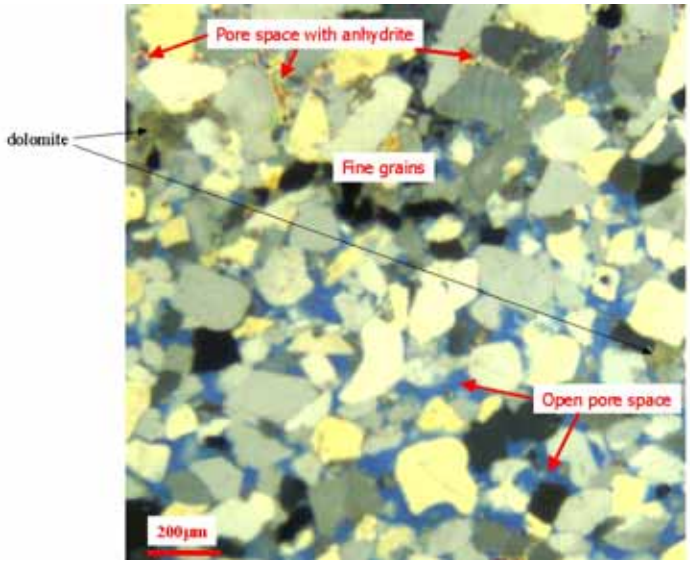

Figure 18. Thin-section image from the upper part of sand B showing patchy cementation and its relationship to grain fabric. The upper part of the thin section image is filled with anhydrite cement (rainbow-color), whereas the lower part is open pore space (blue). The quartz grains appear as shades of yellow, gray, and black. Anhydrite cement has high-interference (bright color, like rainbow) as indicated in the image. There are dolomite grains and cements throughout the image as indicated by brown colors, a few of them are indicated by black arrows. Early cementation of anhydrite in dune sand, later dissolved, facilitated by good sorting, led to secondary porosity in many Minnelusa dune sands (Kelly et al., 1985). This thin section can be a testament to the localized secondary porosity. However, the anhydrite cementation may also have been prevented in the currently open pore space due to small grain size acting as a fluid flow barrier, thus the open pore space may be primary porosity, not secondary porosity.

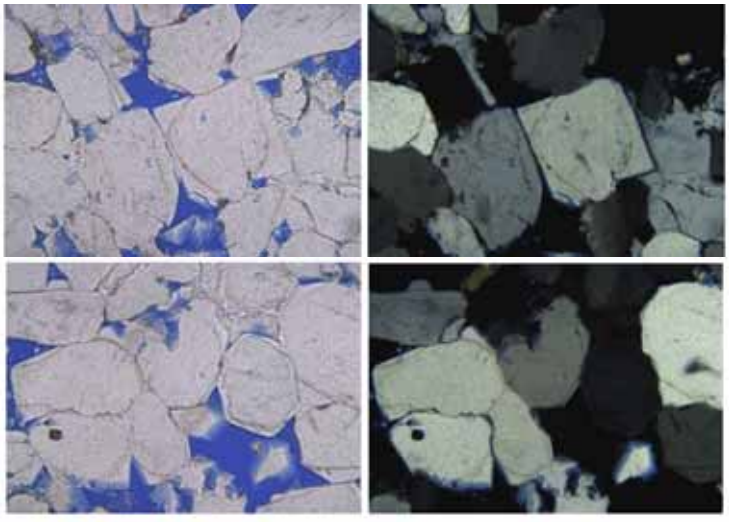

Figure 19. Images of quartz overgrowth observed in the eolian sand B from the Minnelusa Formation. Note the euhedral crystal growth around the originally rounded grains.

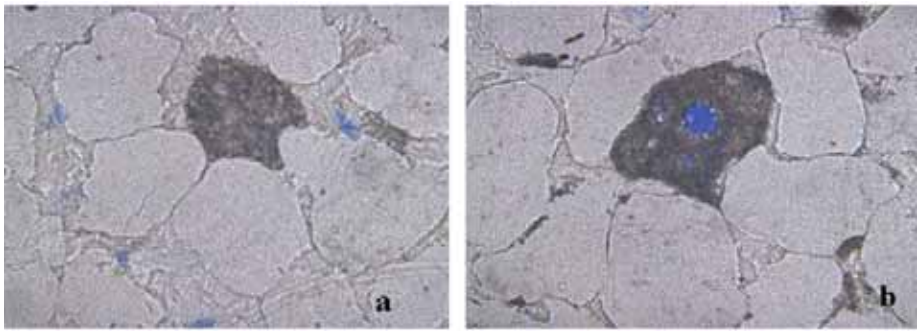

Figure 20. Dolomite (brown) in the sample. a) Dolomite grain, surrounded by similar sized quartz grains. The pore space is filled with anhydrite cement. The dolomite grain shape is conforming to the surrounding quartz grains; the grains may have fractured at an early stage of lithification. b) Dolomite grain with an empty pore space (blue) in the middle. It might be a sign of dissolution.

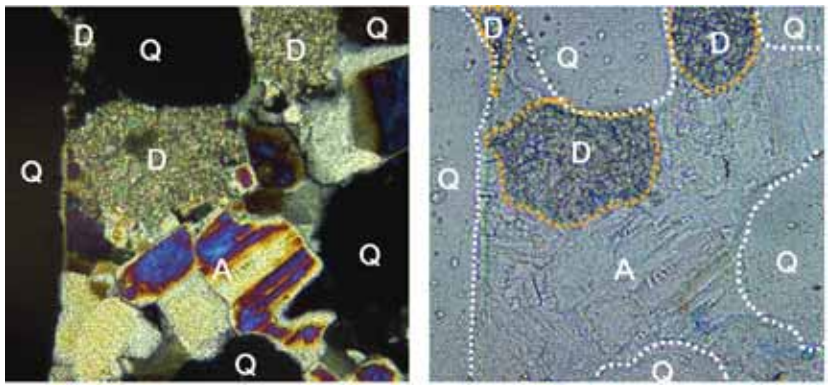

Figure 21. Dolomite surrounded by anhydrite cement. D is for dolomite, Q is for quartz and A is for anhydrite. Anhydrite cementation probably occurred after dolomite precipitation or deposition.

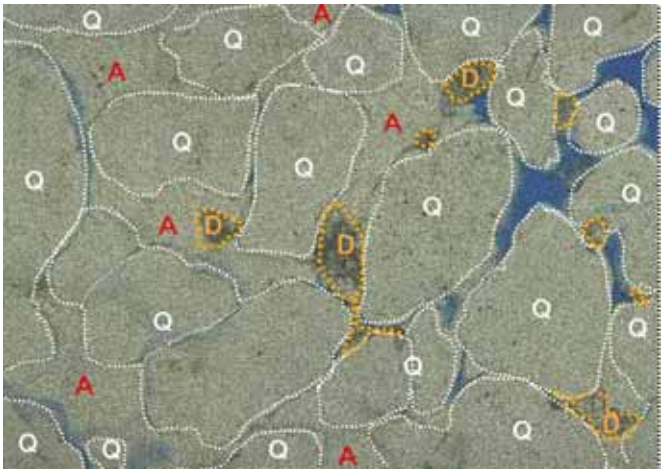

Figure 22. Quartz grains and dolomite grains (showing deformation and recrystallization) surrounded by anhydrite cement.

The pore space, in some localized areas, is mostly filled with anhydrite cementation, which shows a characteristic high interference and rectangular cleavage (Figure 23). Kelly and others (1985) have found that in the Minnelusa sandstone, early cementation of gypsum (later altered to anhydrite) in dune sand dissolved during further diagenesis and created secondary porosity in many of the well-sorted sandstone. This depositional-fabric-controlled dissolution led to many dune sands in this area having good porosity.

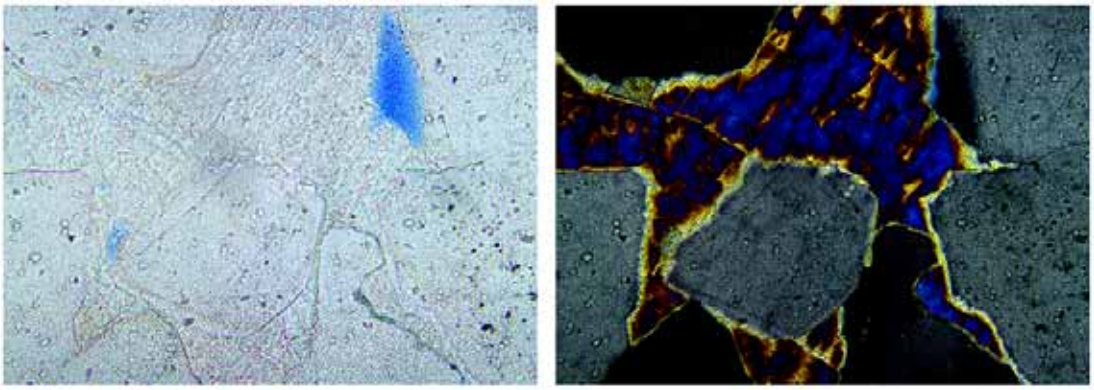

Figure 23. Anhydrite cement, filling the pore space between quartz grains, under normal (left) and cross-polar (right) light. The cement has rectangular cleavage and has high interference as indicated by the bright coloring under cross-polar light.

In summary, at the time of deposition, sand B contained quartz with a few dolomite or anhydrite grains. There may have been small amounts of clays or other unstable minerals, but there is no trace of them left in the thin sections. The well-rounded, well-sorted eolian sands had natural sedimentary fabric (lamination). There may have been rounded dolomite grains deposited at the same time, but later some of those grains were deformed and recrystalized during diagenesis (Figure 20, 21, 22).

Detrital anhydrite grains may have been present initially and may have become seeds for anhydrite cementation during diagenesis. However, it is also possible that evaporite-rich fluid entered the system and deposited pore-filling cements. In any event, at an early stage, anhydrite cemented some pore spaces (Kelly et al., 1985). However, during further diagenesis these anhydrite cements dissolved from some pore spaces (seemingly correlating to well-sorted sands) leaving secondary porosity in the centers of the dunes. A possible source of evaporitic cement can be from an evaporitic marine, lacustrine or

pond-like environment near the dunes, because the Minnelusa Formation is a coastal dune field.

6.3.4 Diagenesis Observed in the Thin Section Images: Dolomite B

Dolomite B is located below the above-described sand B. To understand the nature of diagenesis in this depositional environment, I have taken selected thin sections from approximately 20 ft of the dolomite B section (Figure 24).

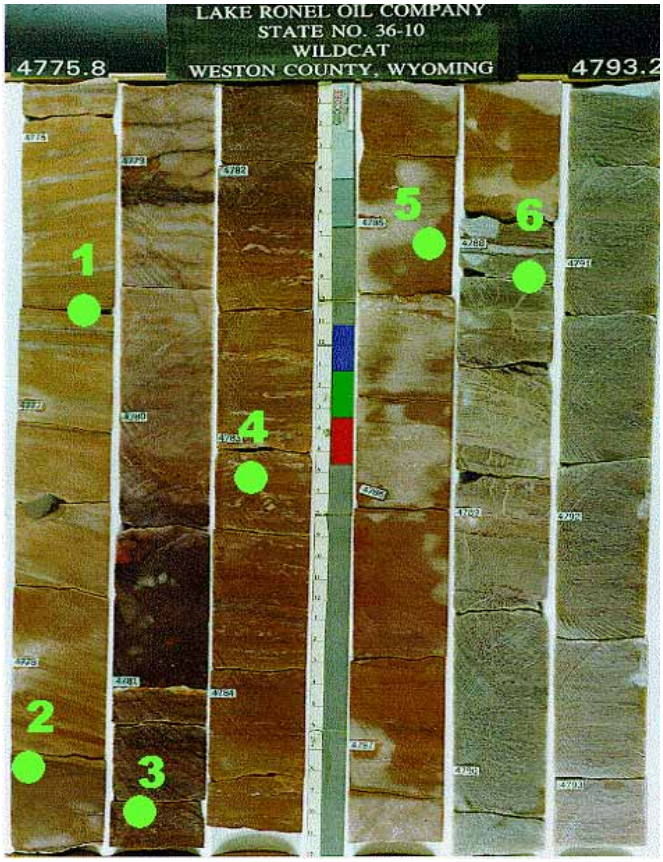

Figure 24. Locations of 6 plugs taken from the dolomite B section. Thin sections were made from these plugs. They are not the same plugs as the 21 plugs previously taken by Lake Ronel Company, which are lost and no longer available for thin section analyses.

The figure below describes the observations of each of the thin sections from the six plugs taken from dolomite B section (Figure 25). The first plug, at a depth of 4776.7 feet, is still part of the sand B sequence, consisting of quartz sands and a few dolomite grains (Figure 26). The quartz sand grains are fine and probably eolian in origin.

#	Depth (ft)	Observation of Thin Section* * Observation courtesy of Don Lowe	Possible Environment	Photos
1	4776.7	Sandy. Well compacted silica showing overgrowth, either happened in place or inherited. Contains very fine dolomite.	Eolian/Dune	Figure 26
2	4778.4	Contains more sand-sized dolomite grains than thin section #1. Huge dolomite grains are also present, along with some anhydrite. Dolomite grain size suggests close transport.	Dune, near dolomite source (marine-coastal?)	Figure 27
3	4781.5	Massive anhydrite with orthogonal cleavage. Inside the anhydrite cement, there is disseminated quartz sand, 0.1 –0.2 mm fine grain, eolian in origin and K-feldspar (probably windblown).	Marine/lacustrine/ pond-like environment with some eolian sands blowing in by wind	Figure 28
4	4783.2	Mostly anhydrite, more windblown quartz than #3, possibly closer to dunes than #3 or aqueous currents transporting in some quartz grains, as the grains are coarser (0.3 mm). Minor number of dolomite grains. There are layers rich in sand and layers rich in anhydrite.	Marine/lacustrine/ pond-like environment but closer to sand dunes than #3 or water transporting in sand grains	Figure 29
5	4785.1	Clastic, mostly quartz with spotty anhydrite pore-filling cement and dolomite cement. Dolomite cement preceded anhydrite cement as dolomite lines grain margins. Few dolomite grains. Quartz grains are 0.3 mm size, which is too large to go too far by air unless there is high wind speed event such as hurricanes. Can not determine any further information.	Deposition by water? Air? Sabhka?	Figure 30
6	4788.1	Mostly dolomite, with patch of anhydrite, very few quartz grains, no fossils. Less evaporitic environment, possibly subaqueous. Quartz grains blown via air, not bed load.	Subaqueous. Coastal or marine environment	Figure 31

Figure 25. Summary of thin section observation and possible depositional environment of 6 core plugs taken from dolomite B section.

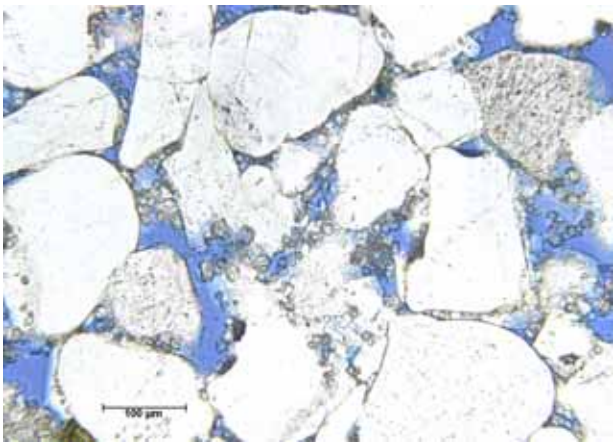

Figure 26. Thin section image of plug #1 photographed under the microscope by Ayako Kameda. Eolian sand grains (white) with sand-sized dolomite grains (spotted-gray). Blue is pore space.

The second plug, about 2 feet below, contains more sand-sized and larger dolomite grains, suggesting close transport (Figure 27). This suggests a dune environment, but near a dolomite source, perhaps a more marine-coastal environment than the first plug.

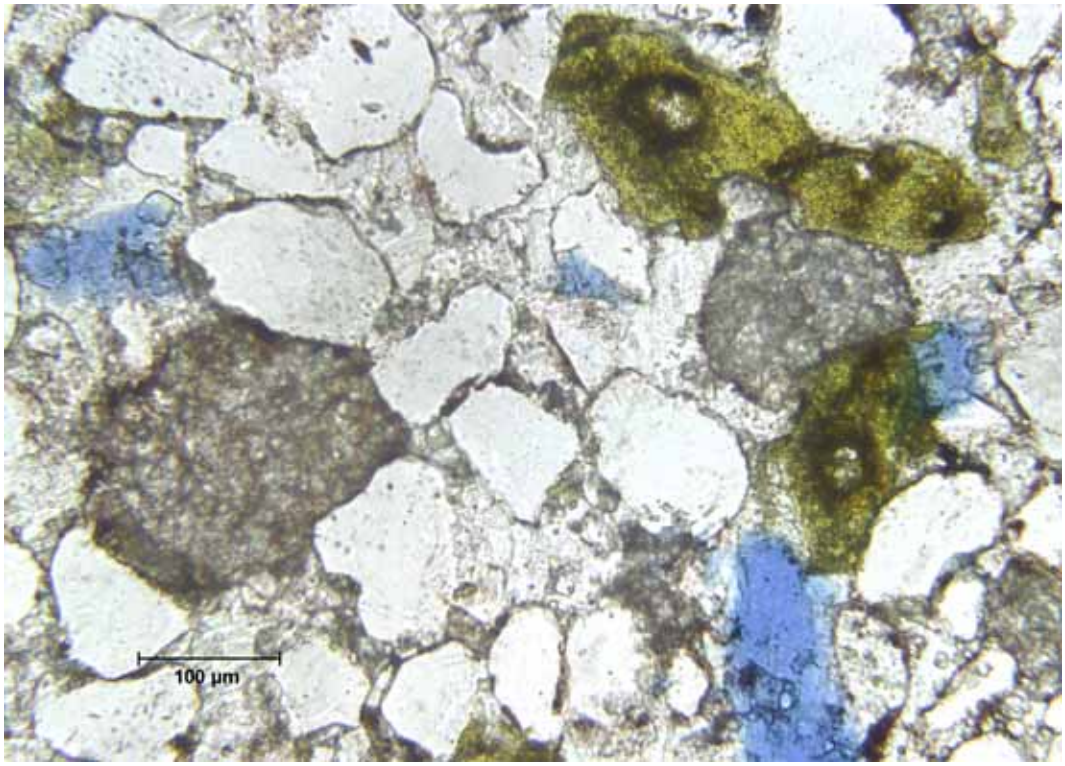

Figure 27. Thin section image of plug #2 photographed under the microscope by Ayako Kameda. Eolian sand grains (white) with sand-sized dolomite grains (spotted-gray). Gray-white matrix is anhydrite. Blue is pore space. Note the large dolomite grains, larger and occurring more frequently than the previous plug (Figure 26).

The third plug at 4781.5 feet is a massive anhydrite with orthogonal cleavage with disseminated fine-grained quartz sand, probably eolian in origin and wind-blown (Figure 28). The massive anhydrite is probably from a marine, lacustrine or pond-like environment where there are evaporites and some eolian sands that are blown in by wind.

The fourth plug at 4783.2 ft consists mostly of anhydrite with more quartz than the previous plug (Figure 29), suggesting a closer environment to dunes than the previous environment. But the environment probably had more access to aqueous currents, as the grains are coarser (about 0.3 mm). There are layers rich in sand and rich in anhydrite. All these indicators suggest that plug #4 is from a marine, lacustrine or pond-like environment with more dune influence, or closer to water current than plug #3.

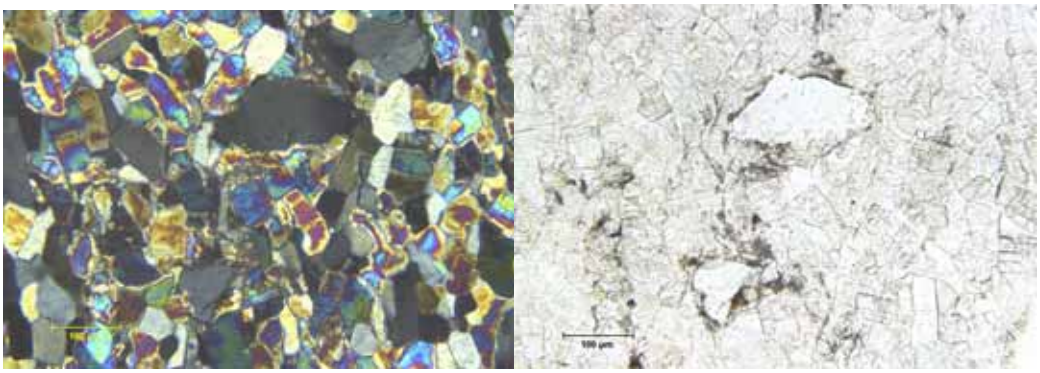

Figure 28. Thin section images of plug #3 photograph by Ayako Kameda. Rainbow color (left) and orthogonal cleavage (right) are indications for anhydrite. Here, anhydrite is massive, with very few quartz grains, which show up as gray (left) and white (right).

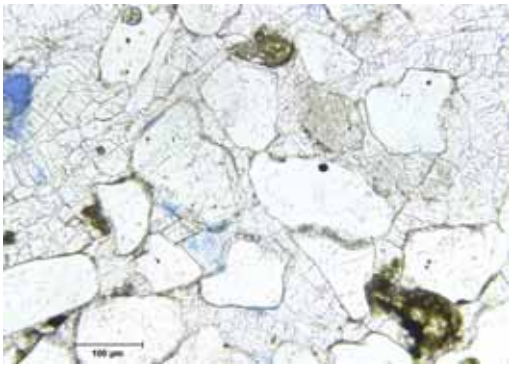

Figure 29. Thin section image of plug #4. The pore-filling cement with orthogonal cleavage is anhydrite. Here, anhydrite is massive, with more quartz grains than seen in plug #3. The quartz grains are coarser as well. Photograph by Ayako Kameda.

The fifth plug at 4785.1 ft is clastic with mostly quartz and patchy anhydrite cementation and dolomite cementation (Figure 30). Dolomite may have preceded anhydrite cement, as dolomite lines the grain margins. Quartz grains in this thin section are large, about 0.3 mm in size. Grains of this large size may be too large to be transported by air. This suggests a non-airborne mode of deposition, perhaps by water. The environment of this deposit is difficult to determine. One possibility is that it is a sabhka. However, large grains can be deposited by air with a high wind speed. More information is needed to determine the depositional environment.

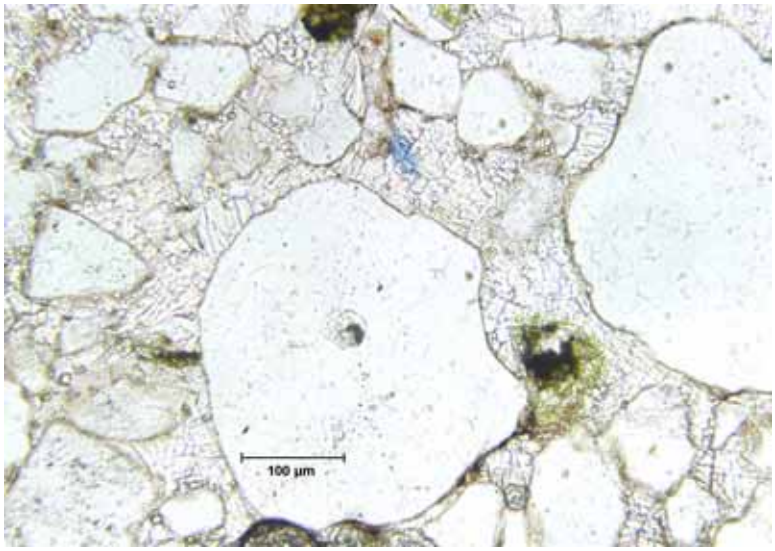

Figure 30. Thin section image of plug #5. The pore-filling cement with orthogonal cleavage is anhydrite. The sample is clastic and contains patchy anhydrite cementation. The large quartz grains (white) are indication of non-airborne transport. Therefore, this clastic sample is certainly near the dune fields but not deposited by air. Dolomite is seen as a darker grain at the bottom of the image. Photographed under the microscope by Ayako Kameda.

Finally, the sixth plug is at 4788.1 ft and is part of a gray, mostly dolomite segment of the core. The thin section indicates that the plug is mostly dolomite with patches of anhydrite and very few quartz grains (Figure 31). This is a less evaporitic environment (no massive anhydrite) but more marine (mostly dolomite) in origin. Quartz grains are sparse but small, and the size indicates that they were blown in by air.

The overall observation of plugs 1-6 indicates a transition in environment from dune dominated environment to shoreline sandstone to marine dolomite, a vertical sequence commonly observed in the Minnelusa Formation cores in the area (Figure 2) due to transgression-regression cycles. In the dolomite B sequence of the core, based on the thin section analyses, the tendency is to go from sand-rich to dolomite-rich environment with some evaporitic (indicated by massive anhydrite) environment in between. The porosity and permeability are very sensitive to these changes. In the eolian sand “B: section, the measured porosity can reach on average 16%, while in the transition zone near plug #1 the porosity drops to about 11 %, and there is virtually zero porosity and permeability in the anhydrite- or dolomite-rich sections.

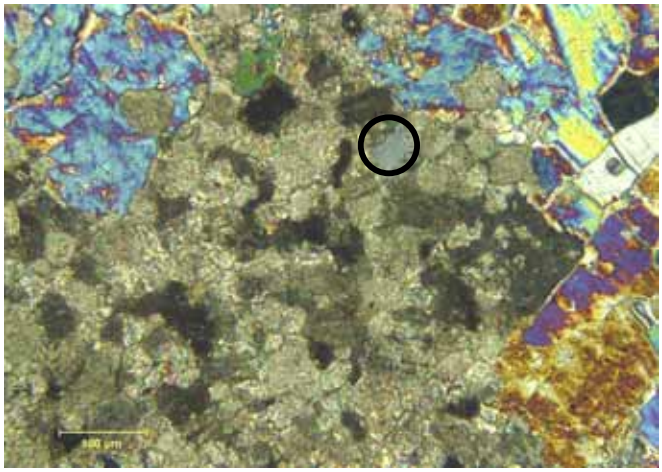

Figure 31. Thin section image of plug #6. The rainbow-colored patchy cement with orthogonal cleavage is anhydrite. The sample is mostly dolomite (yellowish brown that dominates the thin section image). There are very few small quartz grains present (gray, circled in black) which suggests airborne transport. This is probably a more marine origin with a few eolian sand grains blown in by air. Image photographed under the microscope by Ayako Kameda.

6.4 Summary of Depositional Environment and Diagenesis

The thin section analysis suggests that three depositional environments are present in the core under examination: (1) a dune environment with mostly fine quartz sand grains with few dolomite grains, (2) a more evaporitic environment with mostly anhydrite and few quartz and dolomite grains, and (3) a more marine environment with mostly dolomite and very few quartz grains.

After the deposition, the sediments were buried, and the current depth is 4700 ft. For sandstone with mostly quartz composition, mechanical compaction is the main diagenesis process during the initial burial stage. The temperature for mechanical compaction for quartz-dominated sandstone ranges from about 10 ^{o}C to about 24 ^{o}C (Boggs, 1992). The next stage of diagenesis involves more chemical porosity loss via dissolution of quartz and anhydrite cement, which leads to secondary porosity development (Kelly, 1985). The approximate temperature range for this stage is suggested to be from 24 ^{o}C up to over 200 ^{o}C (Boggs, 1992). The present day temperature at 4500 ft depth is about 40 ^{o}C. The uplift and erosion of 250 m is suggested for this area in some simulations (Pollastro and Schenk, 1991), but not much is known. Since there is no indication of super-mature stages of diagenesis where even secondary porosity is destroyed, the Minnelusa core was probably exposed to semi-mature to mature stages of diagenesis where primary porosity

reduction and the presence of secondary porosity can be found. Based on this information, the flow chart for possible diagenesis in the Minnelusa samples is summarized in Figure 32.

In the next chapter, I simulate compaction, quartz overgrowth, and patchy cementation (anhydrite) of the sand B section. Since the Dolomite B section has preserved very little porosity, and I cannot determine for sure its depositional origins or diagenetic paths, I do not model them in the next chapter. But if provenance, depositional environment, diagenesis and burial history can be worked out for dolomite B, it is possible to conduct a site-specific simulation using digital rock technology.

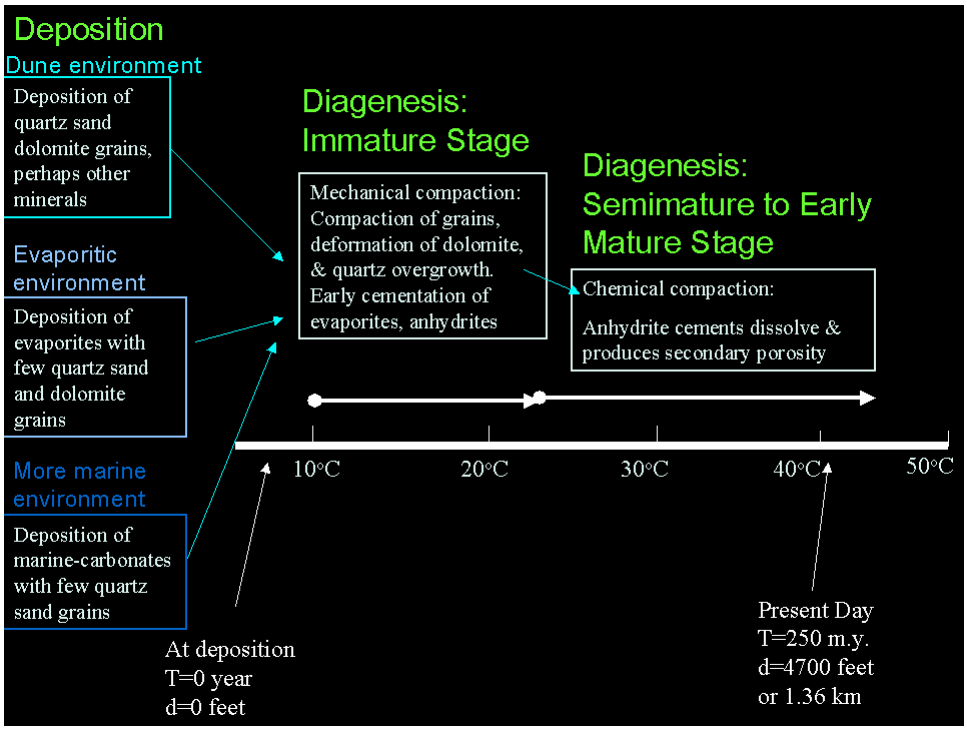

Figure 32. Flowchart summarizing the geologic history of the Minnelusa Core Sandstone B and Dolomite B based on previous workers' conclusions and thin section analyses done in this study. Overall there are three major groups of depositional groups. The deposited sediments were probably subjected to compaction of quartz grains, deformation of dolomite grains, and early cementation of evaporites (later anhydrites). At a higher temperature and further burial, the rocks later experienced dissolution of some of the anhydrite cements in the sandy part of the Minnelusa core. Approximately 250 million years after the deposition, the current depth is about 4700 ft.

6.5 References

Boggs, S., Jr., *Petrology of sedimentary rocks*, Macmillan Publishing Company, New York, 1992.

Fryberger, S.G., The Permian and Pennsylvanian geology of Wyoming, in *Guidebook-Wyoming Geological Association*, **35**, 241-271, 1984.

Kelly, A.O., J.C. Horne, C.L. Reel, and M.A. Sares, Facies control on oil production from Upper Member of Permo-Pennsylvanian Minnelusa Formation, Powder River Basin, Wyoming, *AAPG Bull*., **69**, 5, 852, 1985.

McKee, E., An introduction to the study of global sand seas. In A Study of Global Sand Seas, E. McKee, ed., pp. 1- 20. Washington, *U. S. Geological Survey Paper,* **1052**, 1979.

Pollastro, R.M., and C.J. Schenk, Origin and diagenesis of clay minerals in relation to sandstone paragenesis; an example in eolian dune reservoirs and associated rocks, Permian upper part of the Minnelusa Formation, Powder River basin, Wyoming, *AAPG Bulletin*, **75**, 6, 1136-1137, 1991.

Sheffield, C., *Earth watch; a survey of the world from space*, Sedgwick and Jackson, London, United Kingdom, 1981.

Chapter 7
Case Study Part 2: Modeling Eolian Core from the Minnelusa Formation, Wyoming, Using CT-Scanned Images

That is the essence of science: ask an impertinent question, and you are on the way to a pertinent answer.
–Jacob Bronowski (The Ascent of Man)

7.1 Abstract

In this chapter, I apply the virtual rock physics tools introduced in the previous chapter to a real data set. The main objective is to show how a prototype rock can be numerically moved through geological time and also through space. Moving through time means imposing compaction and diagenesis upon prototype rock. Moving through space means altering rock to reflect diagenesis conditions away from its initial location. I show how an eolian prototype can be digitally altered to arrive at a target which is Permian eolian sandstone and that the porosity and permeability of the altered prototype match these properties measured on the target.

7.2. Methodology

The data come from a core taken from the Minnelusa Formation, Wyoming. The Minnelusa Formation is a Permian coastal dune and marine dolomite deposit (Fryberger, 1984). The depositional and diagenetic processes that affected the Minnelusa rocks were analyzed in the previous chapter. In this chapter, such processes are divided into several elemental algorithms to simulate the geological processes on digital rocks.

The digital images used are CT-scanned images of sandstone plugs, as well as an eolian prototype, Año Nuevo, produced from loose sands taken from a modern eolian depositional environment. The basic numerical tools thus far developed, such as diagenesis tools, fluid flow tools, and the prototyping concept, will all merge in this case study to outline a new method where various numerical experiments can be conducted on a digital rock-physics platform.

Digital pore topology for the Minnelusa core is obtained via X-ray tomography (CT-scan) of two core plugs from the sand B section, as well as a thin-section image (Figure 1). In addition, an eolian prototype is created in the laboratory by packing unconsolidated Año Nuevo eolian sands and then CT-scanning the sample.

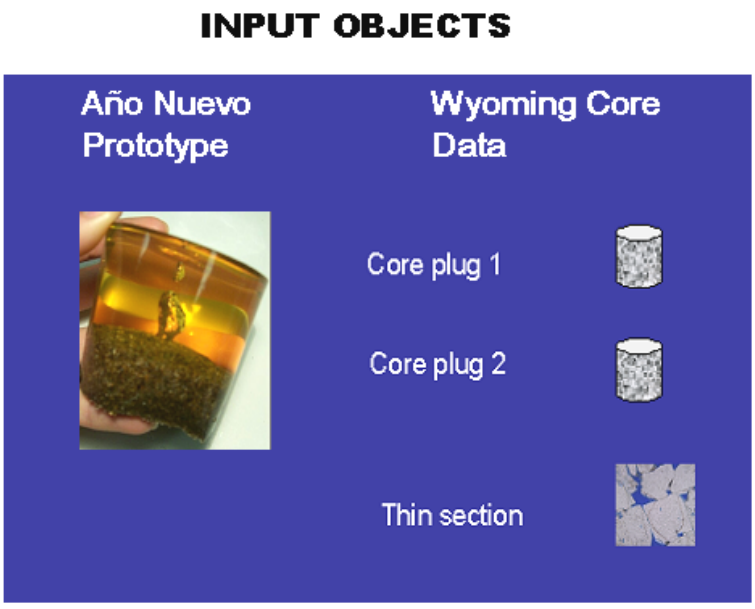

Figure 1. Physical input objects whose digital images are used in this chapter: two core plugs, a thin section image from sand B, as well as the Año Nuevo eolian prototype.

The digital pore images are then used to compute permeability and porosity using Lattice-Boltzmann fluid simulation, as described in the earlier chapters. Then, the computed permeability values are compared to the measured permeability. This procedure can help determine how reliably digital rock technology can be used to predict permeability and porosity.

The diagenetic tools introduced in the previous chapter are applied to the eolian prototype. The ultimate goal is to predict the porosity-permeability evolution in time and in space. To accomplish that goal, I first model the transformation in space using thin section (Figure 2, Step 1A), then model the transformation in space using core plugs (Figure 2, Step 1B), and finally model the transformation of the eolian prototype in time into the Wyoming core plugs (Figure 2, Step 2).

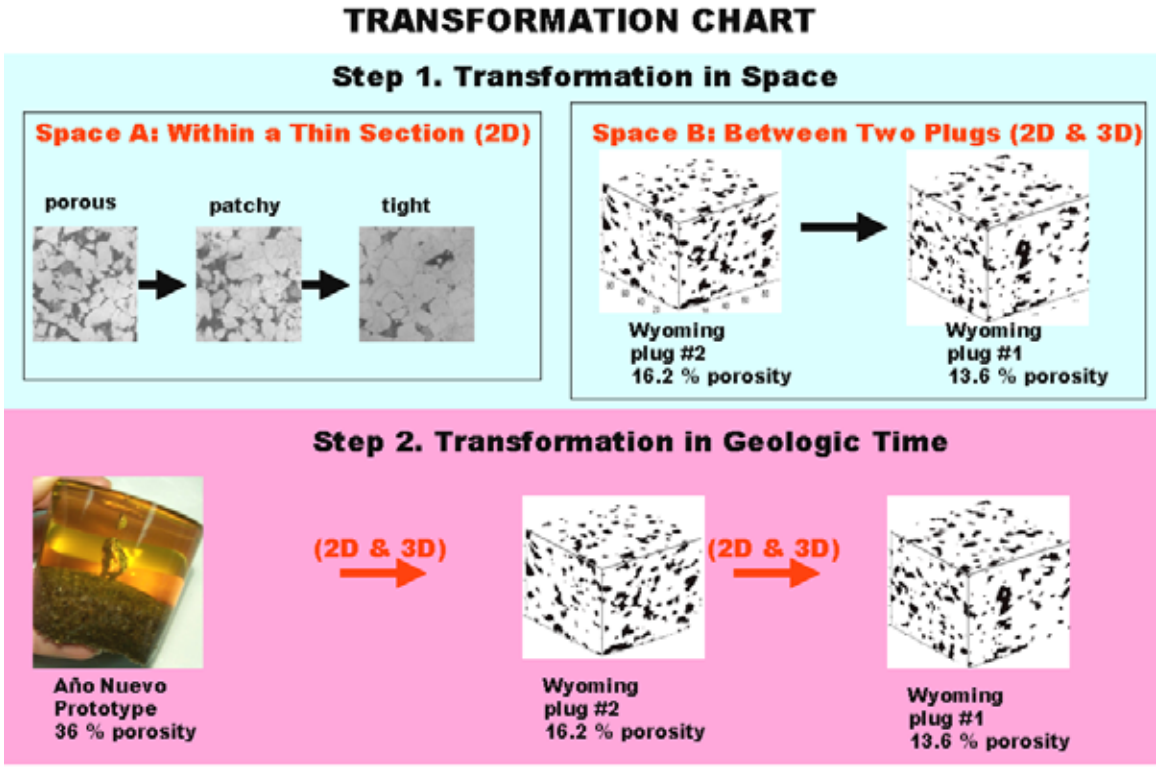

Figure 2. Transformation chart for Chapter 7. Step 1 involves transformation in space, while Step 2 involves transformation in time. The input objects for the transformation are listed in Figure 1. "2D" means that a 3D pore space is statistically constructed from a 2D pore space image. "3D" means that digital alterations are directly applied to 3D CT scans of the physical samples.

7.3. Digital Images

7.3.1 Source of Images Used in Chapter 7

Three different types of images are used in Chapter 7: (1) an eolian prototype packed in the laboratory from unconsolidated dune sand collected from Año Nuevo, CA; (2) a thin section taken from the sand B section of the Wyoming core; and (3) two plugs (#1 and #2) from the sand B section of the Wyoming core with slightly varying degrees of anhydrite cementation.

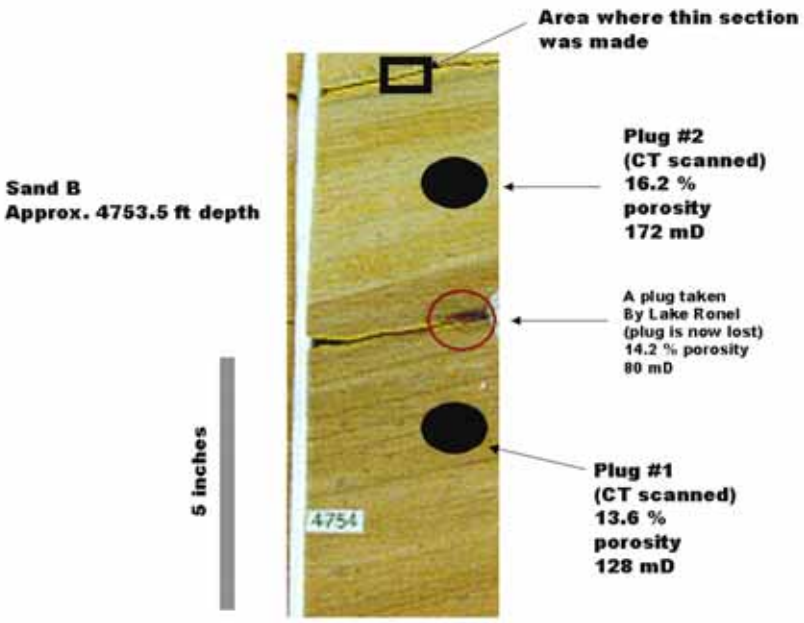

Figure 3. Sandstone B digital images are taken from the part of the core displayed above. The orange arrows indicate some of the gray anhydrite cement spots. Locations of Wyoming core plugs #1 and #2 used in this work, as well as the area where the thin section was taken, are shown in the figure. The area circled with red is where the Lake Ronel Oil took one of their 21 core plugs. Lake Ronel's permeability and porosity measurements are available, but the plugs were lost and could not be CT-scanned

The thin section and two plugs are taken from about 4763.5 ft depth in the Wyoming core from Well #36-10. The core at the depth where the samples were taken is shown in Figure 3. Detailed thin-section analysis is discussed in Chapter 6. The cores are scanned and also taken to the laboratory to measure porosity and permeability. The Lake Ronel Oil Company made measurements available to us from 21 core plugs, but the actual plugs

are lost. Therefore, these 20 plugs could not be used for CT scanning. One such lost plug was located between plug #1 and #2, as indicated in Figure 3. Porosity variation among the three very closely located core plugs is probably controlled mostly by heterogeneities due to varying degrees of patchy anhydrite cementation. Plug #2 has 16.2% porosity, Lake Ronel's lost plug has 14.2 %, and plug #1 has 13.6 % porosity. Patchy anhydrite cementation can be seen as about two- to four-grain clusters in the thin section and also as white or gray spots in the core, as seen in the photo (Figure 3).

7.3.2 Prototype of Eolian Sand

The unconsolidated coastal dune sand sample was taken from the Año Nuevo coastal dune in northern California. Sieve and laser particle size analysis show the average grain size is 0.391 mm. A detailed description of this sand is given in Chapter 2. To produce a prototype, I pack loose sand grains in the laboratory and cement the pack with epoxy. Then, the prototype is scanned via X-ray tomography (CT-scan), which allows the three-dimensional pore geometry to be digitized. Because of the high density contrast between sand grains and the epoxy, the pore space is easy to visualize in the CT-scan.

However, packing the grains in different ways can cause some variation in porosity and fluid flow properties among the prototypes (Vega, 2003). Therefore, a prototype should be formed in a way similar to that used by nature. In the case of Año Nuevo, my goal is to produce a pack that represents a pre-diagenesis sand-pack. Therefore, I use a funnel and allow the sand grains to deposit and readjust on their own, without any additional force applied to pack the material (Figure 4). However, note that depositing with a funnel in the laboratory cannot duplicate the natural grain distribution of the wind-blown sand grains. The funnel-deposit method is chosen because it can be repeated easily in the laboratory. I do not tap or pack the grains manually, but simply allow the grains to fall and deposit, as to avoid further alteration of grain packing. I pour several portions of equal-weight Año Nuevo sand, thus the laminations are naturally created. Lastly, I pour a low-viscosity epoxy used in the boat industry and allow the epoxy to naturally penetrate into the pore space.

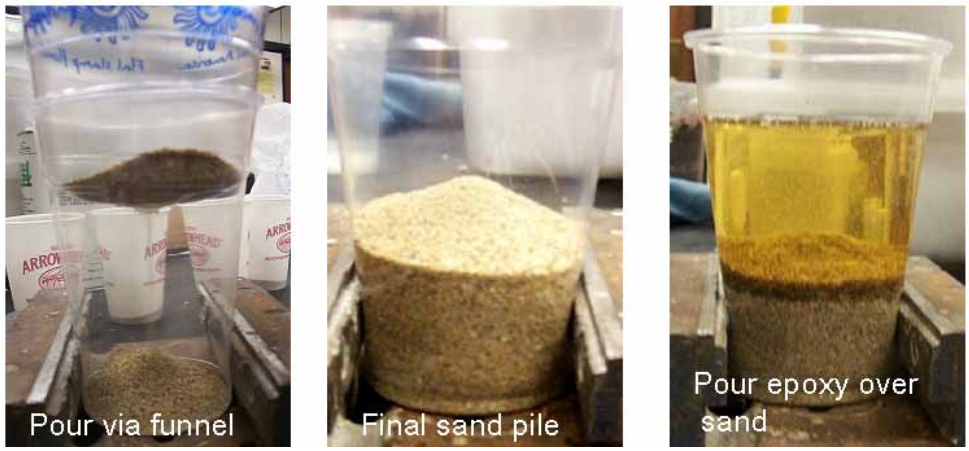

Figure 4. Making of eolian prototype Año Nuevo. Left: Pouring eolian sand grains using a funnel. Center: Final sand pile. Note the laminations. Right: Pouring low viscosity epoxy over the sand pile, allowing the pores to be filled by epoxy.

Figure 5. Eolian prototype Año Nuevo after epoxy hardens. The prototype is cut in half, and then into quarters. A quarter segment is sent for CT-scanning. Note the laminations preserved in the prototype.

After the epoxy is hardened, I cut the pack in half, and then into quarters (Figure 5). One of the quarter segments is CT-scanned to produce a prototype digital image. The CT-scan represents the Año Nuevo prototype in gray-scale; thus an appropriate threshold must be selected to convert the gray-scale into a binary image. In this case, I want a pre-diagenesis 3D digital image of an eolian sand-pack. Therefore, I select the threshold so that the porosity becomes 36%, which is about the critical porosity (36-40%) that separates suspended sand from load-bearing sandstone. After this process, I obtain a 3D digital image of 36% porosity eolian sand-pack that represents pore space as zeros, and solid grains as ones.

7.3.3 Thin Section Images of Wyoming Sandstone

A thin section was made from a segment of sand B in the Wyoming core. The thin section reveals predominantly quartz sand with a few dolomite grains. The image contains heterogeneity, which shows as medium-sized grains with bands of fine-grained laminations (Chapter 6, Figure 20). The texture of the sample also seems to include anhydrite cementation. As discussed in Chapter 6, a detailed analysis and literature search suggest that sand B gained secondary porosity when anhydrite cements dissolved preferentially in the well–sorted zone. The result is a texture-controlled patchy anhydrite cementation.

The thin section made from the sand B Wyoming core contains various micro-scale heterogeneities. Within a single thin-section image, one can identify three different sets of zones with distinct porosity and diagenesis characteristics (Figure 6). The first zone, which I refer to as "Porous," is a very lightly cemented (almost cement-free) and porous section with well-sorted medium quartz grains. I could not identify whether the porosity in this zone is primary or secondary. The next zone is the "Patchy" zone, which has patchy anhydrite cementation in clusters a few grains across. In spite of this patchy cementation, this zone remains porous. The third zone is "Tight," with extensive anhydrite cementation and very low porosity. The "Tight" zone is visible to the naked eye as gray or white spots in the physical samples, as seen in Figure 3.

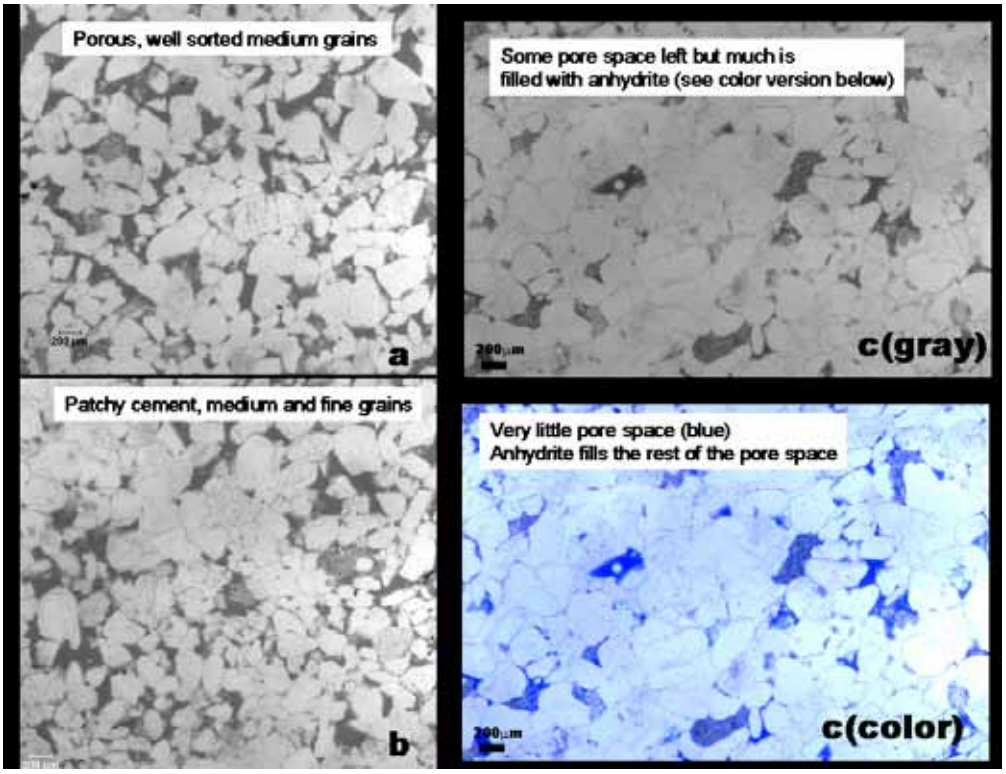

Figure 6. Thin section from the sand B Wyoming core. The thin section contained various micro-scale variations in porosity and degree of diagenesis. Within a single thin section, there are three sets of variations: a, b, and c. (a) A very lightly cemented (or uncemented) porous section with well-sorted medium grains ("Porous"). (b) A patchy-cemented area with medium and fine grains ("Patchy"). (c) A very tight pore space due to high degree of anhydrite cementation ("Tight") shown in gray-scale and in color (blue is pore space).

7.3.4 CT Scan of Plugs

Two plugs cored from the sand B section are #2 (16.2 % porosity, 172 mD) and #1 (13.6 % porosity, 128 mD). Both plugs are CT-scanned, and the plugs are imaged in gray-scale. However, unlike the case of the eolian prototype, where 36% (critical porosity) is chosen, I use the laboratory-measured porosity value (16.2 and 13.6% porosity, respectively) for threshold values. After thresholding, the 3D digital images of plugs #1 and #2 are converted to binary mode (1's and 0's), and are ready for further numerical experimentation.

7.4. Step 1A: Transformation in Space--Thin Section

The grain-scale heterogeneity observed within the sand B thin section can be separated into three groups, "Porous," "Patchy," and "Tight," in the order of decreasing porosity and increasing anhydrite cementation. My goal in this section is to convert "Porous" via numerical diagenesis to images with porosity and permeability of the "Patchy" and "Tight" types, as shown in Figure 2, Step 1A.

First, I take the 2D image of "Porous," and apply 2D numerical codes for compaction, grain expansion and patchy cementation. After numerical compaction, I randomly insert seven 0.4 mm patches into "Porous" and arrive at the "Simulated Patchy" image (Figure 7d). Then, I insert seven more patches to arrive at the "Simulated Tight" image (Figure 7e). The patch size was chosen to be a few grains across, in accordance with my visual inspection of the samples. The patch size and number of the patches are the input parameters in the numerical patchy cement code, and can be altered. By simple trial and error I arrive at the measured porosity value by simulating patchy anhydrite cementation on a 2D image.

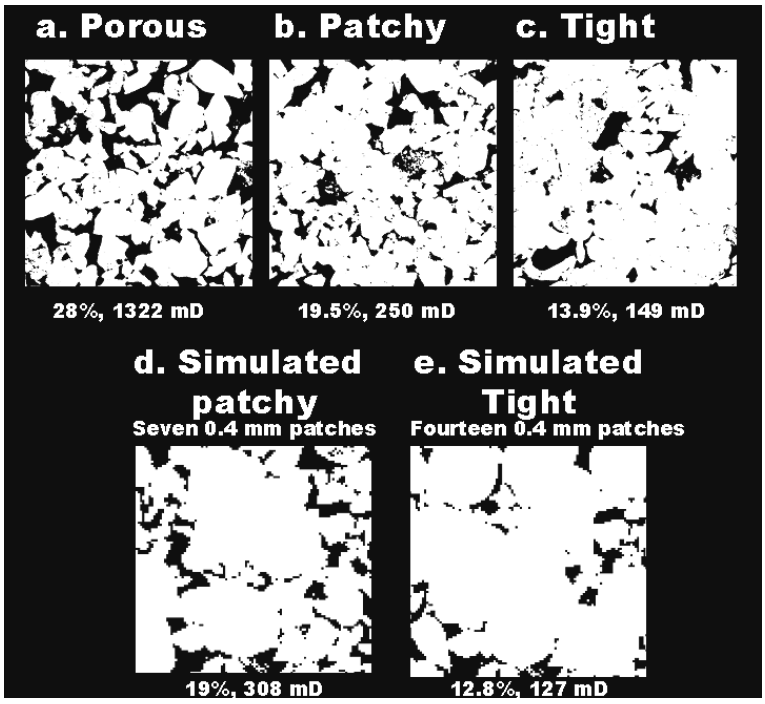

Figure 7. 2D images (a, b, and c) taken from a single thin section from Sand B as well as "Simulated Patchy" and "Tight" 2D images (d and e) that are actually altered images of the "Porous" image.

To compute permeability on the 2D images, I use the method introduced in Chapter 3. Specifically, I employ indicator geostatistics to simulate the third dimension of the rock using 2D thin-section images (Keehm et al., 2001). I have divided the highly heterogeneous thin section image into three zones, and assumed isotropy within each zone. The permeability values computed using geostatistics and the lattice-Boltzmann method are listed in Figure 7, together with the images, and are cross-plotted in Figure 8.

The actual diagenetic evolution path ("Porous" → "Patchy" → "Tight") and the simulated path ("Porous" → "Simulated Patchy" → "Simulated Tight") produce essentially the same 2D images (Figure 7) and result in essentially the same permeability evolution (Figure 8).

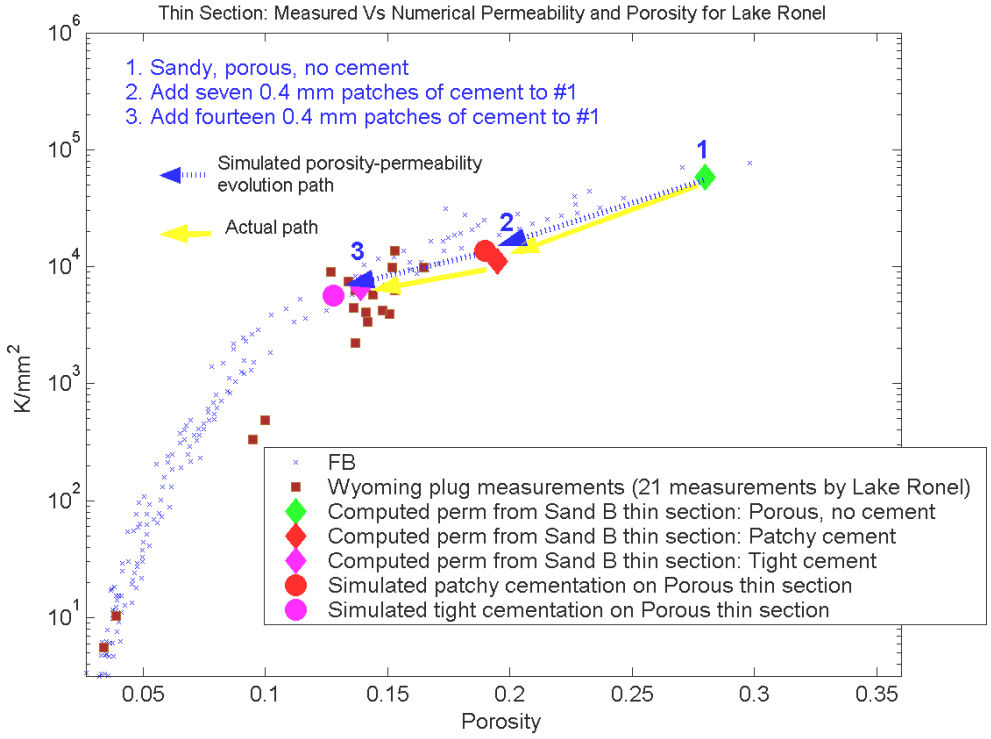

Figure 8. Summary of 2D diagenesis evolution of porosity and permeability of 2D images extracted from a single thin section. Porosity and permeability (1) computed on the porous, sandy section (green diamond), (2) computed on the patchy section (red diamond) and simulated patchy section (red circle), and (3) computed on the tight section (pink diamond) and simulated tight section (pink circle). Note that the porosity-permeability evolution of the simulated 2D images is the same as the computed porosity-permeability of the actual 2D images.

7.5. Step 1B and 2: Transformation in Time and Space--Core Plugs

7.5.1 Workflow

In this section, I explore diagenesis evolution in time by altering the Año Nuevo eolian prototype (pre-diagenesis) to match the Wyoming core plugs #1 and #2 (post-diagenesis), as shown in Figure 2, Step 1B and Step 2.

In the 2D method, an image slice of the prototype is altered via 2D codes to arrive at an image with porosity matching that of core plugs #1 and #2. Then, geostatistics is used to generate a 3D realization, upon which a lattice-Boltzmann fluid-flow simulation is conducted to compute permeability.

In the 3D method, a 3D digital volume of the Año Nuevo eolian prototype is altered via 3D numerical compaction and patchy cementation codes to arrive at a 3D volume with the porosity of the Wyoming plugs #1 and #2.

Going from plug #2 (patchy anhydrite cement) to plug #1 (more anhydrite cement) is much like moving in space (Figure 2, Step 1B). In the previous section, diagenetic evolution within a thin section (on mm to cm scale) was explored. However, in this section, a diagenetic evolution in the space between two plugs is explored. In contrast, going from a prototype to a core plug, as shown in Figure 2, Step 2, is much like transformation in time.

7.5.2 Transformation in 2D: Alteration of Prototype Image Slice

In the 2D method described in Figure 2, Step 2, a 2D image slice of the Año Nuevo prototype is used to explore whether it is possible to realistically model a diagenesis path using only 2D images. Numerically, altering 2D images is much simpler than altering 3D counterparts, as discussed in Chapter 5.

Image #28 of the Año Nuevo prototype CT-scan is chosen for this experiment, since its porosity is at the ideal critical porosity value of 36 %. Then, the image undergoes 2D compaction and expansion (Figure 9-2) and patchy cementation (Figure 9-3 and 9-4).

The altered images are then converted to geostatistical realizations (3D digital rocks) and permeability is computed via fluid-flow simulation.

7.5.3 Transformation in 3D: Alteration of Prototype Volume

A 3D digital image of the Año Nuevo prototype is altered via 3D numerical codes that simulate compaction and expansion, as well as patchy cementation, as described in Figure 2, Step 2. After the alteration, the samples have 16.4% and 13.8% porosity, mimicking Wyoming plugs #2 and #1 respectively (Figure 9). Fluid flow simulation through the altered prototypes gives the computed permeability values listed under the images in Figure9.

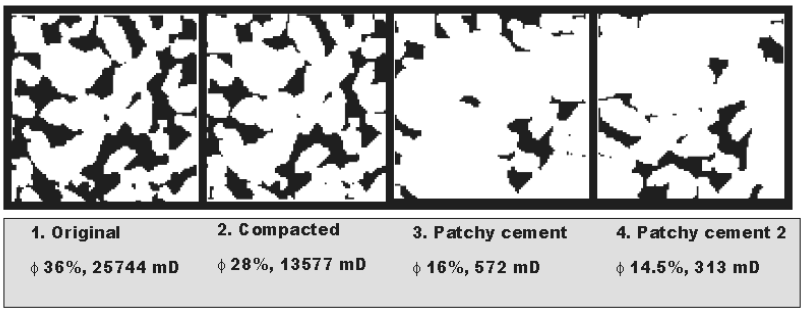

Figure 9. Sequence of 2D alterations of a prototype image. Shown in the figure are 2D images and computed porosity and permeability of (1) a prototype image, (2) after compaction, (3) after patchy cementation down to 16% porosity (matching core plug #2), and (4) after further patchy cementation simulation, reducing the porosity down to 14.5% (like the core plug #1).

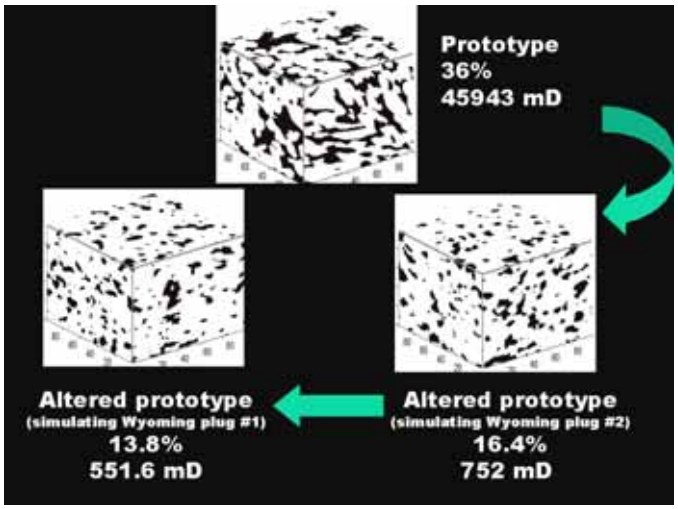

Figure 10. Sequence of 3D alterations of the prototype volume. Shown in the figure are the original Año Nuevo prototype volume, the altered volume after compaction and patchy cementation (simulating plug #2), and an even more altered volume after further cementation (simulating plug #1). The diagenetic evolution between prototype (pre-diagenesis) and core plugs (post-diagenesis) is much like mapping diagenesis in time. The diagenetic evolution between plugs #1 and #2 is analogous to mapping diagenesis in space.

7.5.4 Step 1B and Step 2: Results Summary

The assumption of a circular patch (for 2D) and a spherical patch (for 3D) is a simplification of the actual anhydrite cementation, and may not result in a perfect match between the simulated porosity and permeability and the target values. Also, massive generation of simulated patchy cementation to match a single target can be time-consuming, especially if the starting radius and patch number are wrong. An automation of such adjustment can be done in principle. However, at this stage, the code is manually operated, i.e., the user has to decide the input parameters and adjust accordingly.

Even with such a basic code, the results are remarkable (Figure 11). Both the 2D and 3D diagenesis paths seem to follow the measured path as well as that of the Fontainebleau trends. They also overlap the 21 plug measurements made by the Lake Ronel Oil Company.

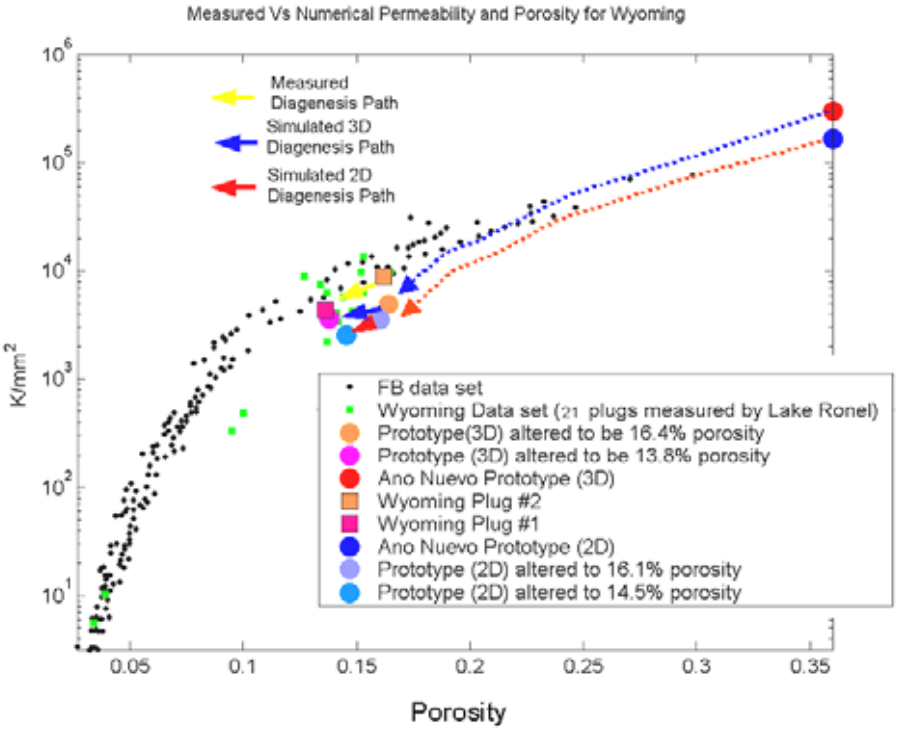

Figure 11. Permeability-porosity cross-plot summarizing 2D and 3D prototype alteration results. The yellow arrow indicates the computed porosity and permeability path between Wyoming plug #1 and #2. The blue arrow indicates the 3D computed porosity and permeability path between the original 3D prototype and the altered volumes via compaction and patchy cementation. The red arrow indicates the 2D computed porosity and permeability path between the original 2D prototype and the altered images via 2D compaction and patchy cementation schemes.

7.6 Chapter Summary

Chapter 7 focuses on the application of diagenesis tools to several digital images in an eolian core in Wyoming. In this chapter, digital images from sand B in the Minnelusa section are used to conduct quartz-overgrowth and patchy-cementation numerical experiments. The results show that by using a 2D or 3D prototype, one can numerically map digital rock evolution in time and obtain a reasonable porosity-permeability path.

There are 15 feet of dolomite B section in the core from Wyoming. The dolomite B is mostly altered dolomite or has massive anhydrite cementation with very little porosity. The dolomite B section acts as a barrier in the reservoirs because of its very low permeability. The depositional environment of this section is possibly an evaporitic and marine environment near the coastal dune field where sand B originates. Dolomite and evaporite occlude essentially the entire pore space through either deposition or diagenesis, or both. Such rock is nearly impermeable and is beyond the applications examined in this work.

Furthermore, applying a geostatistical algorithm in the low porosity range may produce inaccurate permeability values, as discussed in Chapter 3. In higher-porosity rocks, permeability can be reasonably reproduced if porosity is honored. However, at lower porosity ranges, the specific shapes of the pores are more critical in modeling permeability. For the 2D to 3D geostatistical simulation to be more applicable in such "tight" rocks, it is necessary to move beyond two-point statistics into multi-point statistics where pore throat shapes and connectivity will be more honored.

7.7 Conclusion

This chapter shows a few examples of how prototype technology, combined with numerical tools, can be used to model rock through geological space and time. Imposing numerical compaction, quartz overgrowth, and patchy cementation on a prototype helps to arrive at digital images of post-diagenetic rocks (plugs #1 and #2). The porosity and permeability computed on the altered prototypes matched the target porosity and permeability. Also, the alteration of the prototype reproduced a diagenetic porosity-permeability evolution trend similar to that of the Fontainebleau data as well as the 21 core plug measurements made by the Lake Ronel Oil.

The prototype technology and numerical diagenetic tools, therefore, can help open a new way of studying how well-log properties relate to geological input, as well as how well-log properties relate to one another. However, for further applications to become possible, it is necessary to update the geostatistical tools to make them more applicable for other rock types (tight gas sandstone and carbonates, for example), to expand prototype library, and to include more diverse diagenetic tools. Future development of such tools, currently being addressed by many researchers, will provide more flexibility and insight into the studies of rock properties that are related to intricate small-scale topology of the rocks.

7.8 Need for Upscaling

The lab-measured permeability values of the Wyoming plugs used in this chapter are 128 and 172 mD. These values are smaller than the values computed on smaller sub-volumes of these plugs, which are 666 and 1348 mD, respectively. Notice, however, that the physically measured permeability is very close to the 250 and 149 mD calculated for the patchy and tight parts of the thin section, as shown in Figure 7b and c. We speculate that these low-permeability parts of the rock block the flow and thus determine the effective permeability at a larger scale.

The digital-rock approach provides the building blocks, which then can be used in upscaling. The next chapter discusses the effects of upscaling on the permeability of larger volumes of rock.

7.9 References

Boronowski, J., *The ascent of man*, Little, Brown, Boston, Massachusetts, 1974.

Keehm, Y., T. Mukerji, and A. Nur, Computational rock physics at the pore scale: Transport properties and diagenesis in realistic pore geometries, *The Leading Edge*, **20**, 2, 180, 2001.

Vega, S., *Intrinsic and strength-induced velocity and anisotropy in unconsolidated sands*, Ph.D. Dissertation, Stanford University, 2003.

Chapter 8
The Road Ahead:
Upscaling Permeability

8.1 Abstract

In the previous chapter, the computed permeability values of small sub-volumes of Wyoming core plugs overestimated lab-measured permeability values. These sub-volumes are on the order of 1.3 mm by 1.3 mm by 1.3 mm, which is an order of magnitude smaller than the physical plug. I speculate that a possible reason for this overestimation is permeability heterogeneity in the relatively large physical sample. A single extensive, yet small-volume inclusion (or membrane) of small permeability may block the flow, even if other parts of the rock have large permeability. Digital sampling may miss these low-permeability blocks and thus overestimate the macroscopic permeability.

To address this issue, I suggest that upscaling has to be done on the basis of small building blocks, which are provided by the digital rock approach. In the specific example of the Wyoming sandstone, I find a portion of a thin section that has patchy anhydrite cement and small permeability. If macroscopic permeability is found as the harmonic average of this small permeability and larger permeability, the small permeability dominates and the macroscopic value appears to be close to the physically measured permeability value.

The whole issue of estimating macroscopic permeability from the permeability of smaller parts of the rock is often called upscaling. This upscaling issue is not unique for the digital rock application. It has to be addressed at all scales, even if permeability is traditionally measured on physical plugs with the purpose of estimating larger-scale reservoir permeability.

The question that I address here is how to upscale small-scale digital permeability to a core-plug scale. I speculate that lower permeability parts of the rock determine the effective permeability. To test this hypothesis, I use harmonic, arithmetic, and geometric mean upscaling with both the Minnelusa data and Berea sandstone data.

8.2 Computed vs. Measured Permeability of Minnelusa Core Plugs

The lab-measured permeability values of the two Wyoming core plugs are 128 and 172 mD, whereas the computed permeability values on the CT-scanned sub-volumes of these plugs are 666 and 1348 mD, respectively. The measured permeability is much lower than the computed permeability (Figure 1).

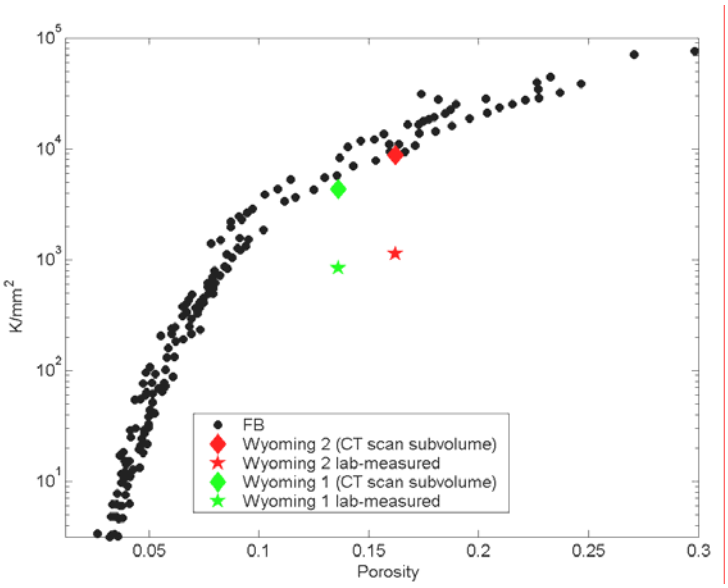

Figure 1. Permeability-porosity cross-plots of Wyoming plug #1 and #2 results, comparing lab-measured (stars) and computed (diamonds) permeability values. The computed permeability values are computed on sub-volumes of the CT-scan images of plug #1 and #2. The sub-volumes are in the order of 1.3 X 1.3 X 1.3 mm^3. The core plugs are one inch in diameter and 2 inches tall. The difference between the lab-measured and computed permeability values might be the effect of upscaling.

I speculate that the main reason for this disparity is permeability heterogeneity in the samples. Small areas with low permeability, not necessarily represented in the scans, can influence the effective permeability of a larger sample. In the previous chapter, the lab-measured permeability of the core plugs (128 and 172 mD) is very close to the permeability values calculated on small thin-section images with anhydrite cementation (250 and 149 mD) (Figure 2). I speculate that the patchy cementation within the core plug lowers the effective permeability values. In reality, fine-scale sedimentary structure such as lamination rich in heavy minerals may be playing a role. In this chapter, however, I will focus on the patchy cementation.

However, The question is, then, how to combine permeability building blocks to arrive at the effective permeability on the core-plug scale. Figure 2 shows the input building blocks to be used in the following calculations.

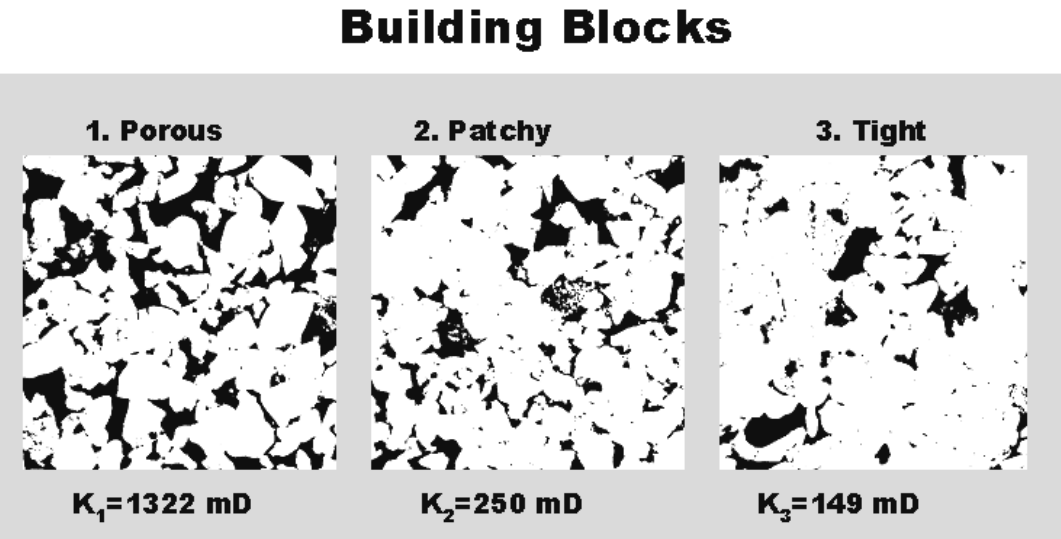

Figure 2. Computed permeability on small portions of a thin section taken from sand B of the Minnelusa core. 2D images are converted to 3D blocks using geostatistics discussed in previous chapters. The permeability values computed on the patchy and tight parts of the thin section are close to the lab-measured permeability of the core-plugs.

8.3. Upscaling Methods Overview

The effective permeability of a 3D network of building blocks (each with a known permeability) may take values between the harmonic and arithmetic average of the block permeability values, depending on their spatial arrangement (Figure 3). Conventionally,

the arithmetic mean is used to average permeability values parallel to the bedding (horizontal) direction, while the geometric or harmonic mean is used to average permeability values perpendicular to the bedding (vertical) (e.g., Deutsch, 1989, Weber and van Geuns, 1990). The geometric mean produces effective permeability larger than the harmonic mean but smaller than the arithmetic mean. Whereas the harmonic and arithmetic mean are used for averaging simple, correlated, uniformly stratified permeability distributions, the geometric mean is used to yield the effective permeability of a random, uncorrelated, isotropic permeability distribution (Warren and Price, 1961). In this chapter, I will apply the arithmetic, harmonic and geometric means to compute the effective permeability, where the arithmetic mean (or K_h) is expressed as follows:

$$K_h = \frac{1}{N}(K_1 + K_{N+1}.....+ K_N), \tag{1}$$

the harmonic mean (or $K_{v\_harmonic}$) is expressed as follows:

$$K_{v\_harmonic} = \frac{N}{\frac{1}{K_1} + \frac{1}{K_{N+1}}..... + \frac{1}{K_N}}, \tag{2}$$

and the geometric mean (or $K_{v\_geometric}$) is expressed as follows:

$$K_{v\_geometric} = \sqrt[N]{K_1 K_{N+1}....K_N}\ . \tag{3}$$

To simplify the computation of the effective permeability, I assume that the volume fractions of each building block are the same.

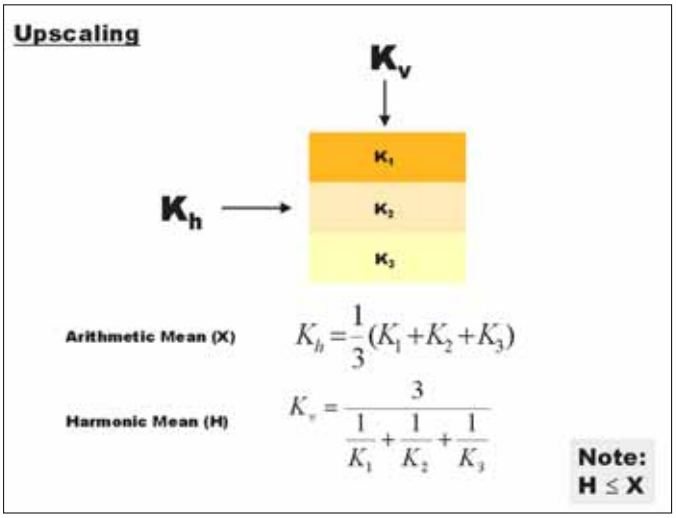

Figure 3. Schematic figure showing the difference between arithmetic (X) and harmonic (H) mean, which are used to average permeability measurements in the horizontal (parallel to bedding) and vertical (perpendicular to bedding) directions, respectively.

8.4. Application of Upscaling to Minnelusa Data

I use equations 1-3 to compute arithmetic, harmonic, and geometric averages of permeability values from porous, patchy, and tight building blocks. The results of the effective mean calculation shows that the harmonic mean, with 261 mD, is the best match to the core-plug permeability measurements (Table 1). As the harmonic mean is conventionally used to compute the vertical (or layer-perpendicular) permeability, and the permeability measured on the core plugs is the vertical permeability (perpendicular to the bedding), this type of upscaling appears to be relevant to the data under examination. The harmonic mean emphasizes the effect of the lower permeability zones on the overall effective permeability.

Minnelusa Results

Building block	1. Porous	2. Patchy	3. Tight
Permeability (mD)	1322	250	149
arithmetic mean	573.67	mD	
harmonic mean	261.60	mD	
geometric mean	366.54	mD	

Building block	1. Porous	2. Patchy	3. Tight
Porosity	0.28	0.195	0.139
arithmetic mean	0.20		

Core plugs 13.6% 128 mD (plug #1) and 16.2% 178 mD (plug #2)

Table 1. Results of effective porosity and permeability calculation using three of the Minnelusa permeability data: porous, patchy, and tight. The harmonic mean yields the best match for the effective permeability. Porosity is calculated by arithmetic mean.

The effective permeability calculation also depends on the volume fraction of the building blocks. In Table 1, I assumed that each block, porous, patchy, and tight, has equal weight in calculation. However, if the sample contains mostly patchy and tight building blocks, and hardly any porous, it might be more accurate to use different building block proportions. For example, if I model the rock to be a composite of patchy and tight building blocks only, then the permeability is much lower (Table 2). Of course, such assumptions must be based on detailed observations of rock microstructure.

Minnelusa Results 2

Building block	2. Patchy	3. Tight
Permeability (mD)	250	149
arithmetic mean	199.50	mD
harmonic mean	186.72	mD
geometric mean	193.00	mD

Building block	2. Patchy	3. Tight
Porosity	0.195	0.139
arithmetic mean	0.17	

Core plugs 13.6% 128 mD (plug #1) and 16.2% 178 mD (plug #2)

Table 2. Results of the effective porosity and permeability calculation using two of the Minnelusa permeability data: patchy and tight. The harmonic mean yields the best match for the effective permeability. The effective porosity is calculated by arithmetic mean.

The effective permeability and porosity calculated in Tables 1 and 2 are summarized in Figure 4. The effective permeability values, which account for low-permeability zones, are a better match to the lab-measured permeability than the computed permeability on the sub-volumes of CT-scanned images. By employing the appropriate volume fraction of the building blocks, one can upscale the numerically computed permeability from a mm^3 volume to the permeability of a core-plug.

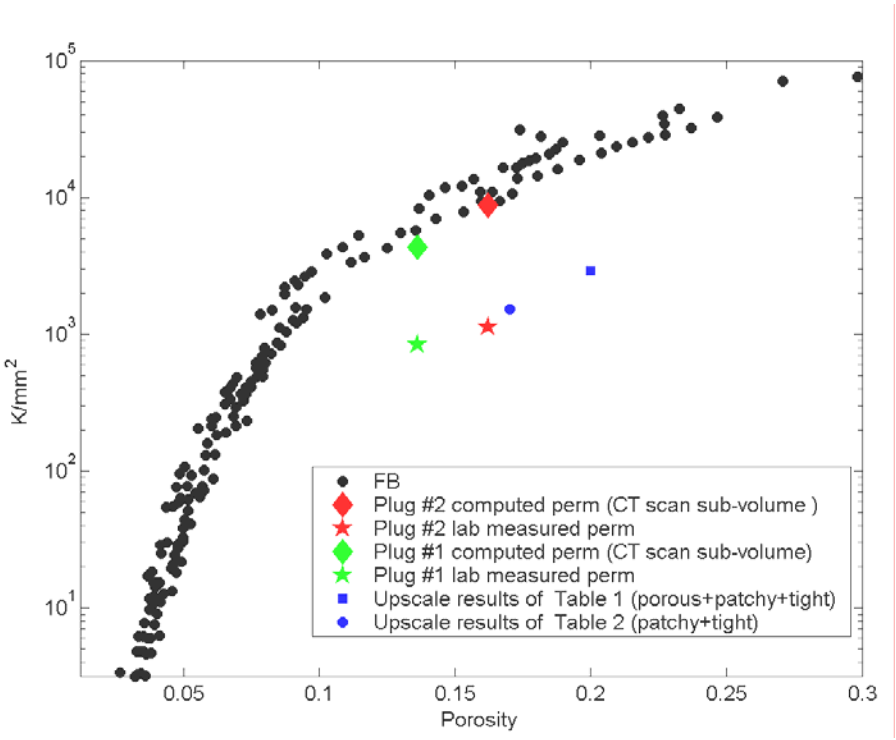

Figure 4. Summary of Minnelusa upscale results (shown in blue). The effective permeability (harmonic mean) and porosity (arithmetic mean) results from Table 2 (patchy and tight) are much closer to those of the lab measurement of plug #2, than the computed permeability of CT-scan sub-volumes.

8.5. Application of Upscaling to Berea Sandstone Data

8.5.1 Core Plug and Building Block Images

Next, I compute the effective permeability of the Berea sandstone core plug 92-96, which contains mostly porous sandstone with a few, thin, horizontal layers of shale (Figure 5), to demonstrate how such low-flow layers can lower the effective permeability. Four thin-section images are taken from the sandstone (Figure 6).

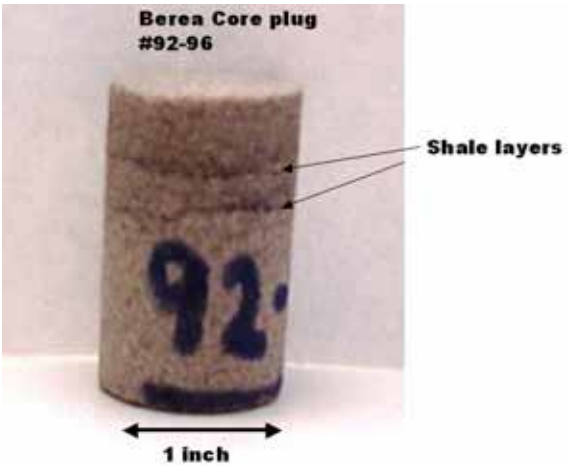

Figure 5. Photograph of Berea core plug #92-96, showing the shale layers as brown color. Black arrows indicate the two distinct layers of shale.

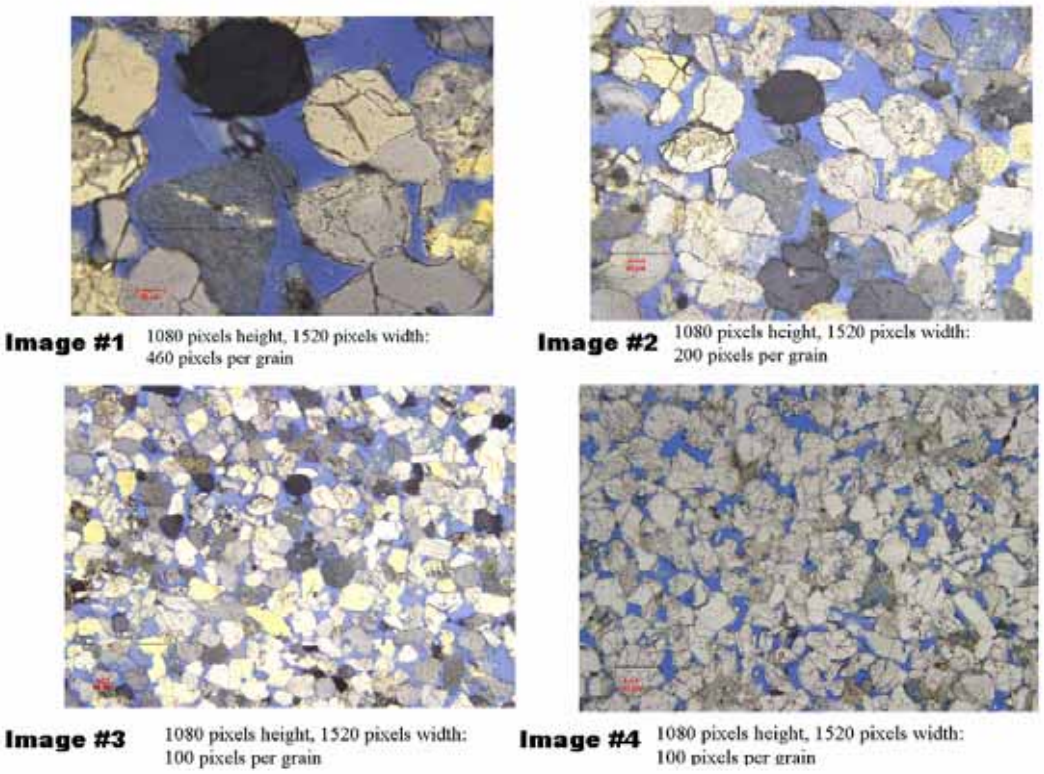

Figure 6. Images used as building blocks for the Berea sandstone upscaling experiment. The 2D images are converted to 3D digital realizations via the geostatistics method; a fluid flow simulation is conducted on the digital realization to obtain computed permeability. Note that the images have different resolution. The red markers are 50 microns for images #1-3, and 100 microns for image #4.

8.5.2 Individual Permeability Results

The clean sand images taken from the Berea sandstone (Figure 6) are used to produce 3D realizations via geostatistics, thus yielding multiple computed permeability values. Results are shown in Table 3. All of the computed permeability values are orders of magnitude higher than the lab-measured permeability value of the core plug, because of the thin shale layers. Since there is no thin section made of the shale layer, I arbitrarily assign a permeability value of 10 mD for the shale layer.

	Sample	Porosity	K_mD	
Plug	Berea plug 92-96	0.288	107.24	Lab-measured perm on the core plug
Image	1	0.288	581.21	Computed perm on the small images 1-4
Image	1	0.291	483.62	
Image	2	0.301	1302.1	
Image	2	0.291	867.56	
Image	2	0.298	1118.5	
Image	3	0.289	1606.8	
Image	3	0.278	1443.1	
Image	4	0.285	509	
Image	4	0.295	741	

Table 3. List of lab-measured and computed porosity and permeability for Berea plug # 92-96. Note the lab-measured core plug permeability is much smaller than the computed permeability. Images are shown in Figure 6. Each image produces multiple realizations of digital rocks, and thus multiple computed permeability values. Images are of sand only. Shale was not imaged.

8.5.3 Upscaling Results

To conduct effective permeability calculations, I must decide which computed permeability values to choose from Table 3. Furthermore, I must decide the volume fraction between sand and shale. I use all of the computed values listed in Table 3, and average them via arithmetic, harmonic, and geometric methods (Table 4).

Sand Fraction	K (mD)	
Arithmetic mean	961.422	K1
Harmonic mean	801.244	K2
Geometric mean	878.163	K3
Shale	K (mD)	
Assumption	10	
	Porosity	
Arithmetic mean	0.29067	

Table 4. Permeability values used in the final calculation shown in Figure 10. The sand fraction is the arithmetic, harmonic, and geometric mean of all 9 values shown in Table 3. The calculated effective permeabilities of the sand fraction are labeled K1, K2, and K3, respectively. The shale permeability is assumed to be 10 mD. Effective porosity is calculated as an arithmetic mean of the 9 values in Table 3.

As for the two thin layers of shale, I estimate that the combined thickness is about 3 mm, whereas the rest of the core plug is a porous sand, about 29 mm thick. Based on this information, I assign a shale to sand volume fraction of 1:9. Effective permeability values for three scenarios, using K1, K2, or K3 for the sand fraction, are shown in Table 5. The harmonic mean yields an effective permeability of about 90 mD, comparable to the core plug measurement of 107.24 mD. A very small amount of shale can greatly reduce the effective permeability if it is laterally continuous, as in the case of this particular sample.

	using K1	using K2	using K3
Arithmetic mean	866.28	722.12	791.347
Harmonic mean	91.4402	89.902	90.704
Geometric mean	609.007	516.88	561.329

Assume Sand 9: Shale 1

Table 5. Effective permeability of the Berea core plug assuming the sand volume fraction to be 90 % and shale to be 10 %. Sand permeabilities are K1, K2, and K3. Overall effective permeabilities including shale are shown in the table. Even though the shale is only 10 % of the volume, it greatly reduces the effective permeability in the vertical direction, especially if one assumes the harmonic mean. The measured core plug permeability is 107.24 mD, and is very close to the harmonic mean in this figure, about 90 mD.

8.6 Chapter Summary

2D images obtained from Minnelusa sandstone and Berea sandstone are used to compute permeability. However, these images are very small, and the permeability computed from these images needs to be upscaled to match the core plug measurements. In the Minnelusa sandstone, there are anhydrite cement patches that inhibit fluid flow, whereas in the Berea sandstone, thin shale layers inhibit vertical fluid flow. Various averaging schemes are tested to upscale the computed permeability values, but the harmonic mean, commonly used to upscale vertical (or bedding-perpendicular) flow, seemed to work the best. In both Minnelusa and Berea sandstone, low-flow zones greatly reduced the effective permeability.

8.7 The Road Ahead

Prototyping and digital rock technology allow researchers to compute various properties and conduct various numerical experiments. However, such results are done on small volumes in the order of 1 mm^3. The results, therefore, need to be upscaled for them to be compared to the physically measured data. The harmonic mean seems to work well when incorporating small, low-flow zones caused by heterogeneities in the rock.

In this chapter, I use anhydrite cementation and shale layers as examples of how these heterogeneities may greatly affect the overall permeability of rock. On the other hand, not discussed in this chapter are fractures, which will greatly increase the flow, unlike cements or shale layers. It is important to make reasonable assumptions about the flow conditions and the spatial composition of the building blocks.

Digital rock technology provides a tool to accurately describe such building blocks and accommodates experiments such as numerical diagenesis. It is then up to the researcher to choose appropriate methods for upscaling the results for use in different applications.

8.8 References

Deutsch, C., Calculating effective absolute permeability in sandstone/shale sequences, *SPE Formation Evaluation*, **9**, 1989.

Warren, J.E. and H.S. Price, Flow in heterogeneous porous media, *Soc. Petroleum Eng*., **1**, 152-169, 1961.

Weber, K.J. and L.C. van Geuns, Framework for constructing clastic reservoir simulation models, *J. Petroleum Technology*, **10**, 1248-1297, 1990.

Chapter 9
Conclusion

Making the simple complicated is commonplace; making the complicated simple, awesomely simple, that's creativity.
–Charles Mingus

9.1 General Statement

This dissertation is based on a very simple philosophy: less toil leaves more time and energy for creativity. Rather than finding a scientific solution to a problem by using bigger and more complicated technology, I wanted to use faster technology that can be made, in principle, available to many researchers. Specifically, I was interested in the question of sandstone permeability. Can I merge geological concepts and digital rock physics to tackle the question of predicting permeability? I believe that this dissertation not only paves a way to understanding permeability, but also creates new questions: Why is there a porosity-permeability trend at the micro-scale that matches the macro-scale trend? Why do some diagenetic alterations made on a thin section robustly translate,

via statistical reconstruction, into alterations on a true 3D image? What is the role of upscaling in the digital rock approach and, in general, in any approach that tackles permeability? I hope that future researchers can solve these problems and explain the phenomena that were observed when I applied the digital rock physics approach to sandstone data.

9.2 Significance of Contribution

The research from this dissertation led to two published papers, Mese et al. (2004) and Kameda and Dvorkin (2004). In summary, the dissertation introduces the following innovations:

- **Prototyping:** Introduces the concept of prototyping, to solve the problem of creating 3D digital pore-space images for permeability simulations. Instead of creating such images mathematically by numerically packing grains into 3D volumes (which is intractable, except for the simplest geometrical shapes), I create physical prototypes in the lab (e.g., sand grain packs), CT-scan them, and then conduct diagenetic and textural alterations on these prototypes in the computer.
- **2D to 3D Permeability Calculation Workflow**: Establishes that small and statistically sub-representative 2D images of sandstone can still be used to generate a valid permeability-porosity trend after geostatistical reconstruction of the third dimension and subsequent numerical flow simulation.
- **Diagenesis Modeling in 3D:** Develops algorithms to simulate diagenesis, such as quartz overgrowth and patchy cementation, as well as textural variations due to deposition (insertion of clay particles) for 3D digital images.
- **Diagenesis Modeling in 2D:** Develops algorithms to simulate diagenesis on 2D digital images followed by geostatistical reconstruction of 3D digital rock from these 2D images. Shows that in some instances, such as with well-sorted sandstone, this approach to modeling diagenesis in 3D provides satisfactory permeability estimates.

- **Application of Prototype and Diagenesis Modeling:** Applies the new tools introduced in the dissertation to a Wyoming eolian core data set. Shows porosity-permeability evolution with diagenesis.
- **Upscaling:** Although far from solving the upscaling challenge, I show how simple upscaling schemes may be used to upscale micro-scale permeability to a core-plug scale permeability.

9.3. Velocity

In this dissertation, I investigate permeability. However, it will greatly improve our understanding if velocity can be linked to permeability, thus allowing remote sensing technologies to be fully utilized to predict permeability. Digital rock physics is a promising platform to conduct multiple experiments on the same digital rock structure, thus making it possible to link permeability and velocity. As a very preliminary experiment, I use a Finney (1970) pack to make small 2D image slices, use geostatistics to simulate corresponding 3D digital realizations of each of the images, then compute velocity from those 3D realizations. This is very similar to the workflow introduced in Chapter 3 with permeability in the thin sections. Rather than fluid flow, I now use *elas3d,* a Finite Element Modeling elastic simulation code. The code has been developed by the National Institute of Standards and Technology (2004), and modified by Youngseuk Keehm (not yet published).

The result (Figure 1) is a porosity-velocity trend, very distinctive and similar to Han's (1986) data set. The computed velocities over-predict both the primary and secondary measured velocity data set, due to the resolution at the grain contacts, but reproduce the observed velocity-porosity trend. Once the resolution is improved, which is possible with more computational power, the accuracy will improve as well.

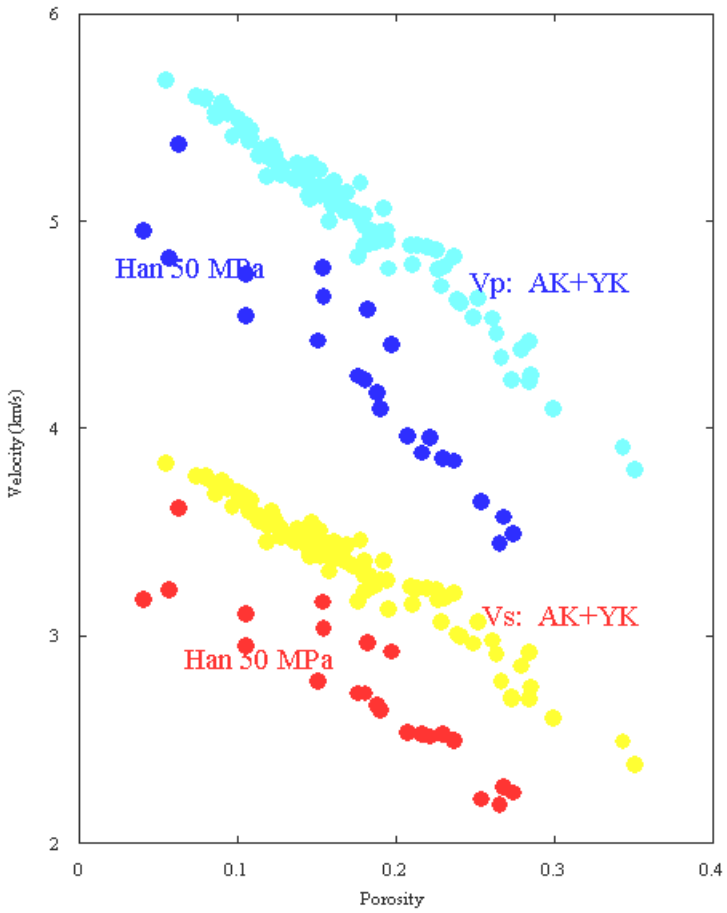

Figure 1. Velocity computed on small Finney-pack thin sections (yellow and light blue), compared to Han's (1986) data set (dark blue and red). AK+YK indicates small Finney-pack thin section simulation results by Ayako Kameda and Youngseuk Keehm.

9.4 Suggested Future Research and Potential Application

One future research direction is to compute relative permeability in addition to absolute permeability for the workflow introduced in Chapter 3 (permeability in the thin section) and Chapter 7 (porosity-permeability evolution with diagenesis). Relative permeability is difficult to measure in the laboratory and may be harder to corroborate with numerical results, but it nevertheless will be more applicable in the petroleum industry.

Some other aspects of the dissertation can be improved, such as expanding the prototype library, using more diverse rock types for CT-scanning, adopting multi-point geostatistics, expanding more diagenesis codes, and further numerical experiments with

velocity on the digital rock laboratory. The prototypes can be improved by expanding the library for various depositional environments, CT-scanning rocks that are not the mid- to high-porosity sandstone used in this dissertation, such as tight gas sands, shaly sands, and carbonates.

Also, the future direction should include adopting multi-point statistics in the geostatistics routine, which would allow accurate simulation of pore shapes in the 2D thin sections. This change in the geostatistics routine would allow 2D images of low-porosity sandstone to be used to compute porosity-permeability trends. To improve the applicability of this technology, any future research should include expanding the numerical diagenesis code. Finally, using the digital rock physics platform, elastic and fluid-flow properties should be compared to better understand the link between velocity and permeability.

Potential application of the results and technologies described in this dissertation are:

- Producing porosity-permeability trends from small cuttings or thin-section images
- Using 2D or 3D digital images of rocks to conduct diagenesis simulation and thus obtain porosity-permeability evolution trends. The diagenesis will be forward-modeled for basin-specific rock-alteration paths, using available geological data and "what-if" scenarios.
- If velocity can be calculated on the same digital rocks as the permeability, seismic surveys or well-logs can be used, in principle, to assess permeability.

9.5 References

Finney, J., Random packing and the structure of simple liquids I: the geometry of random close packing, *Proc. Roy. Soc.*, 319A, 479, 1970.

Han, D., *Effects of porosity and clay content on acoustic properties of sandstone and unconsolidated sediments*, Ph.D. thesis, Stanford University, 1986.

Kameda, A., and J. Dvorkin, To See a Rock in a Grain of Sand, *The Leading Edge*, August, 2004.

Mese, A., A. Tutuncu, A. Kameda, A. Nur, and J. Dvorkin, Digital rock physics for sands and shales, Oil & Gas Network, June, p. 68, 2004.